Quarterly Report for

Contract DE-FG36-08GO18192

Stanford Geothermal Program

January-March 2012

Table of Contents

1. FRACTURE CHARACTERIZATION USING PRODUCTION DATA

This research project is being conducted by Research Assistant Egill Juliusson, Senior Research Engineer Kewen Li and Professor Roland Horne. The objective of this project is to investigate ways to characterize fractured geothermal reservoirs using production data.

1.1 SUMMARY

This report describes the application of methods that have been developed for analyzing tracer and flow-rate signals to characterize fractured geothermal reservoirs, to data from a three-dimensional reservoir model with upscaled fractures.

The revised inversion method that was discussed in the quarterly report from Fall 2011 is used to find tracer kernels. The kernels are first estimated using a nonlinear parametric function which is somewhat restricted in shape. This constraint is subsequently relaxed by reverting to a nonparametric model that uses the parametric estimate as a prior.

The thermal transport properties of the three dimensional model were also investigated. It was shown that a commonly used thermal transport model (Lauwerier, 1955) does not capture the thermal decline very well. A simple streamline based model (Gringarten and Sauty, 1975; Barker, 2010) was also applied but that did not capture the thermal drawdown well either. The leading cause of this discrepancy has not been fully determined at this point.

1.2 INTRODUCTION

A multiwell tracer test will usually have different types of tracer going into each injection well, so as not to create any confusion about from where the tracer originates. However, there are situations where the same tracer, e.g. a natural recirculating chemical compound, could be going into all of the injection wells at once. An example of such data comes from the Palinpinon field in the Philippines, where the chloride concentration in the produced brine showed distinct variations over a 15 year production period. Figure 1.1 shows the chloride concentration in production well PN-29D, along with the variation in injection rates into each of the injection wells PN-1RD through PN-9RD. The chloride concentration of the reinjected brine had an increasing trend because part of the fluid produced from the reservoir was separated as steam going to the power plant.

Urbino and Horne (1991), Sullera and Horne (2001), Horne and Szucs (2007), and Basel et al. (2011) have worked on decoding this data set without conclusive results on how much information can be obtained. Working with the Palinpinon data was challenging because the data were sampled sparsely, a large number of predictors (nine injection wells) were influencing the response, the production rates were not available and two-phase flow in the reservoir may have been affecting the tracer flow paths in highly nonlinear ways.

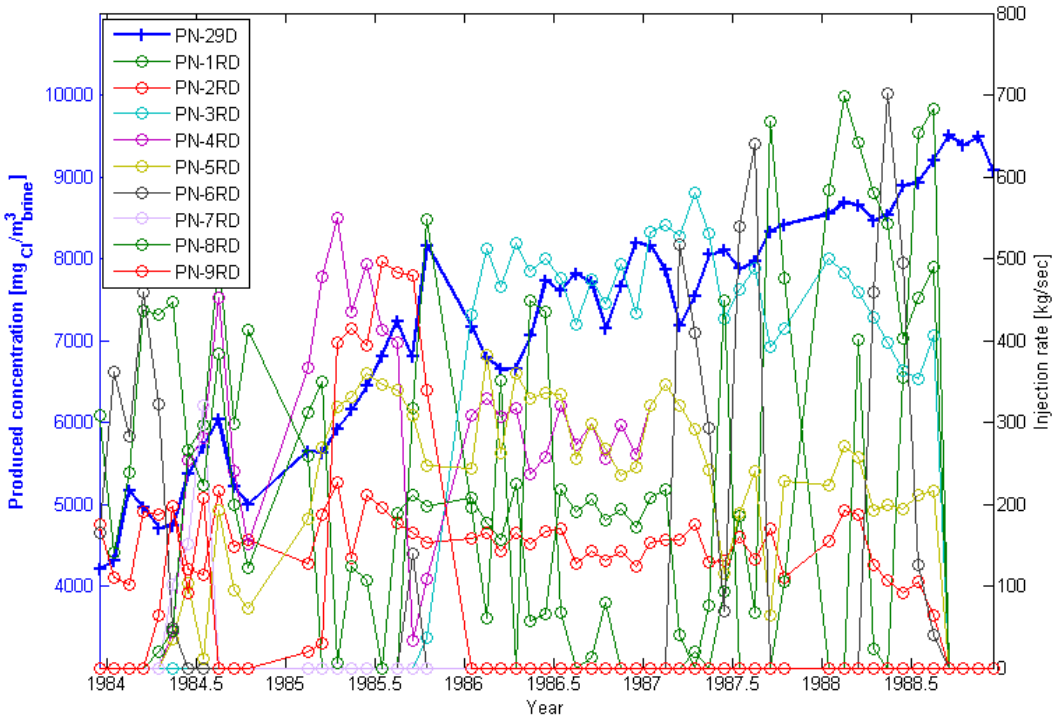

Figure 1.1: History of injection rates and produced chloride concentration in well PN-29D, in the Palinpinon field, Philippines.

In an effort to start answering questions about how much information could be obtained from this type of data it was deemed most practical to work on similar data sets that were created using numerical flow simulation models. The quarterly report from Fall 2011 outlines a methodology for solving the tracer transport problem where the same tracer is being injected into more than one well. The examples in that report were focused on how to estimate the tracer kernel for data coming from two-dimensional discrete fracture reservoir models. In this report we will investigate similar scenarios for data from a three-dimensional upscaled reservoir model.

1.3 KERNEL ESTIMATION WITH A THREE-DIMENSIONAL RESERVOIR MODEL

The results of tracer kernel estimation with data generated from a three-dimensional upscaled reservoir model are illustrated in this chapter. This numerical reservoir model will be referred to as Model III (to be distinguished from Models I and II from the quarterly report from Fall 2011). Model III did not contain discrete fracture elements but instead a distribution of discrete fractures was upscaled to a relatively coarse computational grid. The underlying fracture network was built using the fracture generation software FRACMAN. The fracture network, shown in Figure 1.2, had 200 fractures which were drawn from two sets of fractal (power-law) size distributions, with 100 fractures in each. One of the fracture sets had a N-S trend and the other had a NE-SW trend. The fracture aperture and hydraulic conductivity were correlated to the fracture size, and the NE-SW

fractures were given two times higher conductivity values on average. The fracture conductivity ranged from about 10^{-3}-10^{-1} m/s. The hydraulic conductivity of the matrix was set to 10^{-7} m/s. The aperture distribution covered about 1-10 mm. The porosity of the fractures in FRACMAN was assumed to be one, and the matrix porosity was zero. The connection between wells I1 and P2 was considerably better than that between I2 and P1 as a result of the NE-SW trend in the second set of fractures.

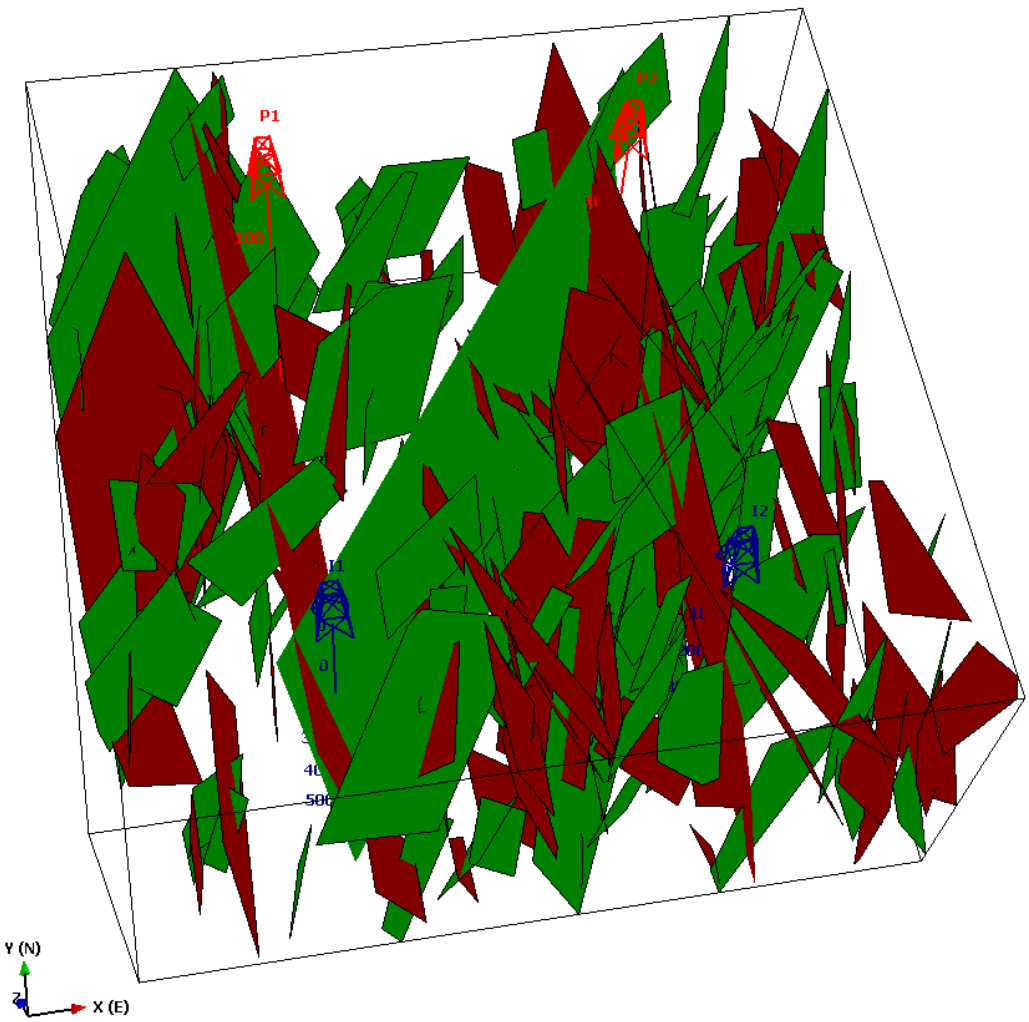

Figure 1.2: The three-dimensional fracture network underlying Reservoir Model III.

The fracture network was upscaled to a grid of 50x50x25 blocks, making each block 20x20x20 m^3 in size. The hydraulic conductivity of the blocks ranged from 0.001 to 433 m/s after the upscaling had been performed. Similarly the porosity ranged from 0 to 0.006. The upscaled data were imported into FEFLOW for flow simulation. The log of hydraulic conductivity in the y-direction (N-S) in the upscaled model is shown in Figure 1.3.

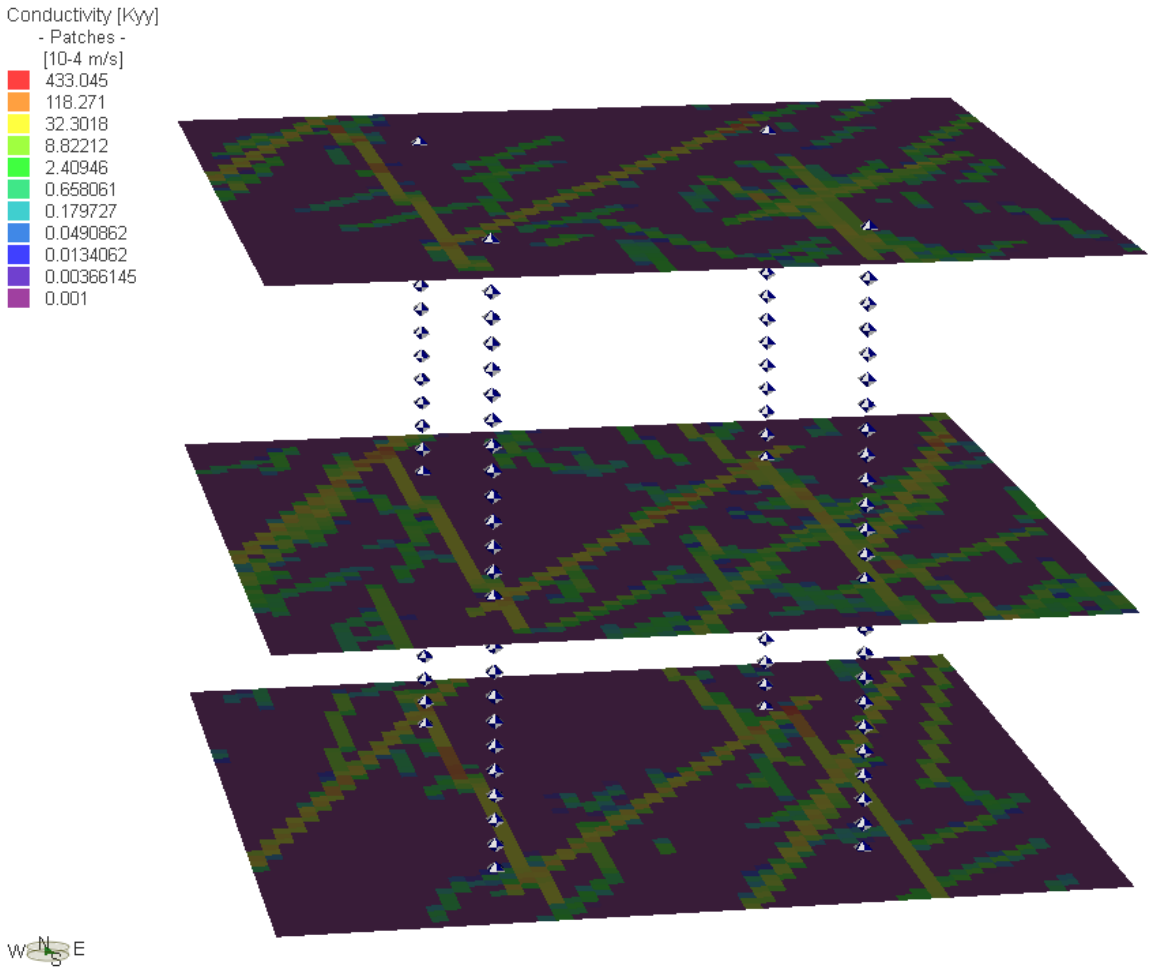

Figure 1.3: The log of hydraulic conductivity in the y-direction (N-S) in the computational grid for Model III.

Figure 1.4 gives a snapshot of tracer distribution in the reservoir model after 100 days of tracer injection into injector I1, with concentration 1 mg/L and water injection rate 2500 m^3/day. Table 1.1 summarizes the main properties of Model III.

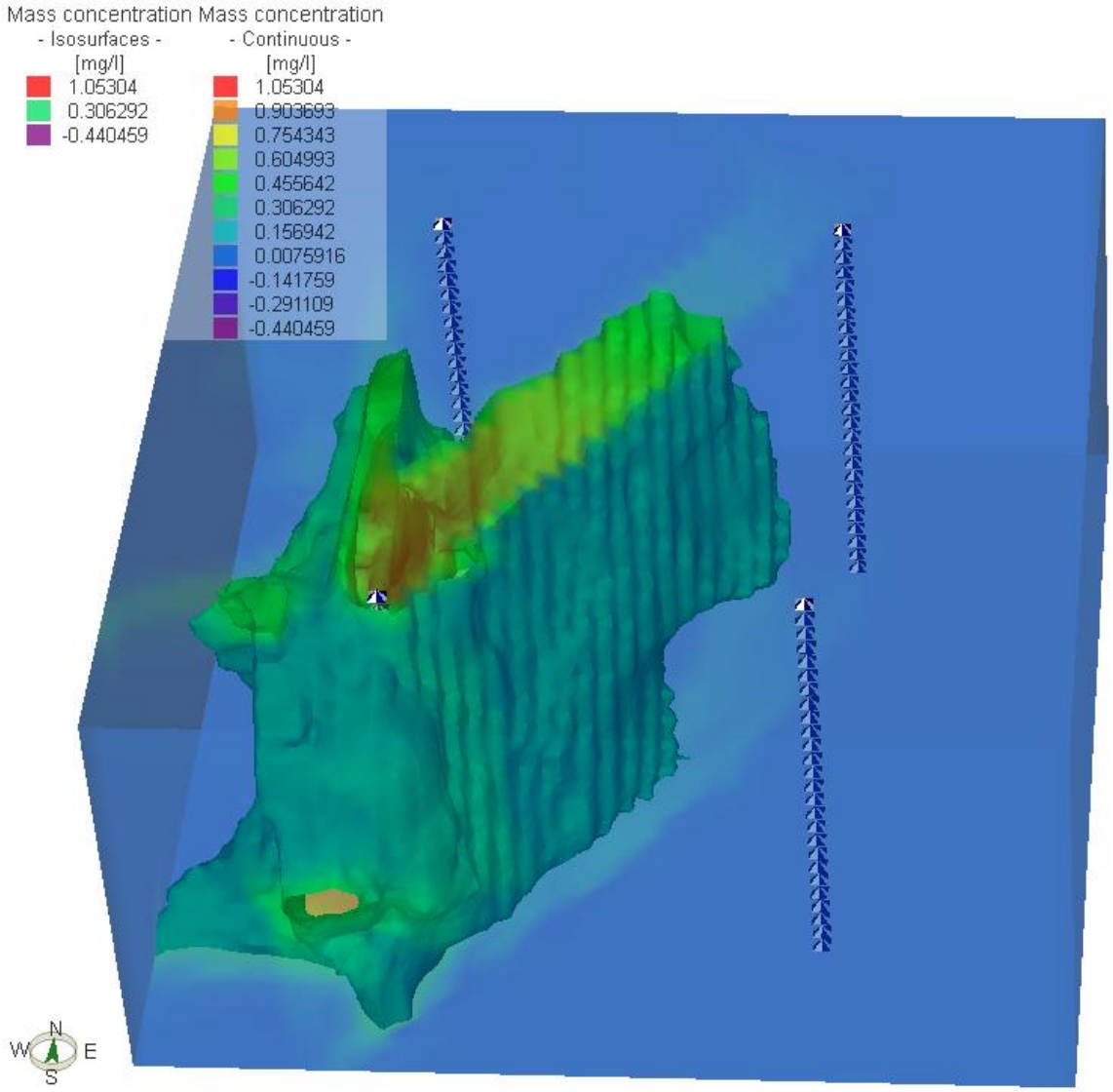

Figure 1.4: A snapshot of tracer distribution in Model III after 100 days of tracer injection into injector I1, with concentration 1 mg/L and water injection rate 2500 m^3/day.

Table 1.1: Summary of properties for Reservoir Model III.

General		
	Dimensions	1000 x 1000 x 500 m^3
	Initial temperature	150 C
	Rock heat capacity	2520 kJ/m3/C
	Rock heat conductivity	3 J/m/s/C
	Longitudinal dispersivity	1 m
	Transverse dispersivity	0.1 m
Fractures		
	Number of fractures	200
	Discrete fractures	no
	Porosity	1
	Hydraulic conductivity	$\propto L^{1.87}$ m/s
	Total Compressibility	1e-10 1/Pa
Matrix		
	Porosity	0
	Hydraulic conductivity	1e-7 m/s
	Total Compressibility	1e-10 1/Pa

1.3.1 Constant Flow – Varying Concentration Scenario

Examples of kernel estimation are illustrated in Sections 1.3.1.1 and 1.3.1.2. The parametric kernel estimation approach was used first and followed by the nonparametric estimation approach. The examples are based on simulated data from Reservoir Model III. These examples are for a scenario where the flow-rates are constant but the injected tracer concentration varies over time. The injection rate for each injector was 2500 m^3/day and the injected concentration was changed every 30 days. The 550 day history of injection and production is shown in Figure 1.5.

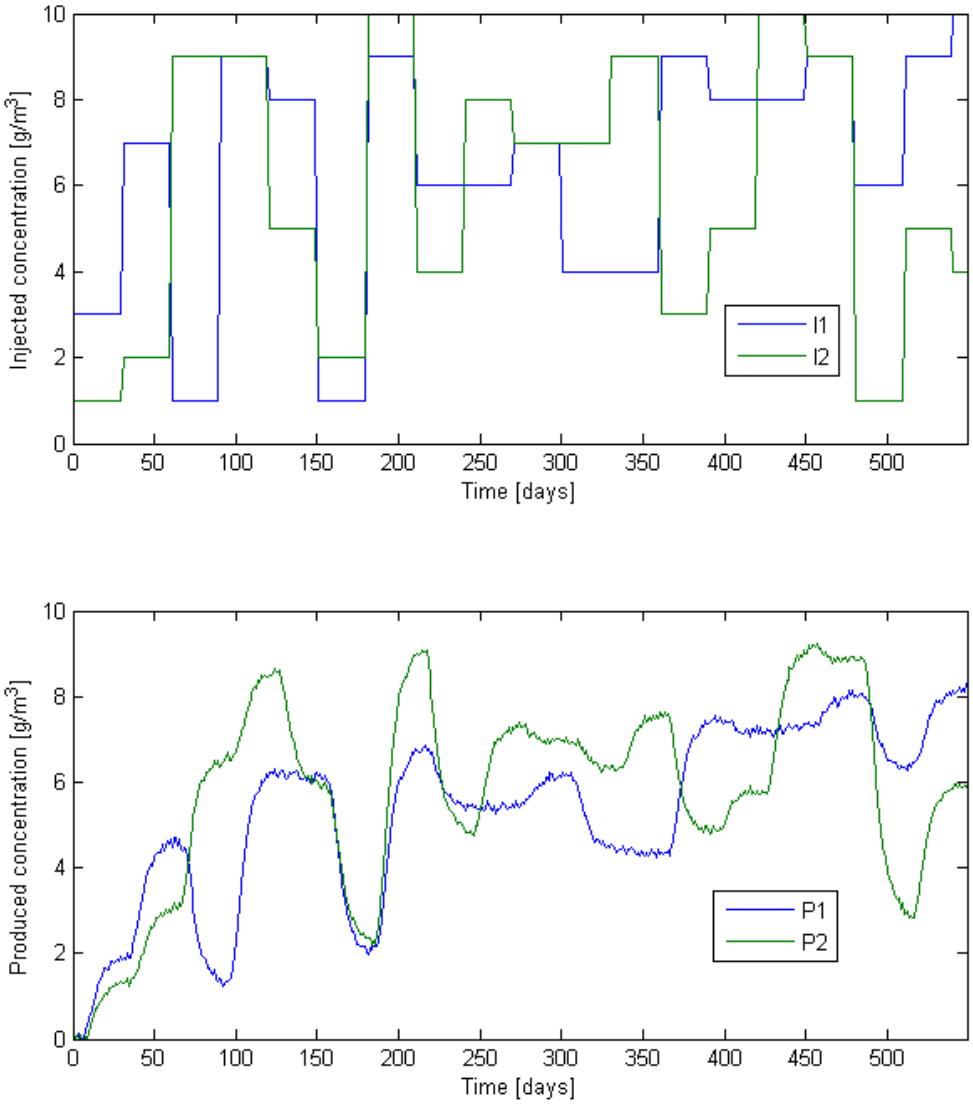

Figure 1.5: Injection and production history of tracer concentration in the constant flow - varying concentration example for Reservoir Model III.

1.3.1.1 Parametric Kernel Estimation

The first step in determining the kernels was to find a parametric estimate. Data from the first 400 days was used to estimate the kernels and then the kernel estimates were used to predict the concentration from day 400 until day 550. The resulting fit was quite good as shown in Figure 1.6, although it was not quite as accurate as that seen in the corresponding example for Reservoir Model I (see quarterly report from Fall 2011).

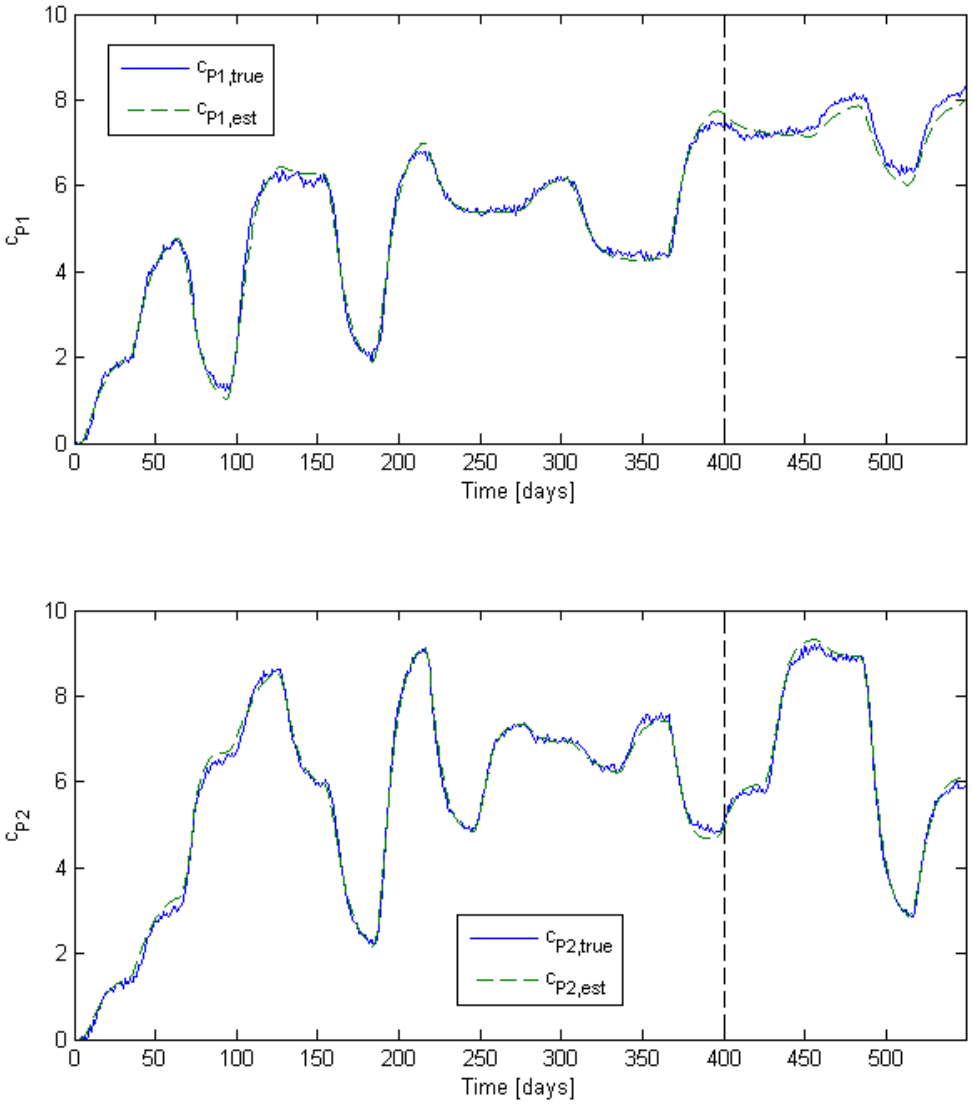

Figure 1.6: Tracer production data as reproduced from the parametric kernel estimates compared to the actual data used to calibrate the models. The true data are shown as blue solid lines and the reproduced data are given by green dashed lines. The black dashed line divides the estimation and prediction periods.

The reason for the less accurate data fit in this case becomes apparent when looking at the resulting kernel estimates in Figure 1.7. The first thing to mention in this case is that the "true" kernel estimates were hard to obtain in this case because of numerical issues in the simulation. This is seen most clearly in the estimate of the true kernel for connection I1P1, where the sinusoidal variations in the tail are numerical artifacts. Another observation to keep in mind is that the parametric model did not fully conform to the shape of the "true"

kernels, as seen for the I1P2 and I2P2 connections. One obvious reason for this is that the parametric kernels are based on equations that were derived for one-dimensional flow, while the actual kernels are generated from a flow field that is somewhere between two- and three-dimensional.

The "true" kernel for the I2P1 connections indicated that there should have been a very large pore volume separating the two wells, but this was not realized by the parametric model. A couple of reasons for this may have been that the true kernel could not be computed accurately because of numerical errors in the FEFLOW simulation, or that having this as a significant connection happened to yield a better solution to the problem. It did not seem likely that the optimization algorithm had become stuck in a local minimum because leaving the I2P1 connection out yielded significantly poorer data fits. In relative terms, however, the I2P1 kernel had small influence on the production signal because the corresponding IWC (interwell connectivity, which was computed earlier from flow-rate variation data) coefficient was very small, as shown in Table 1.2.

Table 1.2: Interwell connectivity coefficients (F_{ij}) for Model III.

F	P1	P2
I1	0.5477	0.4486
I2	0.0024	0.9871

Estimates of the pore volume (V_x), Peclet number (*Pe*) and correction factor (*f*) are given in Table 1.3. The correction factors were relatively close to one, indicating that the IWCs give a fairly good indication of the tracer connectivity for the flow-rates used in this example. The one exception is f_{I2P1} which is abnormally high. Counterintuitive results of this kind could come up when the production signal was a weak function of the input. In spite of this, the test statistic, S0, indicated that the I2P1 connection was the weakest, as shown in Table 1.4. Using a 0.01 cut-off threshold for S0, as was done in the examples for Models I and II, would mean that all of the connections should be considered significant, as shown in Table 1.5.

Table 1.3: Kernel parameter estimates for Model III, based on the constant flow - varying tracer scenario.

		P1	P2
V_x	I1	17,825	33,692
	I2	40,053	34,358
Pe	I1	6.47	3.55
	I2	3.82	10.14
f	I1	0.842	0.836
	I2	1.552	1.102

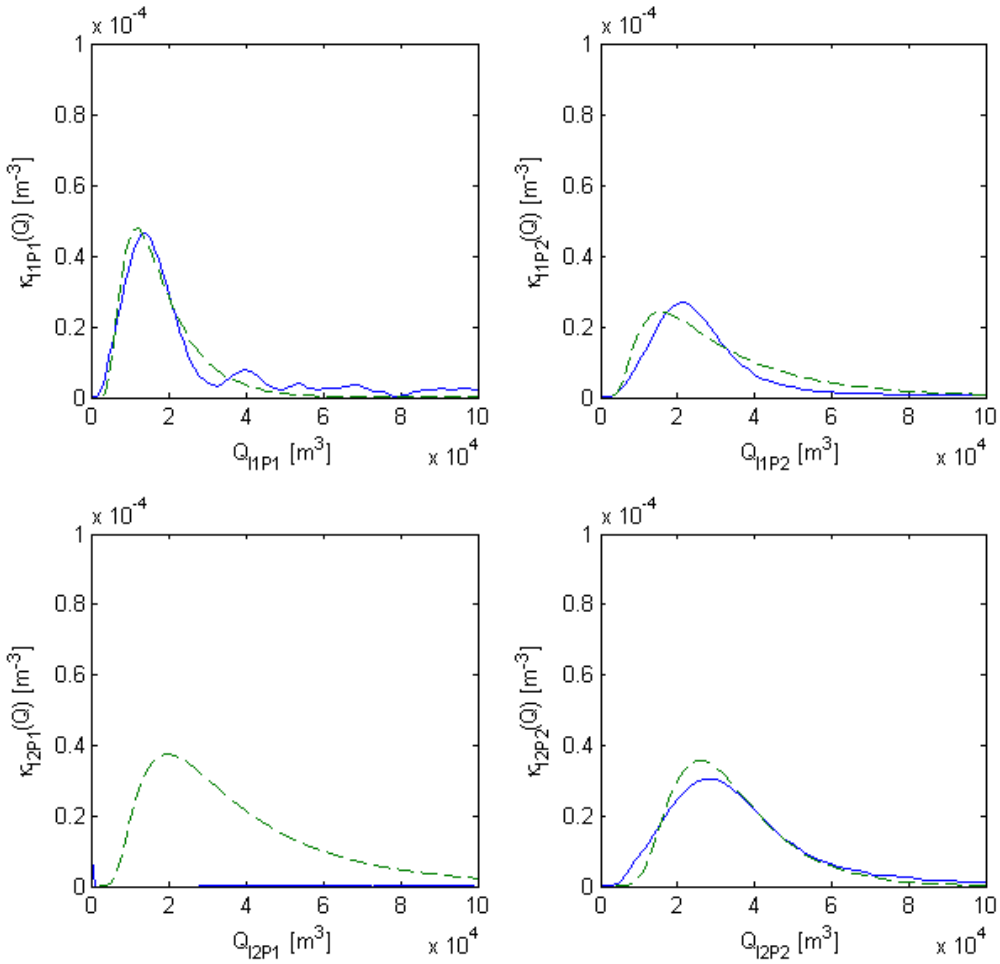

Figure 1.7: Parametric kernel estimates for each of the four injector-producer connections in Reservoir Model III. The "true" kernels are shown as blue solid lines and the parametric estimates are given by green dashed lines.

Table 1.4: Test statistic to determine the influence of each kernel in the constant flow-rate - varying concentration example for Model III.

S0	P1	P2
I1	0.8601	0.2872
I2	0.1390	0.7128

Table 1.5: List of valid injector-producer connections based on the test statistic S0 for Model III.

G0	P1	P2
I1	TRUE	TRUE
I2	TRUE	TRUE

1.3.1.2 Nonparametric Kernel Estimation

The nonparametric kernel estimates for the constant flow - varying concentration example are discussed in this section. The parametric kernels shown in Figure 1.7 were used as priors in this problem, which was solved using the nonparametric theory outlined in the quarterly report from Fall 2011. The first 400 days of production data were used to form the kernel estimates and the last 150 days were predicted using those kernels. From comparing the reproduction of data in this case (see Figure 1.8) to that obtained in the parametric case (see Figure 1.6), it is clear that the nonparametric approach brings a considerable advantage.

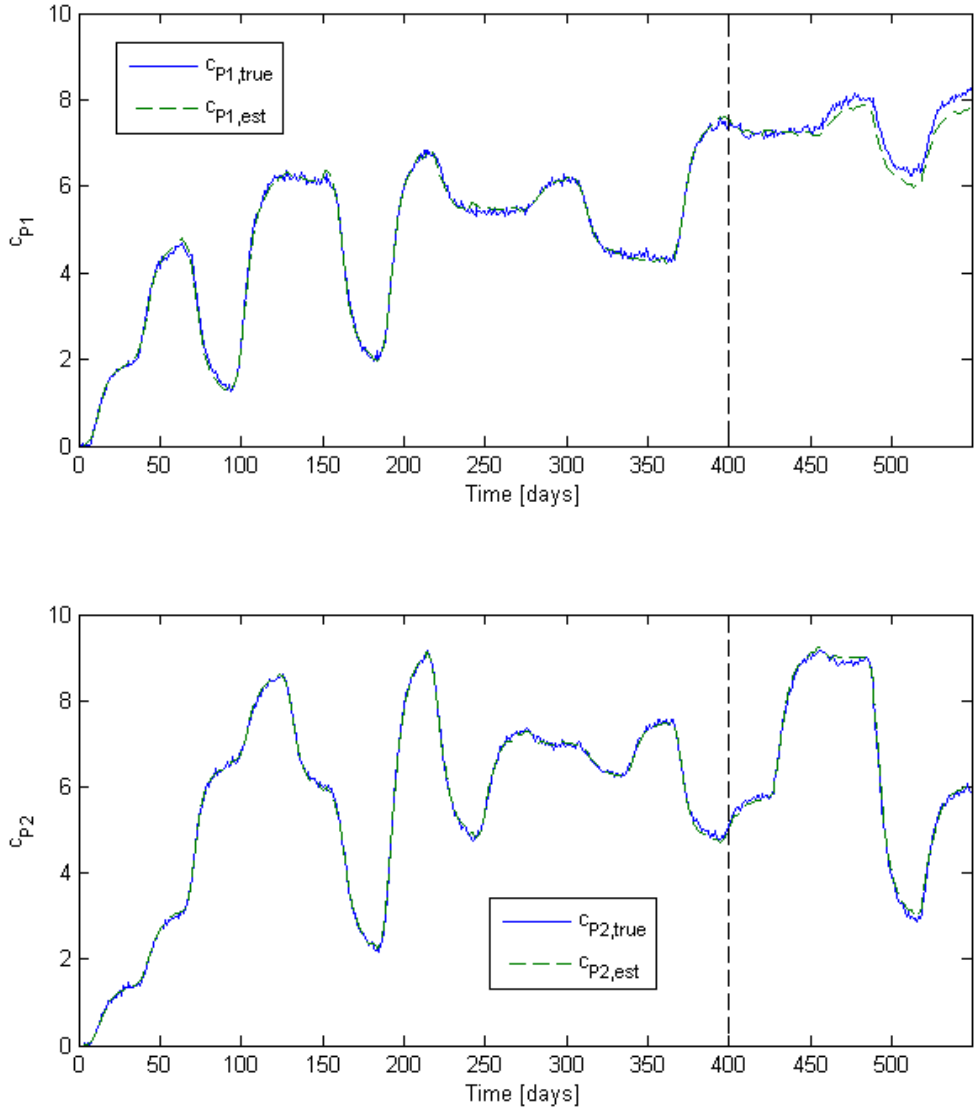

Figure 1.8: Fit to the production data from the constant flow - varying concentration example for Reservoir Model III, using nonparametric kernels. Data from the first 400 days was used for estimation of the kernels and the rest was predicted based on the kernel estimates.

The nonparametric kernels were found to be relatively smooth and they fit the true kernel estimates more accurately than did the parametric estimates, as illustrated in Figure 1.9. The clearest example of this is seen in the estimate of κ_{I1P2}. The kernel estimate for the I2P1 connection, on the other hand, is more oscillatory which would often be the tendency for estimates that were weakly constrained by the data. The pore volume and correction factor corresponding to the kernels shown in Figure 1.9 are given in Table 1.6.

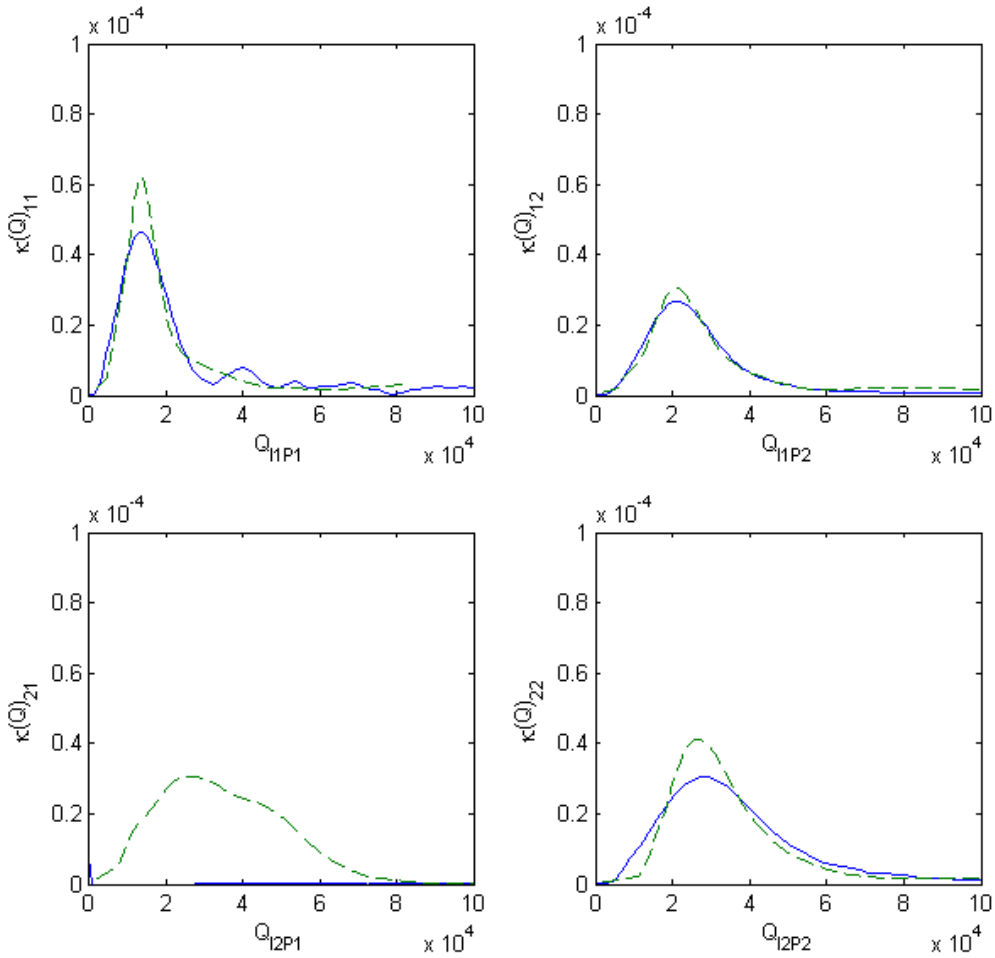

Figure 1.9: Nonparametric kernel estimates for those kernels deemed significant in the constant flow - varying tracer example for Reservoir Model III. The "true" kernels are given by blue solid lines while the estimates are in green dashed lines.

Parametric bootstrapping was used to assess confidence bounds for the nonparametric kernel estimates. These are shown in Figure 1.10. The roughness penalty multiplier (θ) was lowered by two orders of magnitude for the parametric bootstrap computations, which is why the bootstrap estimates are more oscillatory. The fact that the true kernels are not entirely encompassed by the 95% confidence intervals may indicate that the nonparametric kernel model provides an imperfect description of the process, e.g. because of discretization error. In addition to that, the representation of "true" kernels is not entirely accurate, as mentioned earlier. Nonetheless, these oscillations should not have much impact on important bulk properties like the estimated pore volume and correction factor.

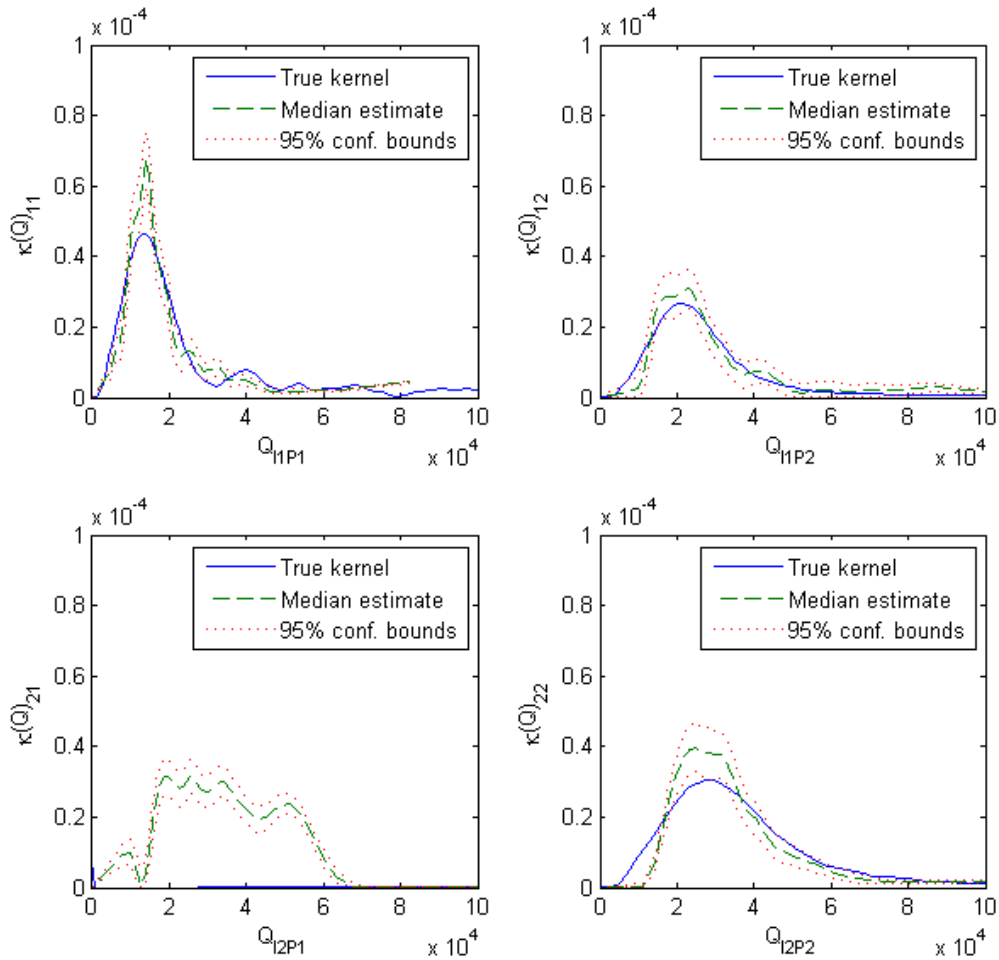

Figure 1.10: Nonparametric kernel estimates and 95% confidence bounds obtained from parametric bootstrapping for those kernels deemed significant in the constant flow - varying tracer example for Reservoir Model III.

Table 1.6: Pore volume and correction factor computed from nonparametric kernels for Model III, based on the constant flow - varying tracer scenario.

		P1	P2
V_x	I1	21,497	43,442
	I2	39,793	40,267
f	I1	0.902	0.819
	I2	1.299	1.166

1.3.2 Varying Flow – Ramp Concentration Scenario

The varying flow-rate - ramp concentration scenario was carried out with a 730 day production history as shown in Figure 1.11 and Figure 1.12. The flow-rates were changed every 100 days and the concentration in both injection wells increased linearly until day 550. After that, the injected concentration was reduced to zero. As in the previous

examples, the production rates were determined by a constant bottomhole pressure condition. The kernel estimates found in the next two sections were based on these data.

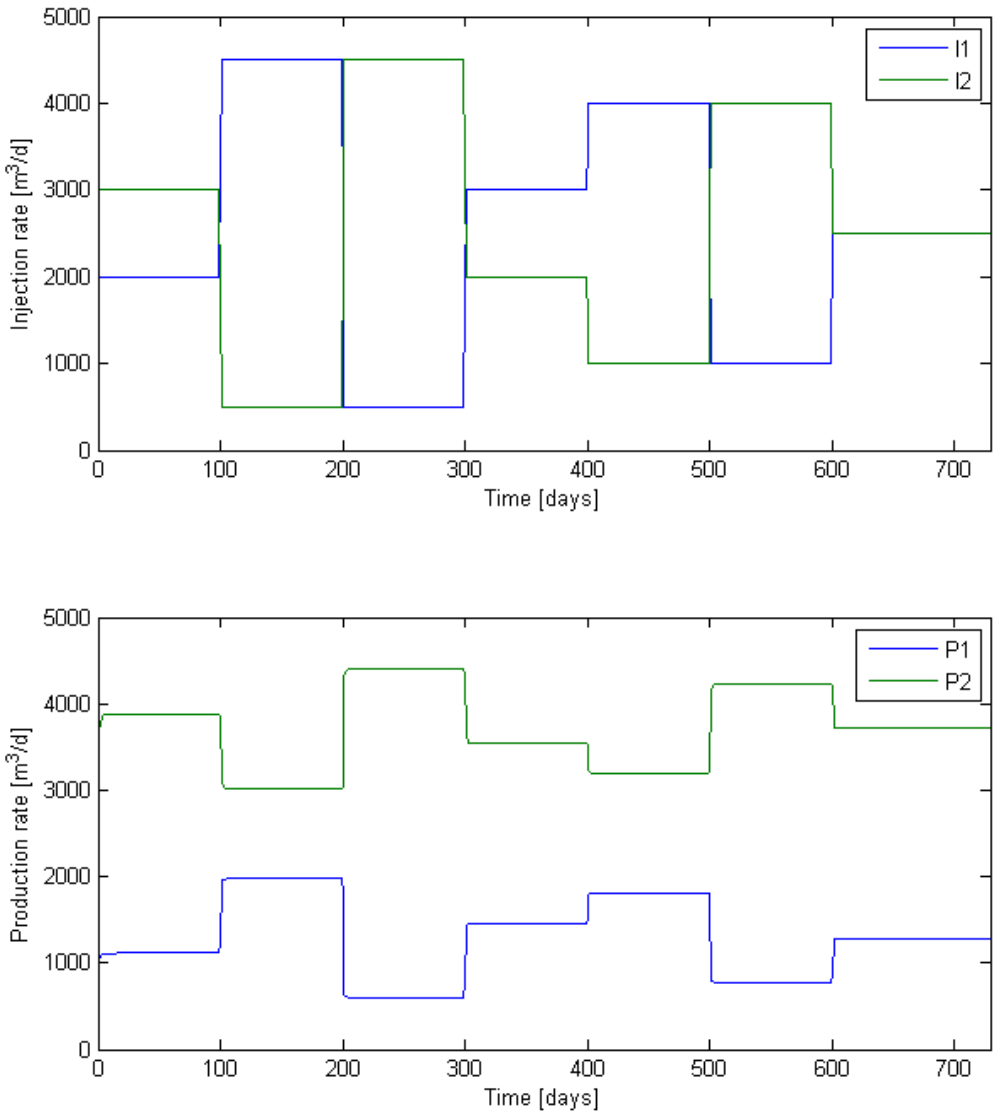

Figure 1.11: Injection and production rates in the variable flow-rate - ramp tracer example for Reservoir Model III.

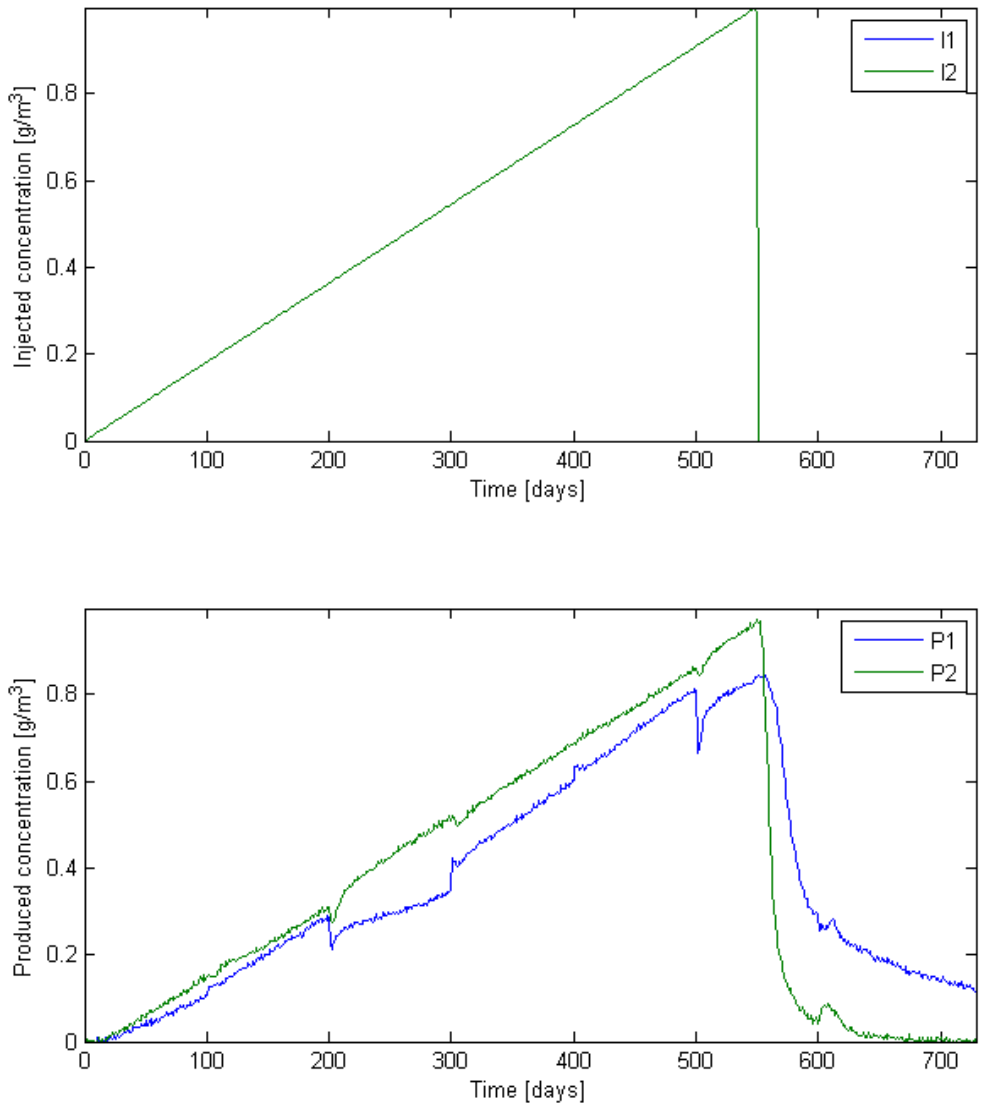

Figure 1.12: Injection and production history of tracer concentration in the variable flow-rate - ramp concentration example for Reservoir Model III.

1.3.2.1 Parametric Kernel Estimation

Using the kernel method to predict the tracer returns in this scenario, proved to be significantly more difficult, than it did with the corresponding two-dimensional example (Model I in quarterly report from Fall 2011). There could be several reasons for this; most notably the fact that the flow was no longer constrained to fractures that defined one-dimensional flow paths. There could also have been some numerical errors associated with the use of relatively large gridblocks in the simulation, and of course the transients in the production data were less informative as discussed in the previous examples for Reservoir Models I and II (see quarterly report from Fall 2011).

The parametric kernel estimation method was applied to the variable flow - ramp concentration data for Model III. Data from the first 550 days was used to obtain the kernels and the last 180 days were predicted with the kernel estimates. The resulting data fits and predictions are shown in Figure 1.13. The concentration in P1 was not captured with much accuracy in those cases where the flow-rate in P1 was small (days 200-300 and 500-600). It seems like at low flow-rate conditions, diffusive effects, that are independent of the flow-rate, start to govern the behavior of the tracer production transient, thereby breaking one of the assumptions made in the development of the tracer kernel model. The concentration in P2, which produces at considerably higher flow-rates at all times, is predicted with more accuracy.

Table 1.7: Kernel parameter estimates for Model III, based on the varying flow - ramp tracer scenario.

		P1	P2
V_x	I1	38,114	29,341
	I2	7,597	48,220
Pe	I1	4.00	4.00
	I2	4.00	4.00
f	I1	0.929	0.987
	I2	0.782	1.004

Table 1.8: Configurations of the injection rates used to illustrate the variability in tracer kernels. Injection rates are given in m^3/day.

	I1	I2
Config. 1	3750	1250
Config. 2	2500	2500
Config. 3	1250	3750

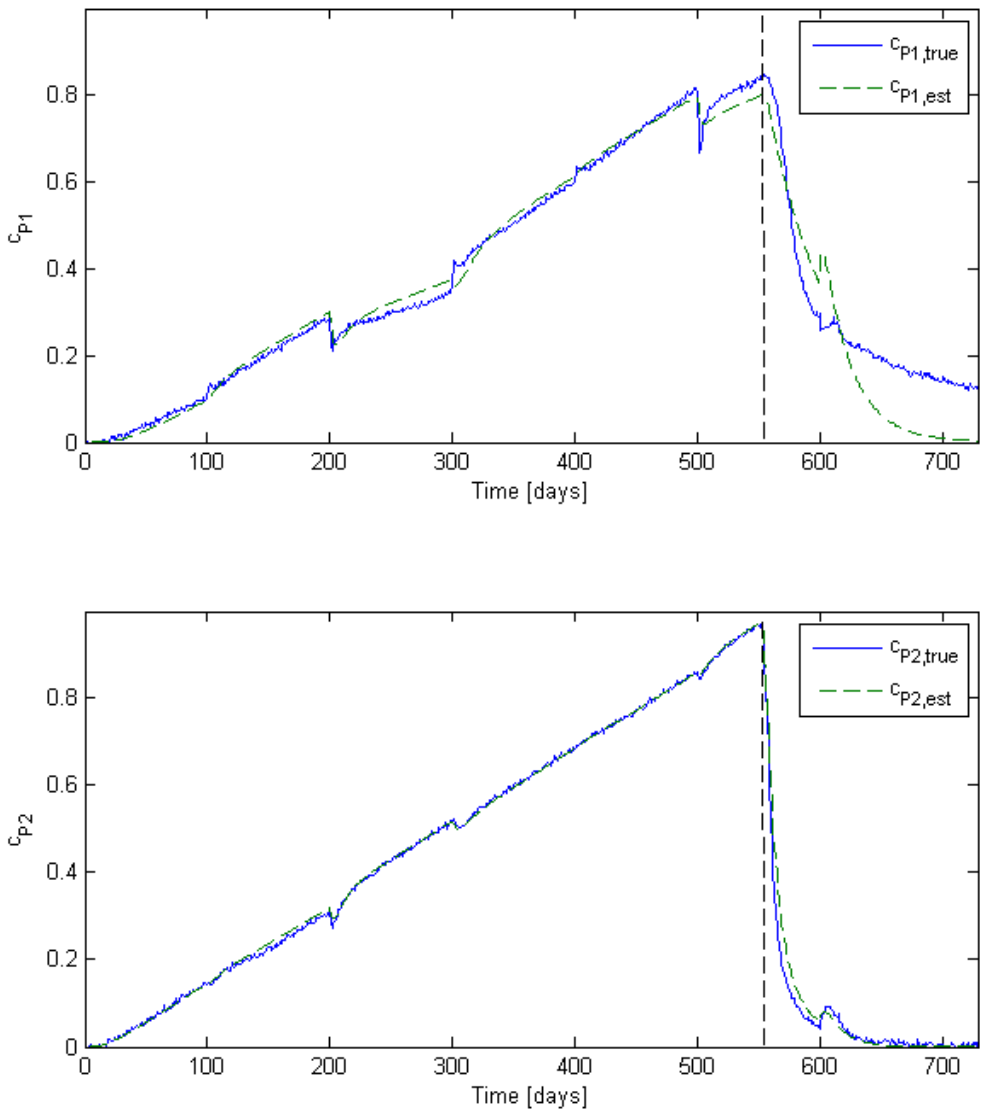

Figure 1.13: Model reproduction of the tracer production data in the variable flow-rate - ramp tracer example for Reservoir Model III. The true data are shown as blue solid lines and the reproduced data are given by green dashed lines. The black dashed line divides the estimation and prediction periods.

The resulting tracer kernel estimates are given in Figure 1.14 and the parameters for those kernels are listed in Table 1.7. The kernels are compared to "true" tracer return curves that were obtained by running constant tracer injection scenarios with the flow-rate configurations given in Table 1.8. The variability in the "true" kernels shows that there is no single kernel estimate that can capture the production signal perfectly, i.e. the kernels vary with the flow-rate configuration. In view of that, it is actually quite pleasing to see

how well the production signal in P2 was captured by the kernel model. Note also how the kernel estimates relating to P2 are something of a mixture of the three "true" kernel estimates. The kernel estimates for P1 are not particularly good, as expected, based on the reasons given in the previous paragraph.

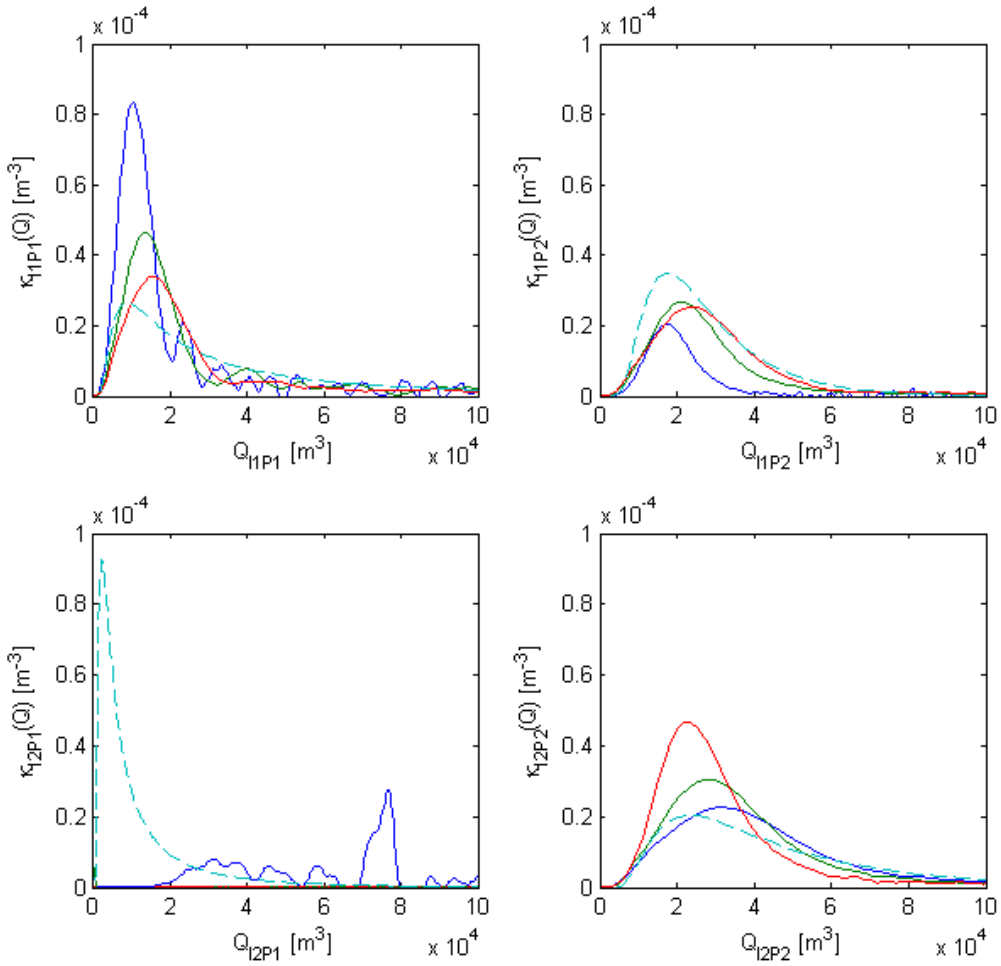

Figure 1.14: Parametric kernel estimates for each of the four injector-producer connections in Reservoir Model III. The "true" kernels for the configurations given in Table 1.8 are plotted with solid lines (Config 1: blue, Config 2: green, Config 3: red). The parametric estimates are given by cyan dashed lines.

As in the constant flow-rate case, the S0 test statistic indicated that all the kernels had significant influence on the production signal, and that the I2P1 connection should be the weakest.

Table 1.9: Test statistic to determine the influence of each kernel in the varying flow-rate - ramp concentration example for Model III.

S0	P1	P2
I1	0.7855	0.4857
I2	0.2145	0.5143

1.3.2.2 Nonparametric Kernel Estimation

The final example is for nonparametric kernel estimation with the varying flow - ramp tracer data set from Model III. In addition to the challenges mentioned in the corresponding parametric estimation example, there were some issues with utilizing the equal area discretization method (see quarterly report from Fall 2011). To fix this, the Peclet number for the parametric estimates was constrained to be above four (as seen in Table 1.7). With this restriction, the equal area method worked well, and the data were reproduced with similar accuracy as was obtained with the parametric model.

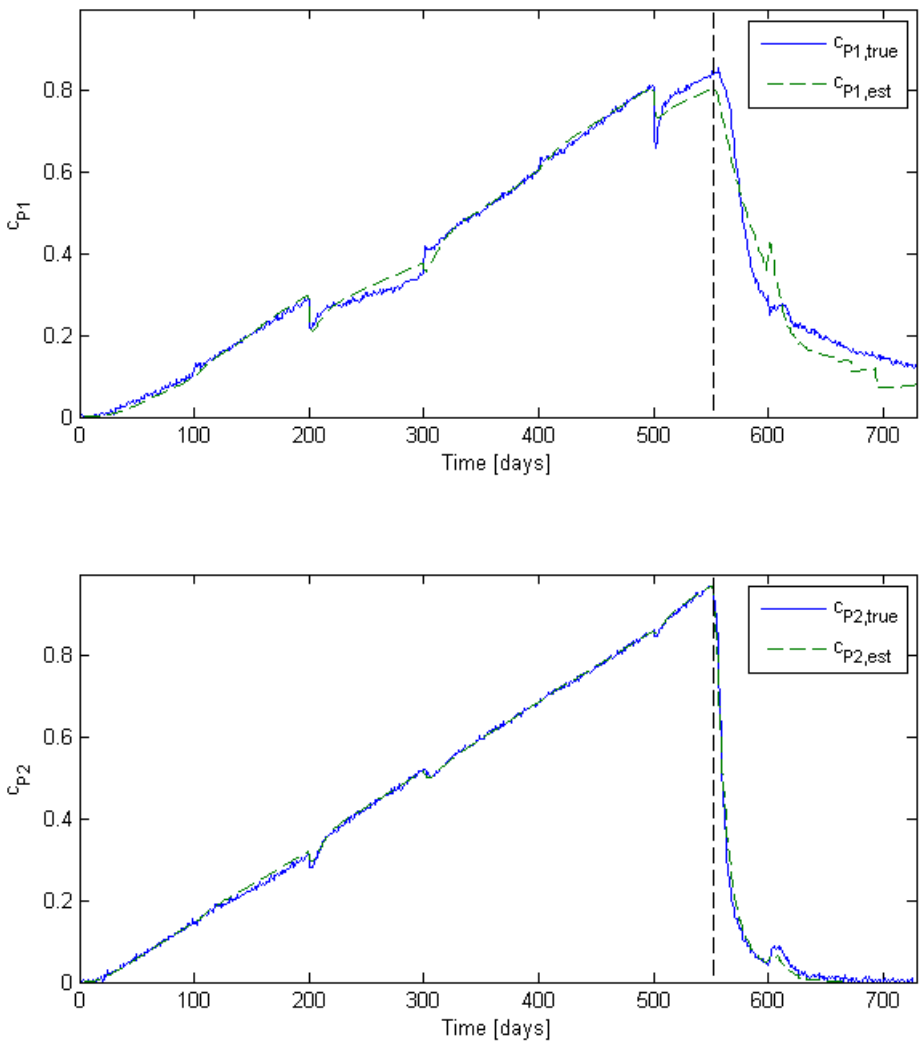

Figure 1.15: Fit to the production data from the varying flow - ramp concentration example for Reservoir Model III, using nonparametric kernels.

The kernel estimates, with confidence bounds obtained from parametric bootstrapping, are shown in Figure 1.16. The large variability in the confidence bounds is partly attributable to the fact that some of the solutions in the bootstrapping procedure converged to a local minimum. This issue could probably have been dealt with by implementing a rejection criterion on the data fit, but that will be left as future work. The estimated pore volume and correction factor are given in Table 1.10.

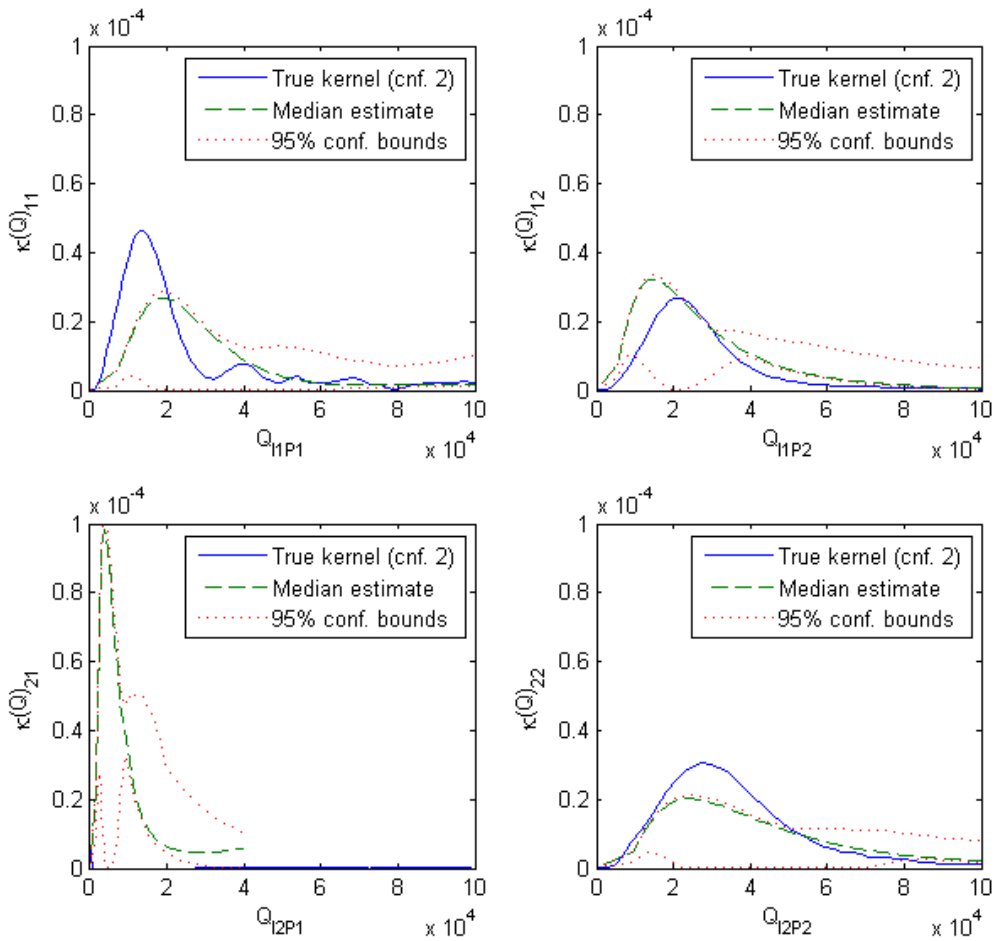

Figure 1.16: Nonparametric kernel estimates and 95% confidence bounds obtained from parametric bootstrapping for those kernels deemed significant in the varying flow - ramp concentration example for Reservoir Model III.

Table 1.10: Pore volume and correction factor computed from nonparametric kernels for Model III, based on the varying flow - ramp tracer scenario.

		P1	P2
V_x	I1	58,404	28,144
	I2	9,153	44,801
f	I1	1.021	0.990
	I2	0.806	0.999

1.4 STEP-BY-STEP METHODOLOGY

Both the parametric and nonparametric kernel estimation methods described in the quarterly report from Fall 2011 could be utilized on their own. It is suggested, however, that they be used together. This process involves the steps outlined here.

Step 1: Obtain effective injector-producer flow-rates, q_{IiPj}, using interwell connectivity. The M-ARX method (Lee et al, 2010) was used to compute interwell connectivity for all of the examples in this report. Transient flow-rate data for both injectors and producers were required to obtain the M-ARX based interwell connectivity matrix, **F**.

Pressure based interwell connectivity (Dinh, 2009) can be used when only pressure data are available and the Interwell Transmissibility Method (quarterly report from Spring 2011, Section 1.4) can be used if both pressure and flow-rate data are available.

Step 2: Find kernel estimates using the parametric kernel estimation method. The method relies on interwell connectivity estimates to compute mixing weight and effective injector-producer flow-rates. Flow rates and transient injection and production concentrations are required for this step.

Step 3: Use test statistic S0, which is based the parametric kernel estimates and the interwell connectivities, to determine which well-to-well connections can be ignored.

Step 4: Find nonparametric kernel estimates for those injector-producer connections deemed significant in Step 3. Use parametric kernel estimates, from Step 2, as priors for the nonparametric kernel estimates. The data required for Step 2 are used again here.

Step 5: Use parametric bootstrapping to obtain confidence bounds for the nonparametric kernel estimates.

1.5 THERMAL TRANSPORT IN A THREE-DIMENSIONAL RESERVOIR MODEL

In practice, it is useful to have a simple analytical model to describe the well-to-well connections in reservoirs, e.g. for the purpose of optimizing reinjection into the reservoir. Most analytical models for thermal transport in fractured reservoirs are based on the assumption that the flow-rate remains constant. Moreover, the fracture and surrounding matrix must have a relatively simple structure. In the annual report for 2010-2011 it was

shown that the analytical model developed by Lauwerier (1955) could be used to model thermal transport in two-dimensional fractured reservoirs quite accurately. This model was developed for flow through a one-dimensional fracture surrounded by two-dimensional matrix slabs.

The interwell connectivity and parameters derived from the tracer kernel can be used to calibrate Lauwerier's thermal transport model. The main uncertainty in the this approach is associated with the fracture aperture. Effective methods to determine the aperture, at the onset of injection, have not been well established. Kocabas (2005) suggested using injection-backflow testing to obtain the effective aperture, but a value obtained by that method could be unreliable for characterizing well-to-well connectivity. Reimus et al. (2011) talked about using thermally degrading tracers to characterize the heat transfer area for well-to-well connections. The method is still in development but seems promising, especially as it builds on similar analytical equations to those that have been used in this research, i.e. those given by Maloszewski and Zuber(1985). The basic idea is to inject two tracers, dissolved in cold water, at the same time into the reservoir. One tracer should be thermally stable, and the other should have known thermal degradation properties. By comparing the returns from the two tracers, one can infer how far the cold front has progressed, which means that the effective heat transfer area, or the effective aperture, can be found.

When it came to modeling thermal transport for three-dimensional models (Model III) the Lauwerier solution did not work very well, as the flow field was not constrained by one-dimensional fractures. Instead, the injector-producer pairs were connected by relatively large two-dimensional fractures, with the exception of the I2P1 pair. Simulations of mass and energy transport were run on Model III with the injection rate and temperature conditions listed in Table 1.11.

Table 1.11: Flow rate configurations and injection temperatures for different thermal simulation runs with Reservoir Model III.

	I1 [m3/d]	I2 [m3/d]	I1 [C]	I2 [C]
Conf. 1	5000	20000	50	150
	5000	20000	150	50
Conf. 2	10000	15000	50	150
	10000	15000	150	50
Conf. 3	15000	10000	50	150
	15000	10000	150	50
Conf. 4	20000	5000	50	150
	20000	5000	150	50

The resulting thermal drawdown curves are shown in Figure 1.17. The figure shows that no cooling was seen in producer P1, in any of the scenarios, when water at 50°C was injected into well I2. Thermal drawdown was seen in all of the other wells, for all other scenarios, although very little cooling was seen in P2 at Configuration 1, with cold water injection in I1.

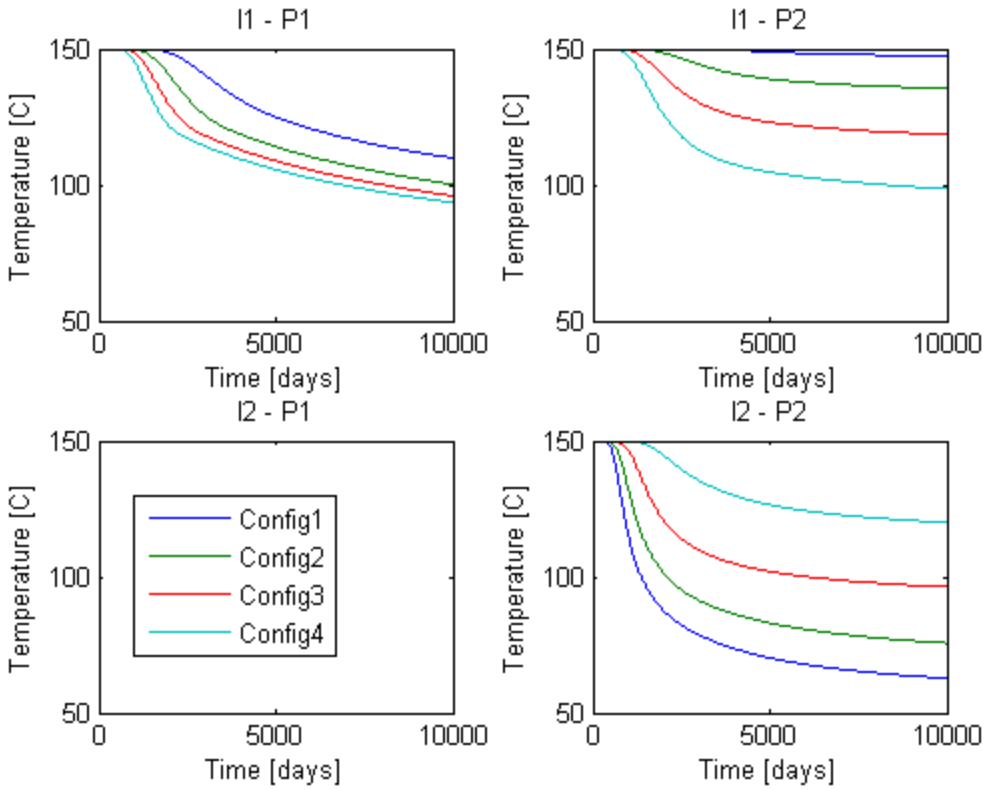

Figure 1.17: Simulated thermal breakthrough for Reservoir Model III. Note that the I2P1 connection showed no thermal breakthrough and thus the production temperature remained at 150 C for the entire 10000 day period.

The thermal breakthrough curves for Reservoir Model III took on a shape that differed significantly from that seen in the two-dimensional reservoir model examples. The Lauwerier (1955) model could not capture the breakthrough behavior very well, as shown in Figure 1.18, where the fracture aperture that gave the best fit to the data has been chosen. Although the leading cause for the apparent shortcomings of this model has not been fully determined, a few potential explanations will be offered.

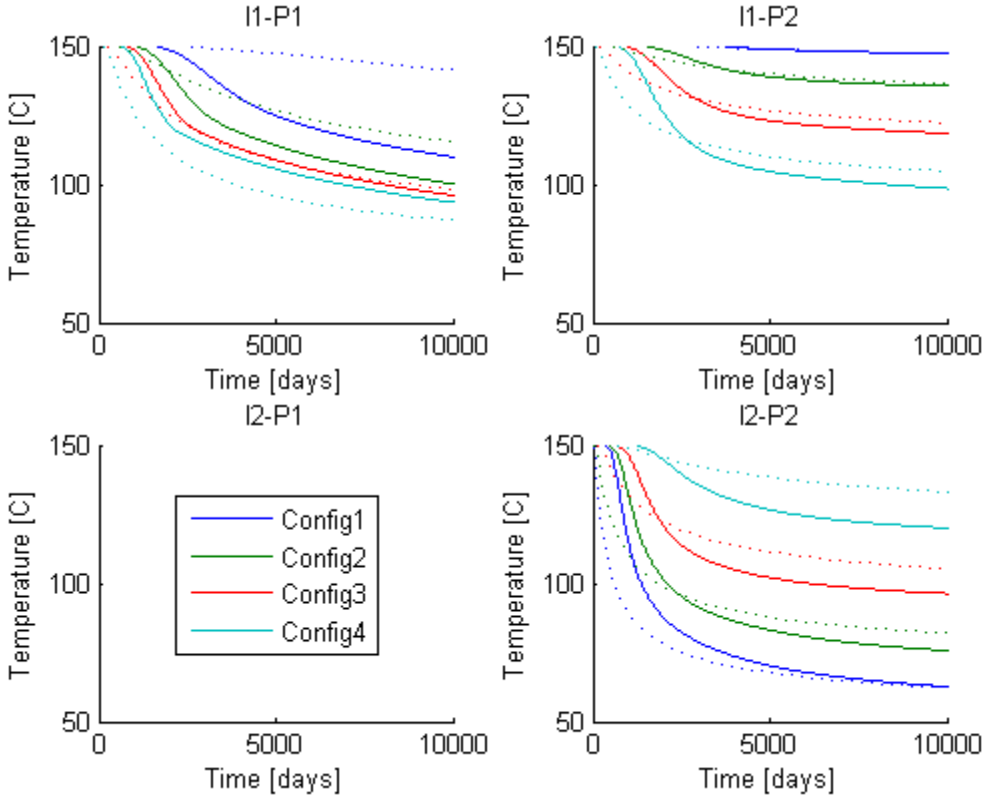

Figure 1.18: Comparison of simulated thermal breakthrough and Lauwerier's (1955) analytical solution for Reservoir Model III. The simulated values are presented with solid lines and the fitted analytical responses have dotted lines.

One potential reason could relate to the fact that the wells in Model III were vertical and each one of the major fractures was slightly tilted. Therefore, the wells intersected the fractures at a single point, although, because of the upscaling this single point may have gotten distributed over two or three gridblocks. The essential observation is that, because of this, the streamlines between the wells formed in a two-dimensional plane with a point source and sink. Thus, a streamline based model similar to that proposed by Gringarten and Sauty (1975) might resolve the issue. A simple analytical streamline model for a well doublet in an infinite plane, presented by Barker (2010), was used to look into this option. This approach did not capture the thermal drawdown well either, but perhaps a streamline model that is constrained to a finite plane would yield better results.

Another explanation of this discrepancy could relate to the complexity of the fracture network. The return profile could be affected significantly by thermal returns coming from two or more fracture paths. This could perhaps be captured by fitting linear combinations of these models to the drawdown curves.

Finally, it should be mentioned that the dispersivity coefficients for Reservoir Model III were set to relatively low values, as shown in Table 1.1. The dispersivities were 50 times smaller for Model III than they were for Models I and II. The effects of this were tested by

running Model III with higher dispersivities but that did not explain the mismatch fully. However, it might be useful to implement the Malozewski and Zuber (1985) model to be able to capture this ambiguity in the dispersion term.

1.6 CONCLUSION

In this quarterly report the application of the tracer kernel method for flow through a three-dimensional fractured system was reviewed. The results showed that the nonparametric tracer kernels were able to capture the tracer transfer functions quite accurately for constant flow-rate conditions. The tracer kernels were less representative for the varying flow-rate case because of the inherent variability in the three-dimensional flow field.

It was noticeable from the examples given in Section 1.3 (and also the quarterly report from fall 2011) that the tracer kernels were considerably more difficult to infer when the flow-rates and tracer concentrations varied simultaneously. A step-by-step methodology for inferring the tracer kernels was outlined in Section 1.4.

The applicability of using analytical thermal transport models to predict thermal breakthrough in a three-dimensional fractured reservoir was considered in Chapter 1.5. The results showed that the Lauwerier (1955) model, that had worked well with two-dimensional discrete fracture models, did not predict the thermal decline accurately for flow through a three-dimensional fractured reservoir. The leading reasons for this shortcoming have not been fully understood. We speculate that it has to do with the distribution of flow through the two-dimensional plane defined by the major fractures connecting wells in the reservoir.

2. FRACTURE CHARACTERIZATION OF ENHANCED GEOTHERMAL SYSTEMS USING NANOPARTICLES

This research project is being conducted by Research Associates Mohammed Alaskar and Morgan Ames, Senior Research Engineer Kewen Li and Professor Roland Horne. The objective of this study is to develop in-situ multifunction nanosensors for the characterization of Enhanced Geothermal Systems (EGS).

2.1 SUMMARY

During this quarter, flow experiments were carried out in a fractured rock plug using 2 µm and 2 µm fluorescent microparticles to examine variable suspension concentration and fluid velocities. The recovery of 2 µm particles was found to be highly sensitive to suspension concentration, while that of the 5 µm was found to be highly sensitive to the fluid velocity (i.e. pressure gradient). The sensitivity of the recovery of 2 µm particles to concentration was likely due to a higher susceptibility of 2 µm particles to aggregation than that of 5 µm particles, leading to more aggregation at high concentrations and, subsequently, more trapping via straining. Meanwhile, the sensitivity of the recovery of 5 µm particles to fluid velocity was likely due to the larger gravitational forces and fluid drag forces acting on the larger particles and the fact that higher fluid drag forces corresponding to higher fluid velocities can directly offset gravitational forces (whereas particle aggregation cannot necessarily be offset significantly by a higher fluid velocity).

To investigate the processes that govern particle transport in experiments and ultimately in the reservoir, we began to perform pore-scale simulation of nanoparticle and microparticle flow for various pressure gradients, particle sizes, particle densities, and injection conditions. The model accounts for fluid drag, gravity, and electric forces, and the results demonstrate the shifting balance between these forces at different conditions.

2.2 INTRODUCTION

Last quarter, we investigated the flow mechanism of silica microspheres through the pore spaces of a micromodel. We fabricated a micromodel made of an etched image of Berea sandstone pore network into a silicon wafer. Transport of the silica microspheres was analyzed by acquiring images using an optical microscope. Work was also performed to adapt an emulsion synthesis route reported for monodisperse bismuth nanoparticles with the goal to synthesize monodisperse tin-bismuth nanoparticles.

This quarter, we began to investigate the transport of fluorescent silica microparticles (with twice the density of the water used as the suspension fluid) in a fracture-matrix system. For this purpose, core-flooding experiments were conducted using a fractured sandstone core plug. Influence of particle size, concentration and fluid velocity on particle transport was addressed. Particle transport was assessed by measuring breakthrough curves, which were constructed using fluorometry measurements on collected effluent samples.

This quarter, we began to perform pore-scale particle tracking simulations in order to improve our quantitative understanding of the experiments and to help determine which

nanomaterials exhibit favorable transport under different geochemical conditions in the reservoir, and thus meet the first selection criterion for geothermal temperature sensors. Modeling performed thus far accounts for fluid drag, gravitational, and electric forces. Ultimately, chemical bonding forces, particle straining due to size exclusion, and particle aggregation will be incorporated into these modeling efforts.

2.3 FRACTURE FLOW EXPERIMENTS

2.3.1 Fluorescent silica microparticles

Fluorescent silica particles were used in the experiments. These microsphere particles have a narrow size distribution with an average diameter of 2 and 5 µm, labeled with blue and green fluorescent dye, respectively. The excitation and emission of the blue and green fluorescent dyes were 360/430 nm and 480/530 nm, respectively. The particle size was confirmed by Scanning Electron Microscopy (SEM), as depicted in Figure 2.1. These microspheres had a density in the range between 2.0 to 2.2 g/cm^3. The microspheres employed were negatively charged as per the manufacturer. Five different measurements of zeta potential (ζ) (i.e. conversion of electrophoretic mobility to zeta potential using the Smoluchowski equation, (Bradford et al., 2002)) were performed and the average zeta potentials were found to be -40.2 mV (standard deviation: 0.4 mV) and -80.23 mV (standard deviation: 1.77 mV) for particle size 2 and 5 µm, respectively. All silica suspensions were diluted to three distinct concentrations ($C = 0.5, 2C = 1\ and\ 3C = 2\ mg/cm^3$).

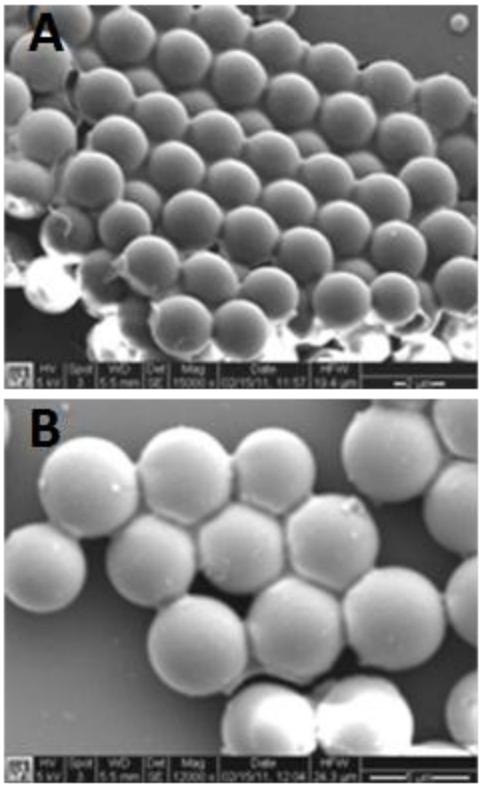

Figure 2.1: SEM micrographs of (A) blue and (B) green fluorescent silica particles.

2.3.2 Sandstone Core Preparation and Characterization

The Berea sandstone core plug used this experimental study was 3.78 and 2.56 cm in diameter and length (Table 2.1), respectively. The core plug was fired at 700ºC for 2 hours. This firing process was implemented because it stabilizes the indigenous fines and produces strongly water-wet conditions (Syndansk, 1980; Shaw et al., 1989). Prior to saturation, the core plug was dried under vacuum pressure of 0.09 MPa at 70 ºC for 24 hours. The core was then saturated with testing fluid (i.e. ultrapure water using Q-Millipore) inside the core-holder. The saturation was accomplished by evacuating the system (core plug and connecting tubing) to vacuum pressure below 50 millitorr. The system was left under vacuum for about 4 hours to ensure complete evacuation. The pure water was then introduced and the remaining vacuum was released to aid the process of saturation.

The rock sample was characterized in terms of its porosity, matrix permeability, grain density and pore size distribution. The porosity of the core plug was measured using by resaturation of the core (weight difference before and after saturation with testing fluid of known density), Helium expansion (gas pycnometer) and mercury intrusion methods and found to be 22%, 21.4% and 20.3%, respectively. The grain density measured by the gas pycnometer was 2.67 g/cm^3 and that by mercury intrusion was 2.57 g/cm^3. Matrix permeability was measured by introducing flow at different flow rates. The average matrix permeability was approximately 0.51 darcy. The pore size distribution (Figure 2.2) was obtained from the capillary pressure-saturation curve measured by mercury intrusion and Laplace's equation of capillarity. According to this approach, the Berea sandstone has pores in the range from few nanometers (5 nm) to as large as 50 µm in diameter, with the majority below 25 µm (d90). The average pore size (d_{50}) or (d50) was approximately 15.5 µm. The pore distribution also indicated that 10% of the total pores are smaller than 8 µm (d10).

Table 2.1: Summary of fractured Berea sandstone properties.

Diameter (cm)	*Length (cm)*	*Porosity (saturation)*	*Pore volume (cm3)*	*Matrix perm. (darcy)*	*Total perm. (darcy)*	*Aperture (µm)*		*Mean grain size (µm)*	*Mean pore size (µm)*
						Max.	*Min.*		
3.78	*2.56*	*0.22*	*6.3*	*0.51*	*1.2*	*62.4*	*3.79*	*150*	*15.5*

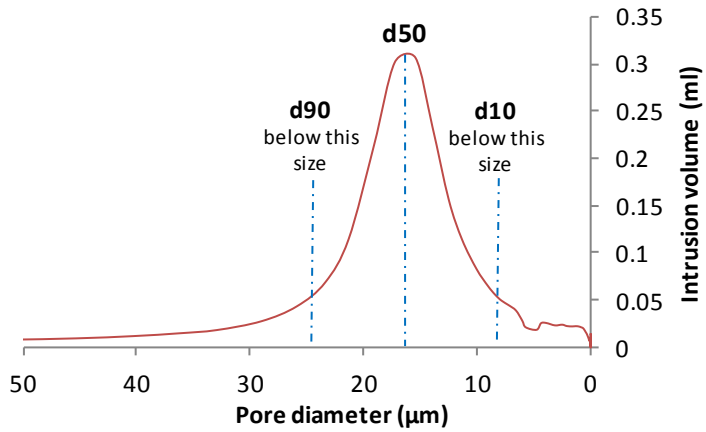

Figure 2.2: Pore size distribution of Berea sandstone obtained by mercury intrusion, indicating an average pore diameter of about 15.5 µm, 90% of pores are smaller than 25 µm and 10% are smaller than 8 µm.

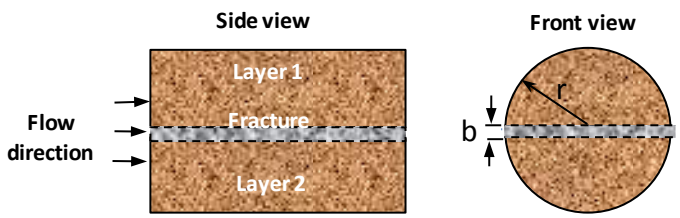

Figure 2.3: Schematic of the sandstone core plug with the location of the fracture. The fracture extends from the inlet to the outlet.

The fracture was created by saw-cutting the core plug into two pieces at the center. A schematic of the core showing the location of the fracture is depicted in Figure 2.3. The two pieces were then brought together using shrinking tube. The hydraulic aperture of the fracture was estimated by considering the flow in parallel layers. Under conditions of flow in parallel layers, the pressure drop across each layer is the same. The total flow rate is the sum of flow rate in each layer. That is:

$$Q_t = Q_1 + Q_2 + Q_f \tag{2.1}$$

using Darcy's Law of incompressible horizontal fluid flow $Q = kA(\Delta p)/\mu L$,

$$k_t A_t = k_1 A_1 + k_2 A_2 + k_f A_f \tag{2.2}$$

since $k_1 = k_2 = k_m$ and assuming $A_t = A_1 = A_2 = \pi r^2$, $k_f = b^2/12$ (cubic law) and $A_f = 2br$, then Equation (6) becomes:

$$b = \sqrt[3]{6\pi r(k_t - k_m)} \tag{2.3}$$

where r is the radius of the core plug in meter, k_t and k_m are the total and matrix permeability in square meters, respectively. Note that the matrix permeability (k_m) was determined before introducing the fracture. The hydraulic aperture of the fracture varied between 17.9 to 62.4 µm at different confining pressure ranging from 8.5 to 50 atmospheres. Since all particle injections were performed under confining pressure of 8.5 atmospheres, the maximum hydraulic aperture in these experiments was estimated to be 62.4 µm ($k_t = 1.20$ darcy) using flow in parallel layers (Equation 8). The minimum aperture was approximated to be 3.79 µm by assuming the fracture permeability to be equal to the total permeability (1.2 darcy).

2.3.3 Experimental Setup and Procedures

A schematic of the experimental setup employed for the particle transport studies is given in Figure 2.4. It consists of ultrapure water container, water pump, injection loop, syringe, differential pressure transducer and a core-holder. Effluent samples were then analyzed by standalone fluorimeter. Water ($\rho_w = 0.997$ g/cm^3, $\mu_w = 0.982$ cp at 21ºC) used throughout the experiments was purified using Millipore (A10) equipped with 0.220 µm filter, and deaerated at 50 millitorr vacuum for at least 30 minutes prior to use. Particles were injected using syringe through the injection loop. The injection loop allowed an alternating injection of particle suspension and particle-free water, without interrupting the flow. Volumetric flow rates were varied between 1 to 10 cm^3/min using pump equipped with standard head manufactured by Dynamax. The pump flow rate was calibrated using stop watch and balance (Mettler PM300) with 0.01 gram accuracy. The differential pressure across the core plug was measured using differential pressure transducer (Validyne Model DP215-50) with low pressure rating diaphragm. The transducer was calibrated with standard pressure gauge with accuracy of 1.25% of full range.

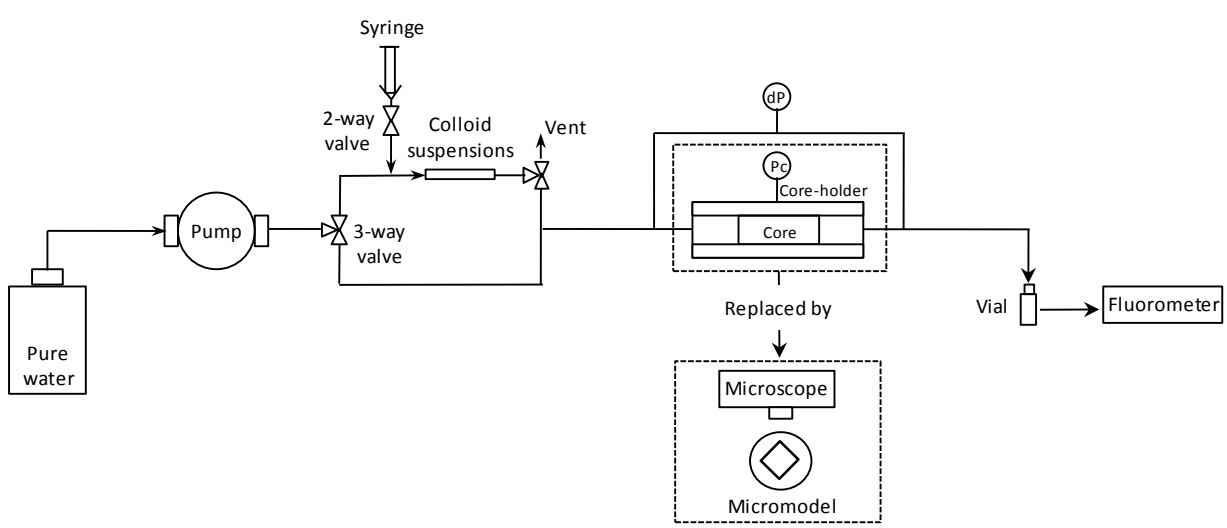

Figure 2.4: Schematic of the experimental setup employed in the particle transport studies.

Prior to the injection of the particle suspensions, the core was preflushed with pure water to displace rock fines and debris. The preflushing samples were analyzed to elucidate the existence of any naturally occurring particles. The injection sequence involved the introduction of the particle suspension slug followed by a continuous injection of pure water. In particular, the volume of particle suspension injected in to the core was 2.5 cm^3. Subsequently, a continuous flow of pure water (post-injection) was carried out. Depending on the experiment, a few pore volumes of pure water were injected while the effluent samples were collected. The total time of the experiment, flow rates and frequency of sampling were also experiment dependent. To investigate the influence of particle size, concentration and fluid velocity on the transport of particles through the core plug, 13 injections were conducted. For each particle size, every suspension concentration $(C, 2C\ and\ 4C)$ was injected at 1 and 3 cm^3/min. In addition, the 5 µm particle suspension at concentration (C) was injected at 10 cm^3/min. The breakthrough curves of the silica microspheres were determined by measuring the emission spectrum and correlating it to the effluent concentration using a calibration curve. To construct the calibration curve, the emission spectra of a few dilution samples of known concentrations were acquired. The emission intensity at the maximum peak was then plotted against the dilution concentrations, and the intensity-concentration data were fit by a linear correlation. The concentration of collected effluents was then determined using this linear correlation based on their emission intensity.

2.4 PORE-SCALE FLOW SIMULATION OF NANOPARTICLES AND MICROPARTICLES

In order to understand which forces have dominant effects on particle transport in porous and fractured media under various conditions, it is necessary to model these processes at the pore-scale. Thus, fluid drag, gravity, size exclusion, and both particle-matrix and particle-particle electric and chemical bonding forces must be modeled as distinct terms in order to better understand experimental results and have any predictive power regarding which nanomaterials can be transported through a reservoir at reservoir conditions. This quarter, simulations were performed using the Particle Tracing Module in COMSOL Multiphysics accounting for fluid drag, gravity, and electric forces.

2.4.1 Model Geometry and Velocity Field Solutions

Before modeling the flow of nanoparticles at the pore-scale, it is first necessary to model the flow field in the pore space. Keller et al. (2011) constructed a pore scale model to mimic the geometry of a micromodel, which was in turn generated from SEM images of rock thin sections. This model was used to solve the Navier-Stokes equation numerically for laminar flow for the velocity field and pressure distribution in a 640 µm by 320 µm section of the micromodel given a horizontal pressure drop of 0.715 Pa between the inlet (right face) and outlet (left face). The resulting velocity field and pressure distribution generated by Keller et al. are shown in Figure 2.5 and 2.6, respectively.

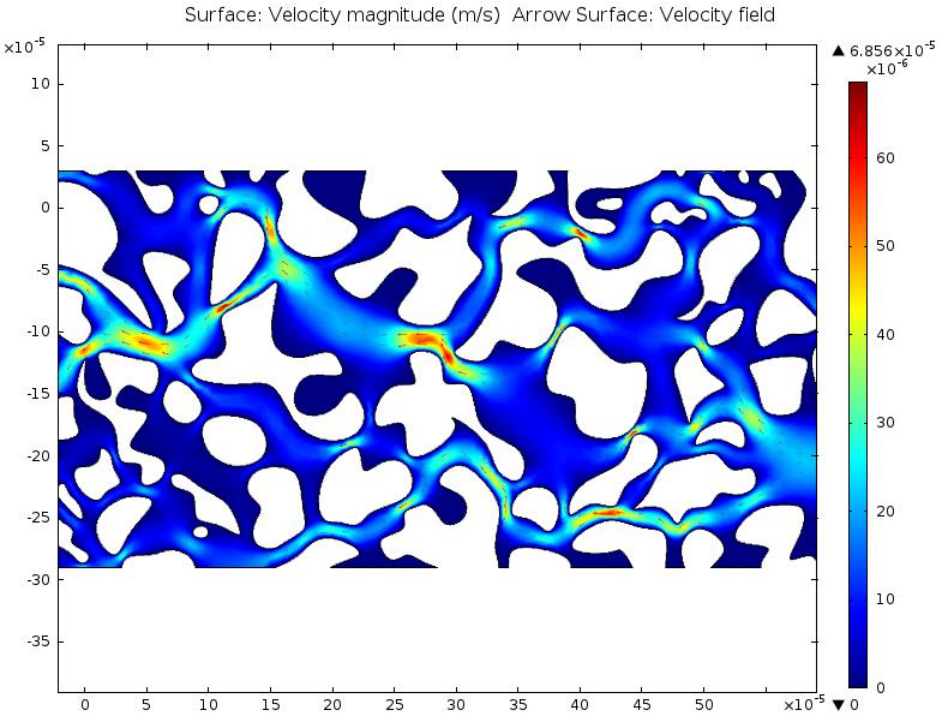

Figure 2.5: Velocity field in two-dimensional pore space for a pressure drop of 0.715 Pa/640 µm (Keller et al., 2011).

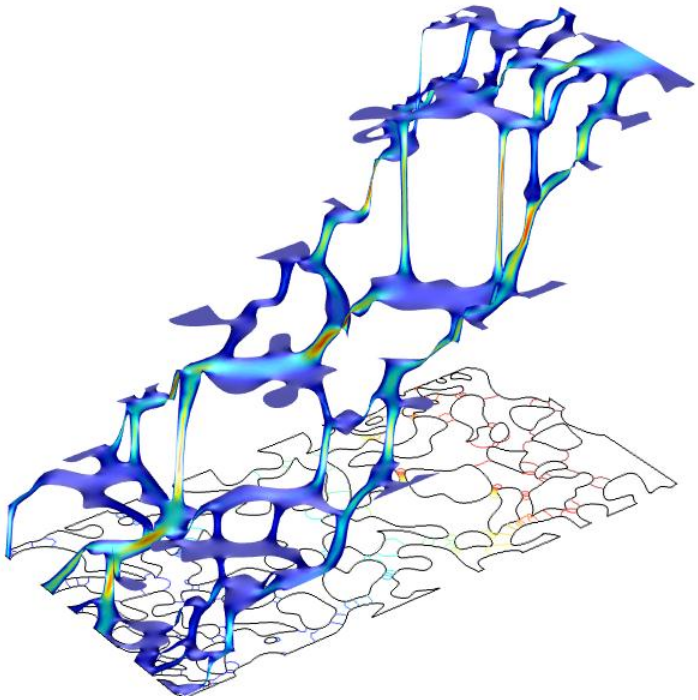

Figure 2.6: Velocity field and pressure surface in two-dimensional pore space for a pressure drop of 0.715 Pa/640 µm (Keller et al., 2011).

The pore space geometry and velocity field (Figure 2.5) generated by Keller et al. were used in the particle tracking simulations described in this report. Ultimately, a pore scale model will be constructed to mimic the geometry of the micromodel used in our experiments. To investigate the effect of variable pressure gradient in the particle tracking simulations, we also calculated the velocity field at a pressure gradient of ~250 Pa/ 640 µm, which is the average pressure gradient in the micromodel experiments described last quarter. The resulting velocity field and pressure surface are shown in Figures 3 and 4, respectively.

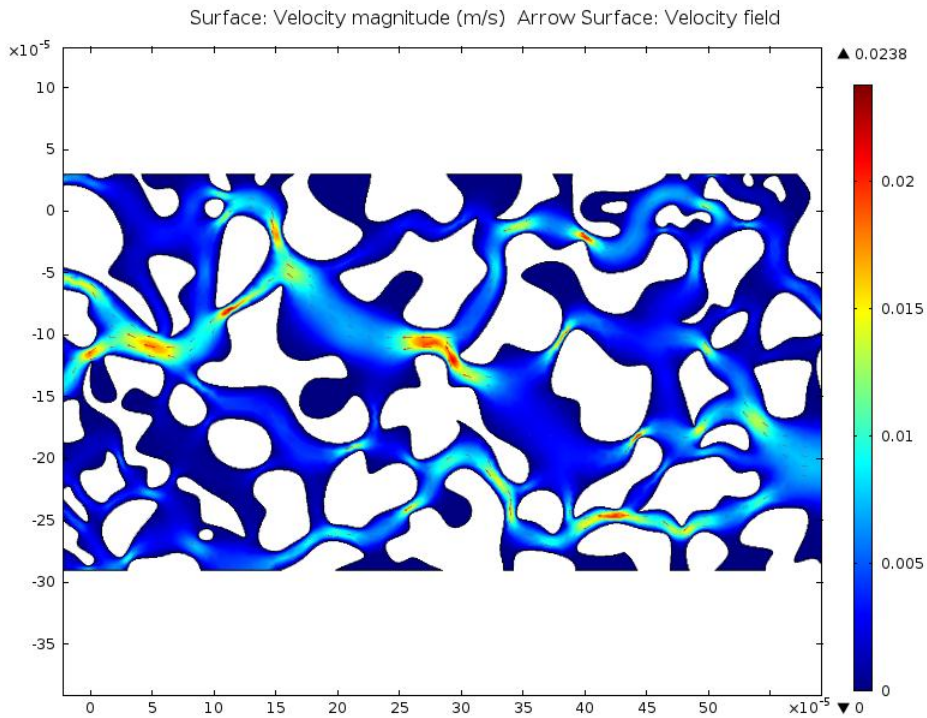

Figure 2.7: Velocity field in two-dimensional pore space for a pressure drop of 250 Pa/640 µm.

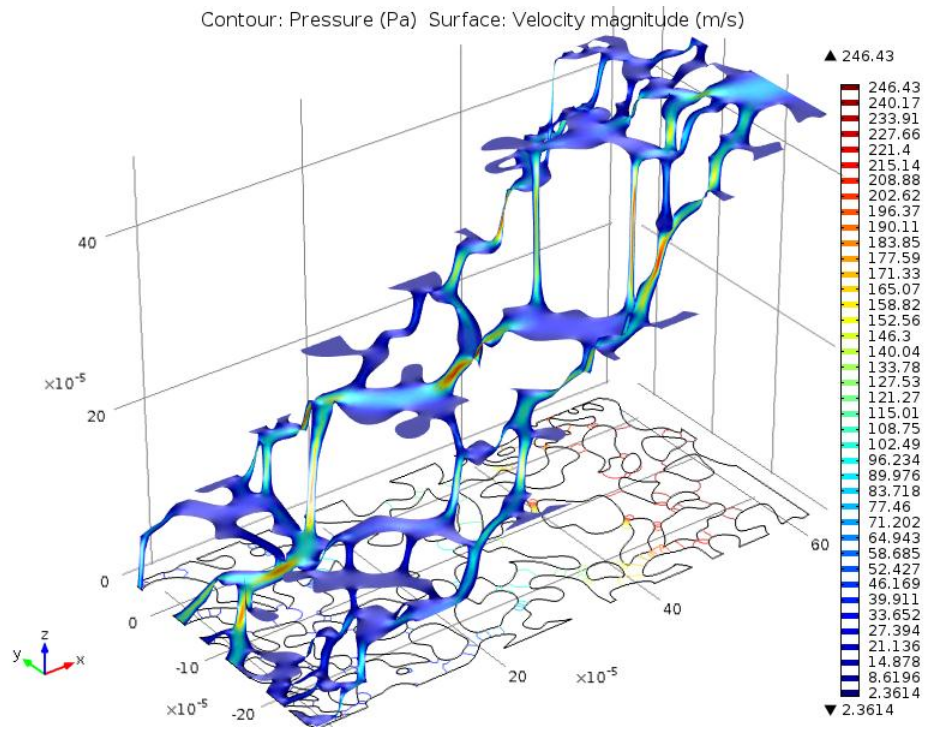

Figure 2.8: Velocity field and pressure surface in two-dimensional pore space for a pressure drop of 250 Pa/640 µm.

2.4.2 Model Structure & Summary of Particle Tracking Simulations

The momentum balance described in the following equation was used to model particle movement in the flow field:

$$\frac{\delta(m_p v)}{\delta t} = F_t \tag{2.4}$$

where m_p is the particle mass, v is the particle velocity vector, and F_t is the vector sum of all forces acting on the particle at any given time. The forces modeled were fluid drag, gravity, and electric surface charge interactions (the last of which is a work in progress).

The fluid drag force on a particle F_d was calculated using the following equation:

$$F_d = m_p \frac{18\mu}{\rho_p d_p^2}(u - v) \tag{2.5}$$

where μ is fluid viscosity (1 cP), u is the fluid velocity vector, ρ_p is the density of a particle, and d_p is particle diameter.

The gravitational force on a particle F_g was calculated using the following equation:

$$F_g = m_p g \frac{(\rho_p - \rho_f)}{\rho_p} \tag{2.6}$$

where g is gravitational acceleration and ρ_f is fluid density (1000 kg/m^3).

The electrical force on a particle F_e was modeled as:

$$F_e = eZ(\nabla V) \tag{2.7}$$

where e is the elementary charge of an electron, Z is the charge number of each particle (so particle charge is eZ), and ∇V is the electric field intensity in the pore space (V is the electric potential in the pore space). Steady state electric potential fields in the pore space were generated for these simulations by solving the following equation (conservation of electric current):

$$\nabla J = Q_j \tag{2.8}$$

$$\nabla J = \sigma E + J_e \quad \text{(a form of Ohm's Law)} \tag{2.9}$$

$$E = -\nabla V \tag{2.10}$$

$$-n * J = 0 \qquad \text{(electric insulation boundary condition)} \tag{2.11}$$

where J is charge density, Q_j represents an external current source (0 in this case), σ is electrical conductivity of the pore fluid (3e-4 S/m), E is the electric field, J_e is externally generated current density (0 in this case), and n is the unit normal vector at a model boundary. The following boundary condition was used to apply an electric potential at the rock surface: $V = V_0$ where V_0 is some constant electric potential at the pore wall.

The particle tracing simulations performed are summarized in Table 2.2.

Table 2.2: Summary of Particle Tracing Simulations Performed

Case	*Drag*	*Gravity*	*Electric*	*Δp [Pa]*	*ρ_p [kg/m3]*	*d_p [m]*	*Injection*	*Wall potential (V)*	*Z (particle charge #)*
1	*y*	*n*	*n*	*0.715*	*2200*	*500*	*Pulse*	*n/a*	*n/a*
2	*y*	*n*	*n*	*248*	*2200*	*500*	*Pulse*	*n/a*	*n/a*
3	*y*	*n*	*n*	*0.715*	*2200*	*500*	*Step*	*n/a*	*n/a*
4	*y*	*n*	*n*	*248*	*2200*	*500*	*Step*	*n/a*	*n/a*
5	*y*	*y*	*n*	*0.715*	*2200*	*500*	*Pulse*	*n/a*	*n/a*
6	*y*	*y*	*n*	*248*	*2200*	*500*	*Pulse*	*n/a*	*n/a*
7	*y*	*y*	*n*	*0.715*	*2200*	*2000*	*Pulse*	*n/a*	*n/a*
8	*y*	*y*	*n*	*248*	*2200*	*2000*	*Pulse*	*n/a*	*n/a*
9	*y*	*y*	*n*	*0.715*	*8000*	*500*	*Pulse*	*n/a*	*n/a*
10	*y*	*y*	*n*	*248*	*8000*	*500*	*Pulse*	*n/a*	*n/a*
11	*y*	*y*	*n*	*0.715*	*8000*	*100*	*Pulse*	*n/a*	*n/a*
12	*y*	*y*	*n*	*248*	*8000*	*100*	*Pulse*	*n/a*	*n/a*
13	*y*	*n*	*y*	*0.715*	*2200*	*500*	*1 particle*	*-0.05 mV*	*-100*
14	*y*	*n*	*y*	*0.715*	*2200*	*500*	*1 particle*	*-0.05 mV*	*+100*
15	*y*	*n*	*y*	*0.715*	*2200*	*500*	*Pulse*	*-0.05 mV*	*-50*
16	*y*	*n*	*y*	*0.715*	*2200*	*500*	*Pulse*	*-0.05 mV*	*+20*
17	*y*	*n*	*y*	*0.715*	*2200*	*500*	*Pulse*	*-5 V*	*-50*

2.5 RESULTS

2.5.1 Fracture-Flow Experiments

The transport of silica particles was investigated by flow experiments in a fractured Berea sandstone core plug. For this purpose, the particle suspension concentration, particle size and fluid velocity were varied. The effluent breakthrough curves are presented in Figure 2.9.

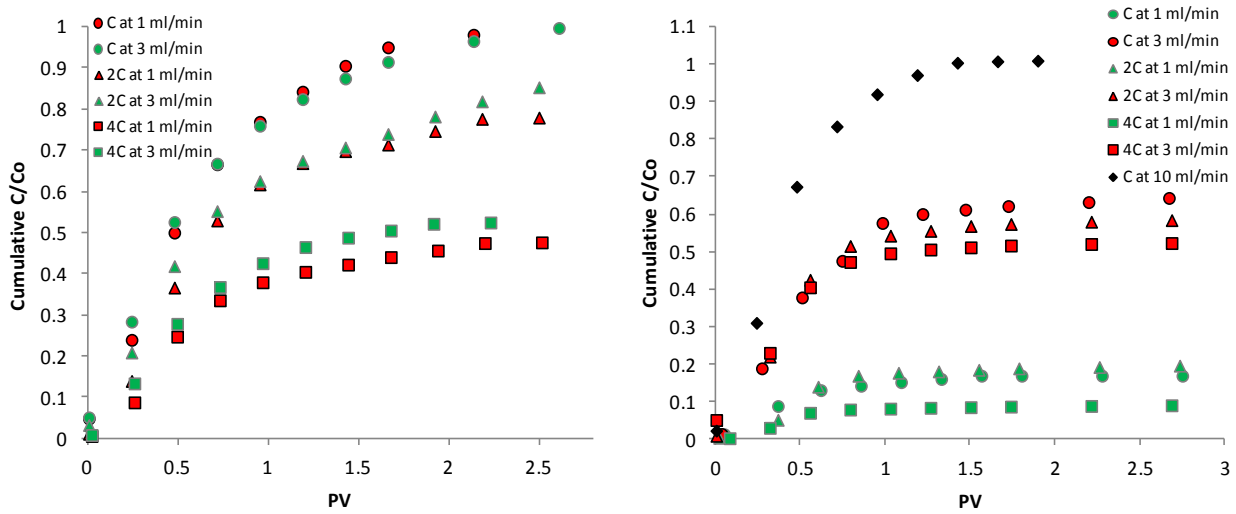

Figure 2.9: Breakthrough curves for silica microspheres with diameter of 2 µm (left) and 5 µm (right), at different flow rates and particle suspension concentration. Recovery of particles is enhanced as particle size increase, which is indicative of straining.

Several observations can be made based on these breakthrough curves. The breakthrough time for both particle sizes was very similar. The return curves for both particle sizes showed a very fast arrival followed by gradually increasing (in the case of the 2 µm particles) or constant (for the 5 µm particles) concentrations. The first arrival of the 2 and 5 µm particles occurred within 0.02 to 0.04 and 0.03 to 0.08 pore volume of the start of their injection. This suggests that the recovered particles were, at least initially, moving through the fracture and large pores. Trapped particles were most likely retained in the small pore spaces in core matrix and fracture walls in regions with small apertures. It was concluded that gravitational sedimentation, aggregation at the primary energy minimum (only for the 2 µm particles) and straining due to particle size were the main particle trapping mechanisms. For the 5 µm particles, the role of the balance between fluid drag and gravitational forces was apparent. The particle cumulative recovery decreases with increasing particle size at the same experimental conditions, which is indicative of straining. This finding is consistent with the observation made by Bradford et al. (2002) through the injection of fluorescent latex particles into saturated sand columns.

For the 2 µm silica particles (Figure 2.9, left), the recovery was inversely proportional to particle suspension concentration, and directly proportional to fluid velocity. Recovery was strongly sensitive to concentration, and slightly sensitive to fluid velocity. Detachment of

particles by rolling, sliding or lifting was considered insignificant since increasing fluid velocity (drag forces) did not result in considerable recovery enhancement.

Similarly, with increasing particle size (5 µm), the recovery was also increasing with increasing fluid velocity and decreasing with increasing concentration. The degree by which the recovery was influenced by these parameters (fluid velocity and suspension concentration) was completely different at this particle size. It was observed that recovery is more sensitive to fluid velocity than concentration. In general, the particle recovery (Figure 2.9, right) was found to have a linear relationship with the fluid velocity used during injection. For example, the recovery of the 5 µm diameter particle particles had increased from below 20% to higher than 64% (about three times higher by increasing fluid velocity by factor of three). Further increase in fluid velocity resulted in complete recovery of the 5 µm diameter silica particles (Figure 2.9, right). Large particles follow fast moving streamlines (central streamlines) and therefore they are held away from grain or fracture walls. As fluid velocity decreases, the drag force exerted on particles by moving fluid also decreases, allowing gravity to play a larger role. Particles may also diffuse away from fast moving streamlines toward the fracture walls, or near grains at the fracture-matrix interface, but this is not expected to play a dominant role in the transport of micron-scale particles. Based on all experimental data, it was hypothesized that the gravitational sedimentation was playing an important role in the particle transport.

The silica particles used in these experiments have a density of about 2.2 g/cm^3, more than twice that of suspension or injected water, meaning that these particles are subject to a force due to gravity. The gravitational force on a particle is directly proportional to particle mass (and thus the cube of the particle diameter), so the 5 µm particles are more greatly affected by gravitational settling than the 2 µm particles (see Equation 2.6). This helps to explain why the recovery of 5 µm particles is much more sensitive to fluid velocity than the 2 µm particles. As the trapping of 5 µm particles is likely dominated by gravitational sedimentation (which can be directly offset by increasing fluid velocity) and the trapping of the 2 µm particles is likely dominated by aggregation (which cannot necessarily be directly offset by increasing fluid velocity), it makes sense that the recovery of the 5 µm particles is more sensitive to fluid velocity than that of the 2 µm particles.

Furthermore, the fluid drag force acting on spherical particle is directly proportional to the fluid velocity and the particle diameter (see Equation 2.5). Larger particles will be under greater drag forces, and thus, they will be mobilized or detached more effectively from contact surface as velocity increases (Ryan and Elimelech, 1995). The lift force that also counters the adhesive force is also function of the fluid velocity (see Figure 2.10). The combined effect of fluid velocity and those forces renders larger particles to be very sensitive to fluid velocity. Finally, as a result of increasing fluid velocity, the volume of low velocity regions (referred to as stagnant flow regions) will decrease, which will limit collision of particles between fracture surface crevasses or at the pore walls.

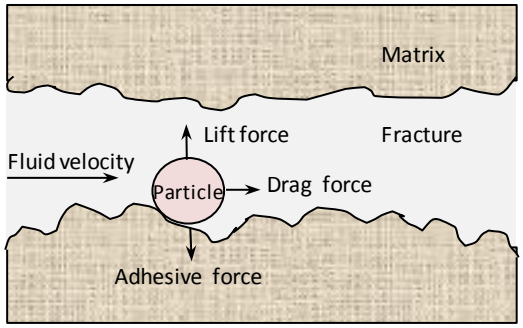

Figure 2.10: Illustration of acting forces on particle attached to rough surface.

2.5.2 Particle Tracking Simulations

The return curves for the simulations are shown in Figure 2.11.

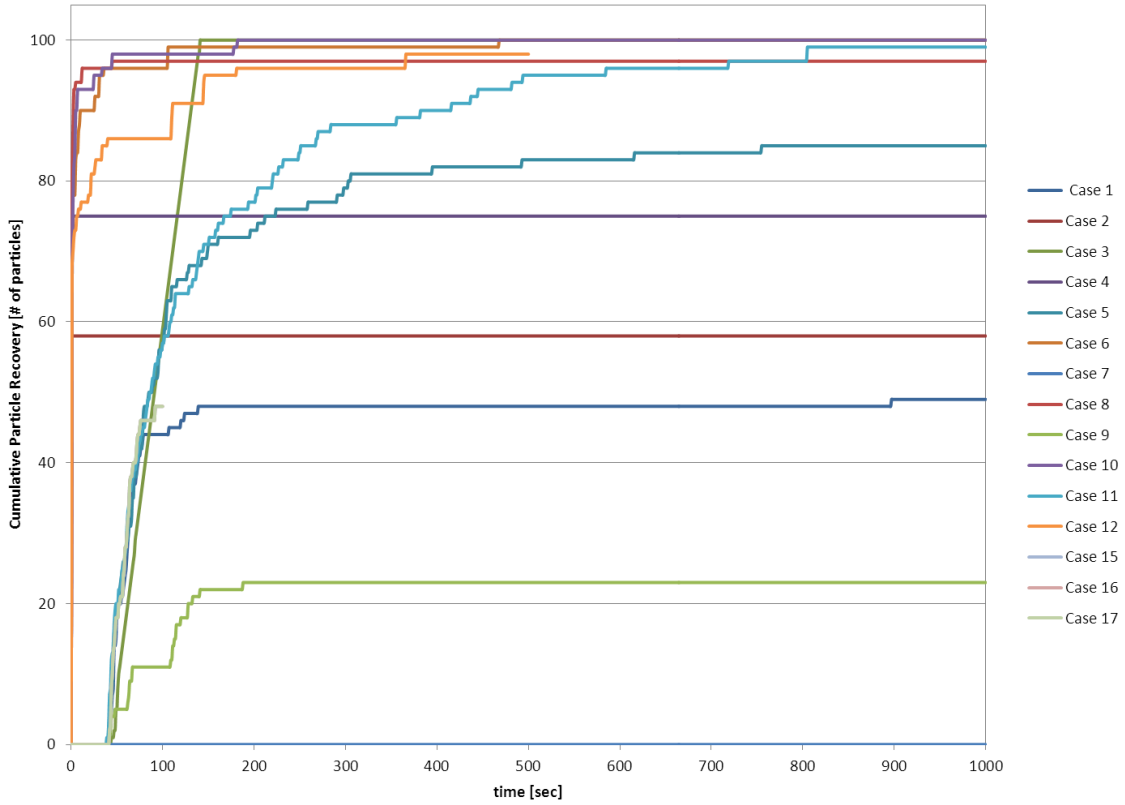

Figure 2.11: Particle return curves

Note that return curves for Cases 13 and 14 are not included, because the only particle simulated in these cases was trapped on a rock grain (see Figure 2.14). Counting the number of particles that reach the outlet gives a more quantitative measure of particle recovery. However, the size of the model raises the question of how these results can be

scaled up to predict recovery in an entire micromodel, a coreflood, and ultimately a reservoir.

The particle trajectory plots for selected cases are given in Figures 2.12 and 2.13.

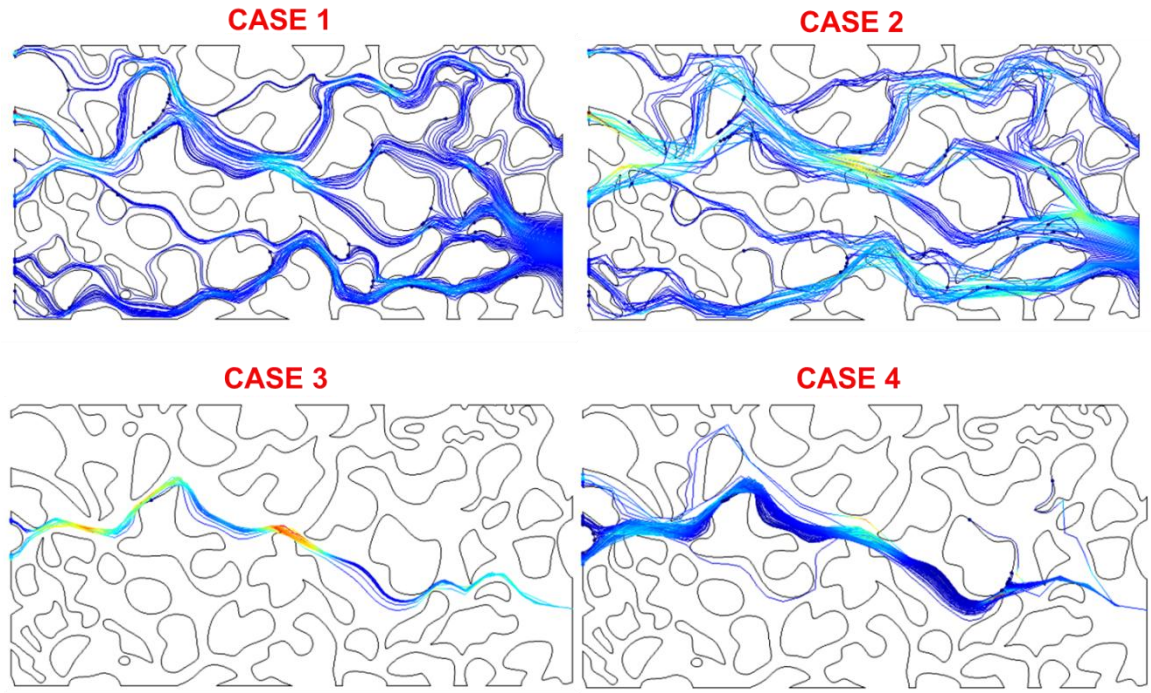

Figure 2.12: Particle trajectories for Cases 1-4 at t=1000 s.

Note in Figure 2.12 that the color of the particle trajectories represents particle velocity. Also note that the trajectories for the high velocity cases (Cases 2 and 4) are less smooth and sometimes seem to pass through the rock grains. This is an artifact of storing the calculated particle position at too few time steps and does not actually represent the simulation results. It is obviously more noticeable in the high velocity cases because the particles are moving more quickly.

In all four cases, some particles are trapped mechanically against rock grains by advective forces (no consideration of gravity, charge interactions, or chemical bonding). This is called interception. In the "step" injection simulations, fewer particles experience interception because all particles enter the model in a high velocity region. Thus, they are more likely to stay in the high velocity regions of the pore space and less likely to collide with rock grains and become mechanically trapped. For this reason, it is important to understand the nature of particles entering fluid streamlines from an injection port, which could be the subject of future modeling.

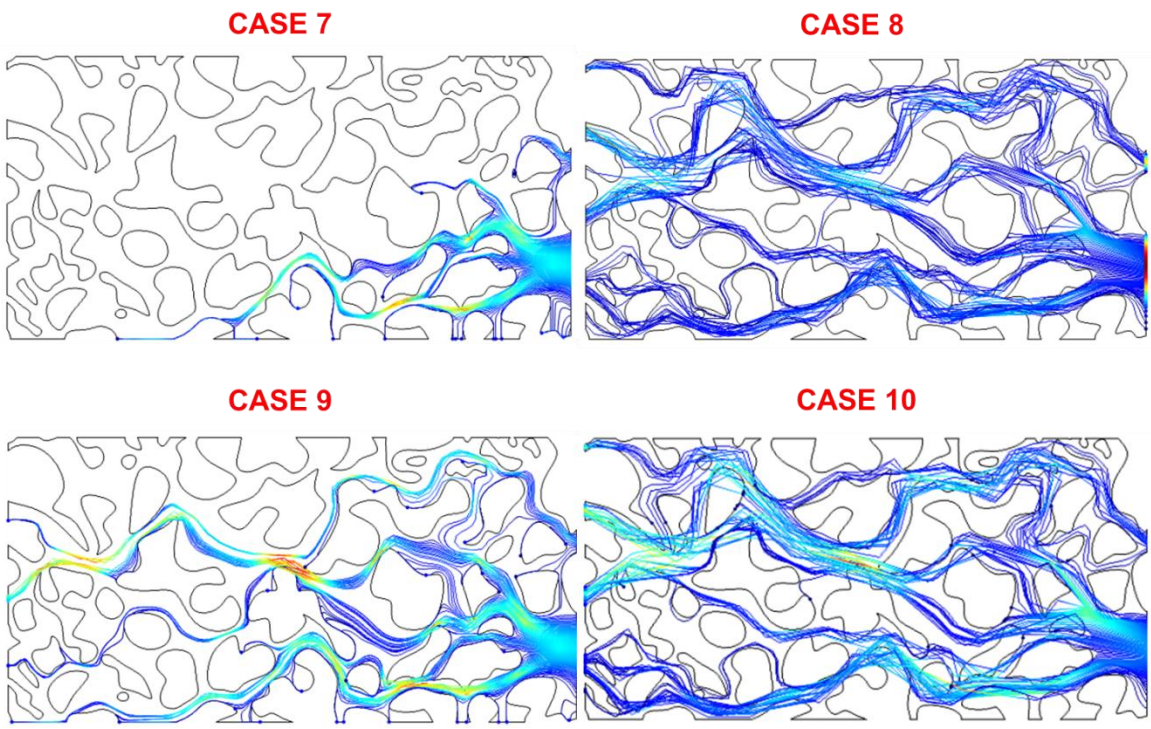

Figure 2.13: Particle trajectories for Cases 7-10 at t=1000 s

It is apparent that for sufficiently large or dense particles, gravitational settling can severely limit particle transport. However, increasing the pressure (and thus fluid velocity) mitigates this somewhat, which is in agreement with the observations in section 2.5.1. Also, in the case of 100 nm particles with a density of 8000 kg/m^3, which was meant to approximate the density of tin-bismuth (trajectory plot not shown), gravity has much less of an effect than for these larger particles.

The electric potential fields in the pore space for different simulation cases are shown in Figure 2.14, and the particle trajectory plots for the cases accounting for particle interactions with these potential fields are shown in Figure 2.15.

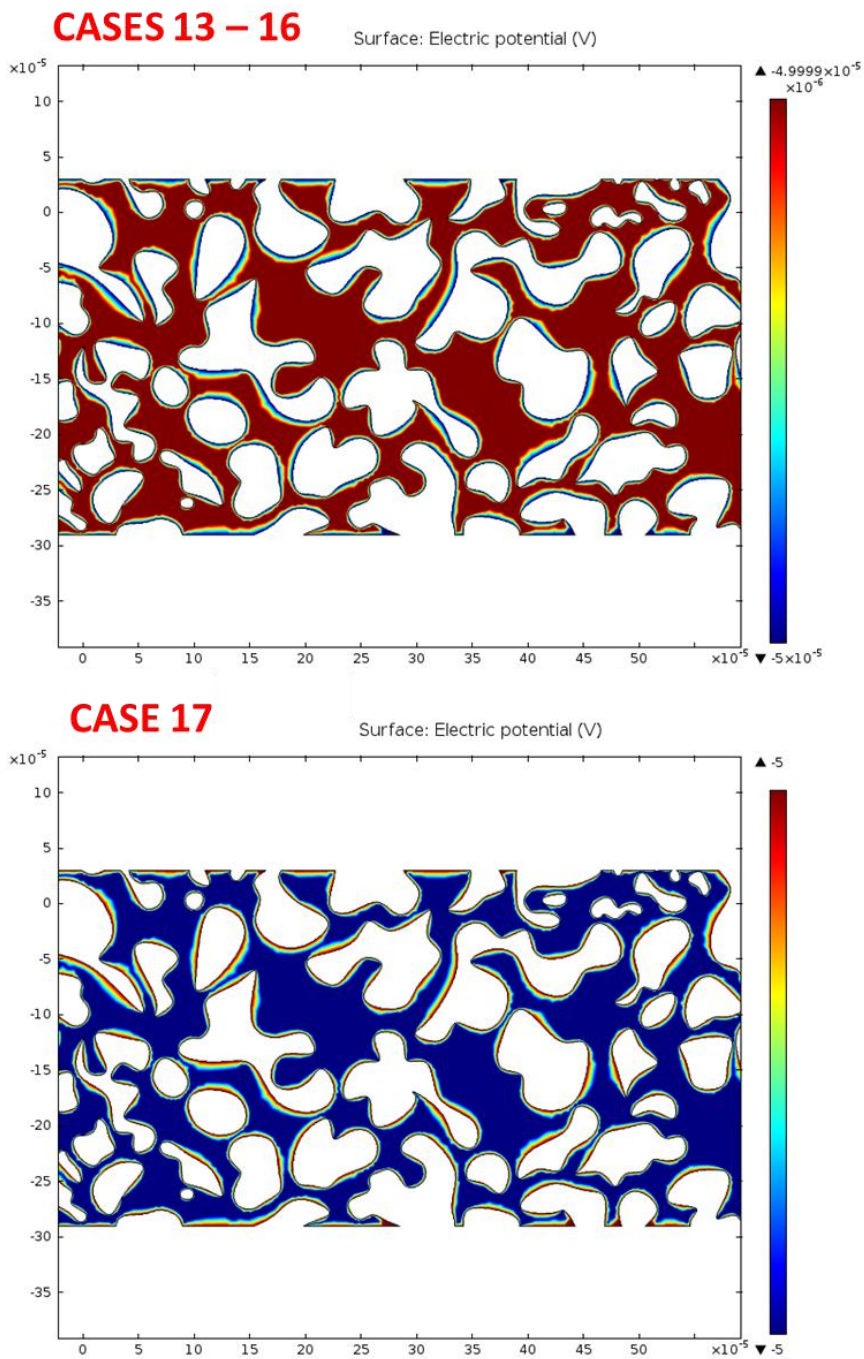

Figure 2.14: Distribution of electric potential in pore space for different cases

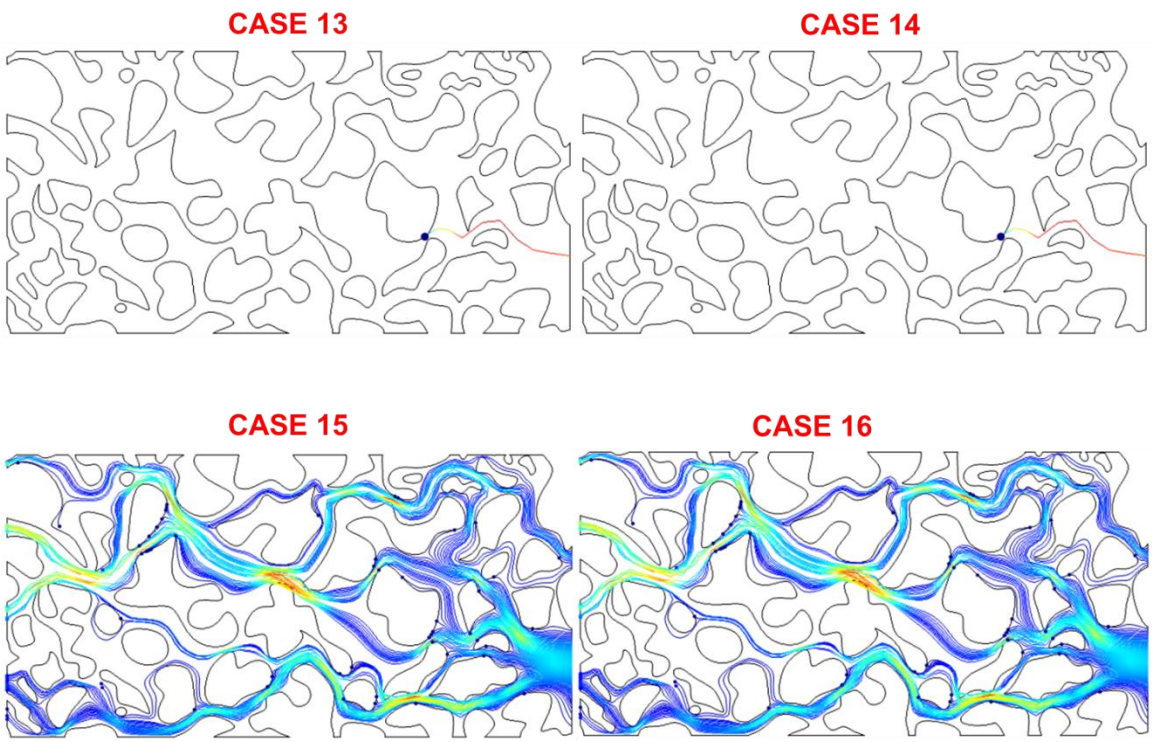

Figure 2.15: Particle trajectories for Cases 13-16 at t=1000 s

It can be seen in Figure 2.15 that the changes made to both the electric potential at the rock surface and the particle charge had very little effect on particle trajectories. Moreover, the recovery was very similar to the simulation without electric interactions up to t=100 s (see Figure 2.11). While this may be plausible, it should be noted that the boundary values used for electric potential were somewhat arbitrary, and careful selection of these values will increase the validity of these results. Another possible cause for the minimal impact of the electric potential field is that the discretization close to the pore walls may not be small enough, thus preventing particles from traveling closer to the wall where the electric force is largest.

2.5 FUTURE WORK

A detailed analysis of the results of the flow experiments in fractured sandstone will be performed. This analysis will make use of classical particle filtration theory and Derjaguin-Landau-Verwey-Overbeek (DLVO) Theory to quantify the forces affecting particle transport at various experimental conditions.

On the modeling side of the project, future efforts will be made to obtain more realistic values of both particle charge and electric potential at rock surfaces. The impact of using a smaller discretization close to the pore walls will be investigated to see if this results in a more significant electric force. A model with geometry corresponding to that of the micromodel experiments will be generated for experimental comparison. Ultimately, chemical forces, particle aggregation, and size exclusion will be incorporated into the

modeling to provide a comprehensive view of what governs particle transport under various conditions.

3. FRACTURE CHARACTERIZATION USING RESISTIVITY

This research project is being conducted by Research Assistant Lilja Magnusdottir, Senior Research Engineer Kewen Li and Professor Roland Horne. The objective of this project is to investigate ways to use resistivity to infer fracture properties in geothermal reservoirs.

3.1 SUMMARY

In this project, the aim is to use Electrical Resistivity Tomography (ERT) to characterize fracture properties in geothermal fields. The resistivity distribution of a field can be estimated by measuring potential differences between various points while injecting an electric current into the ground and resistivity data can be used to infer fracture properties due to the large contrast in resistivity between water and rock. The contrast between rock and fractures can be increased further by injecting a conductive tracer into the reservoir, thereby decreasing the resistivity of the fractures. In this project, the potential difference has been calculated between two points (an injector and a producer) as conductive fluid flows through a fracture network. The time history of the potential field depends on the fracture network and can therefore be used to estimate where fractures are located and the character of their distribution.

The flow simulator TOUGH2 was used to calculate how a conductive tracer distributes through geothermal reservoirs and the analogy between Ohm's law that describes electrical flow and Darcy's law describing fluid flow made it possible to use TOUGH2 also to calculate the electric fields. The EOS1 module was used in both cases and it was found to be capable of calculating the electric potential for a simple grid accurately enough despite assuming that liquid viscosity, density and compressibility are pressure-dependent. A discrete-fracture model introduced by Karimi-Fard et al. (2003) was used to create a discrete-fracture network with fractures of realistic dimensions and the time history of the potential difference between an injector and a producer was analyzed. The study demonstrated how the electric potential difference between two wells, and its derivative, could provide information about the fracture paths from the injector to the producer. Next, the fracture network was modeled as an electric circuit to verify that the electric field calculations from TOUGH2 were accurate for the discrete fracture network. Finally, some preliminary work was done in finding ways to use the electric potential with inverse modeling to characterize fracture patterns.

Future work includes investigating further how inverse modeling can be used to find the character and distribution of fractures in the reservoirs. It is also of interest to implement self-potential calculations into the model since the change in self-potential affects the measured potential difference and could facilitate fracture characterization. Due to the limited number of measurement points, the study will include investigating ways to enhance the process of characterizing fractures from sparse resistivity data. One of future goals is to study the influence of injecting varying tracer concentrations and also to examine different electrode layouts.

3.2 INTRODUCTION

Characterizing the dimensions and topology of fractures in geothermal reservoirs is crucial for optimal design of production. Fractures carry most of the fluid in the reservoir so fracture configuration is central to the performance of a geothermal system both in fractured reservoirs as well as in Enhanced Geothermal System (EGS) applications. The knowledge of fluid-flow patterns is necessary to ensure adequate supply of geothermal fluids and efficient operation of geothermal wells and to prevent short-circuiting flow paths from injector to producer that would lead to premature thermal breakthrough. Fracture characterization therefore increases the reliability of geothermal wells and the overall productivity of geothermal power plants.

The goal of this study is to find ways to use Electrical Resistivity Tomography (ERT) to characterize fractures in geothermal reservoirs. ERT is a technique for imaging the resistivity of a subsurface from electrical measurements. Pritchett (2004) concluded based on a theoretical study that hidden geothermal resources can be explored by electrical resistivity surveys because geothermal reservoirs are usually characterized by substantially reduced electrical resistivity relative to their surroundings. Electrical current moving through the reservoir passes mainly through fluid-filled fractures and pore spaces because the rock itself is normally a good insulator. In these surveys, a direct current is sent into the ground through electrodes and the voltage differences between them are recorded. The input current and measured voltage difference give information about the subsurface resistivity, which can then be used to infer fracture locations.

Resistivity measurements have been used in the medical industry to image the internal conductivity of the human body, for example to monitor epilepsy, strokes and lung functions as discussed by Holder (2004). In Iceland, ERT methods have been used to map geothermal reservoirs. Arnarson (2001) describes how different resistivity measurements have been used effectively to locate high temperature fields by using electrodes located on the ground's surface. Stacey et al. (2006) investigated the feasibility of using resistivity to measure saturation in a rock core. A direct current pulse was applied through electrodes attached in rings around a sandstone core and it resulted in data that could be used to infer the resistivity distribution and thereby the saturation distribution in the core. It was also concluded by Wang and Horne (2000) that resistivity data have high resolution power in the depth direction and are capable of sensing the areal heterogeneity.

Slater et al. (2000) have shown a possible way of using ERT with a tracer injection by observing tracer migration through a sand/clay sequence in an experimental $10 \times 10 \times 3$ m^3 tank with cross-borehole electrical imaging. Singha and Gorelick (2005) also used cross-well electrical imaging to monitor migration of a saline tracer in a $10 \times 14 \times 35$ m^3 tank. In previous work, usually many electrodes were used to obtain the resistivity distribution for the whole field at each time step. The resistivity distribution was then compared to the background distribution (without any tracer) to see resistivity changes in each block visually. These resistivity changes helped locate the saline tracer and thereby the fractures. Using this method for a whole reservoir would require a gigantic parameter space, and the inverse problem would not likely be solvable, except at very low resolution. However, in

the approach considered in this study, the electrodes would be placed inside two or more geothermal wells and the potential differences between them studied. The potential difference between the wells which corresponds to changes in resistivity would be measured and plotted as a function of time while the conductive tracer flows through the fracture network. The goal of this project is to find ways to use that response, i.e. potential difference vs. time, in an inverse modeling process to characterize fracture patterns.

In this report, the analogy between water flow and electrical flow is defined and the possibility of using EOS1 module in TOUGH2 instead of EOS9 is explored. Next, the resistivity of a saline tracer is interpreted and the time history of the electric potential difference is studied for a discrete-fracture network to illustrate further how the potential difference response corresponds to the fracture network. The discrete fracture network is also modeled as an electric circuit and the analytical results compared to results from TOUGH2. Finally, some preliminary work to find ways to use inverse analysis to characterize fracture networks is described and future work outlined.

3.3 WATER FLOW ANALOGY OF ELECTRICAL FLOW

The steady-state flow of an electric current through a conducting medium due to differences in energy potential is analogous to the steady-state flow of a fluid through porous medium. Darcy's law is an empirical relationship similar to Ohm's law,

$$J = -\sigma \nabla \varphi \tag{3.1}$$

where J is current density [A/m^2], σ is the conductivity of the medium [Ωm] and φ is the electric potential [V] but instead of describing electrical flow Darcy's law describes fluid flow through a porous medium,

$$q = -\frac{k}{\mu} \nabla p \tag{3.2}$$

where q is the flow rate [m/s], k is permeability [m^2], μ is viscosity of the fluid [kg/ms] and p is pressure [Pa]. Table 3.1 presents the correspondence between the variables and relations of water flow (Darcy's law) and electric current flow (Ohm's law).

Table 3.1: Correspondence between electric current flow and water flow.

	Darcy's law: $q = -\frac{k}{\mu} \nabla p$	Ohm's law: $J = -\sigma \nabla \varphi$
Flux of:	Water q [m/s]	Charge J [A/m^3]
Potential:	Pressure p [Pa]	Voltage φ [V]
Medium property:	Hydraulic conductivity k/μ [m^2/Pa·s]	Electrical conductivity σ [1/Ωm]

The similarities between these two equations imply that it is possible to use flow simulator like TOUGH2 to solve electric field due to flow of electric current. Then, the pressure results from TOUGH2 would correspond to the electric voltage, the current density to the flow of water and the electrical conductivity would correspond to the hydraulic conductivity, i.e.

$$\sigma = \frac{k}{\mu} \tag{3.3}$$

However, it must be recognized that viscosity depends on pressure while conductivity of a reservoir does not depend on the electric voltage used.

3.4 PRESSURE DEPENDENCE OF VISCOSITY

The previous quarterly report (July-September 2011) described how the EOS9 module in TOUGH2 was used successfully to solve the electric field due to flow of an electric current by defining the liquid viscosity, density and compressibility constant. Therefore, unlike EOS1, EOS9 allows for a simulation of an electric field without the resistivity becoming dependent on the electric potential. However, the EOS1 module has been used in this project instead of EOS9 because we some problems occurred when EOS9 was used with the Discrete Fracture Method (DFN) by Karimi-Fard et al. (2003). In order to study the effects of pressure dependence on the simulated electric potential, EOS1 and EOS9 were both used to calculate the electric field for a simple 9 × 9 grid shown in Figure 3.1.

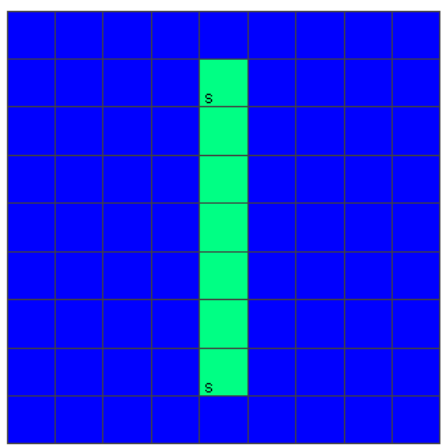

Figure 3.1: Inhomogeneous 9 × 9 grid.

The two-dimensional grid was modeled with dimensions 100 × 100 × 1 m^3 and permeability 1×10^{-13} m^2 (blue blocks) and with a fracture in the middle with permeability 1×10^{-8} m^2 (green blocks). The initial pressure was set as 10^6 Pa and the temperature as 150°C. Equation 3.3 shows how the conductivity of the field was defined as the permeability divided by the viscosity, so when EOS1 was used the conductivity changed by a small amount as the viscosity changed with pressure. In EOS9 the viscosity, density and compressibility were defined constant making it possible to model constant

conductivity values for the reservoir. Figure 3.2 shows the electric potential for the grid blocks calculated using EOS1 and EOS9 in TOUGH2.

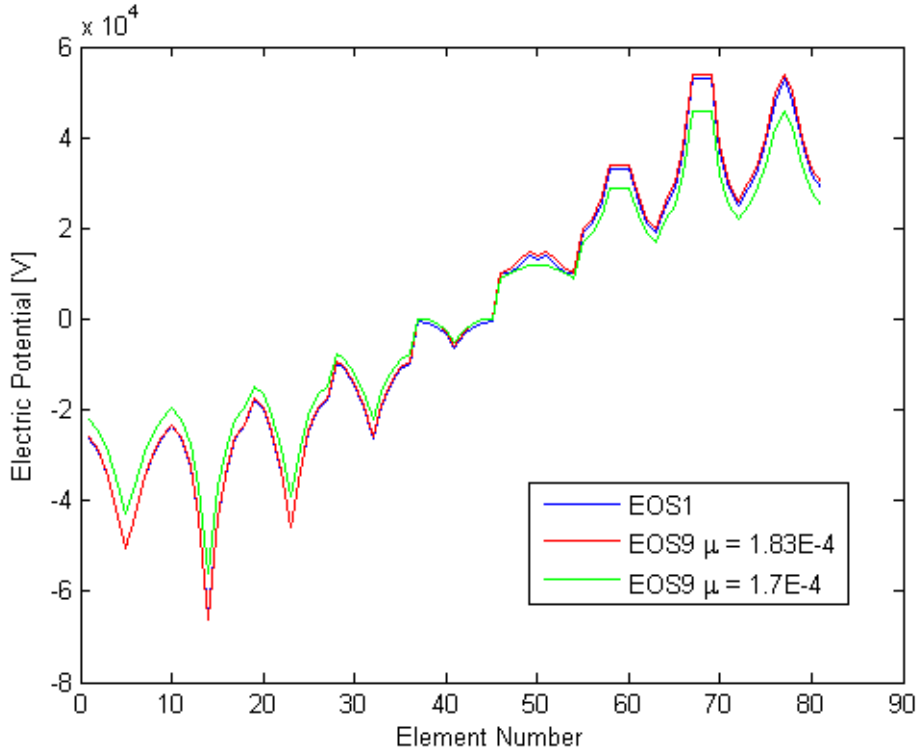

Figure 3.2: Electric potential for the reservoir calculated using EOS1 and EOS9

The electric potential calculated using EOS1 is almost the same as the electric potential calculated using EOS9 with $\mu = 1.84 \times 10^{-4}$ Pa·s. However, if the viscosity is set as 1.7×10^{-4} Pa·s the electric potential results are slightly different from the EOS1 results because EOS1 uses the viscosity of water at the appropriate pressure and temperature conditions. In this case, the pressure is ranging from $0.996\text{-}1.0 \times 10^{6}$ Pa and the temperature is 150°C so the viscosity is ranging from $1.85\text{-}1.83 \times 10^{-4}$ Pa·s. Therefore, it has been shown that EOS1 module in TOUGH2 can be used to calculate the electric field instead of using EOS9 as long as the permeability is defined as the conductivity multiplied with the appropriate viscosity that corresponds to the pressure and temperature conditions in the simulation.

3.5 RESISTIVITY OF A SALINE TRACER SOLUTION

The tracer injected into the reservoirs is a NaCl solution whose resistivity changes with temperature and concentration. Ucok et al. (1980) have established experimentally the resistivity of saline fluids over the temperature range 20-350°C and their results for resistivity of NaCl solution calculated using a three-dimensional regression formula is shown in Figure 3.3.

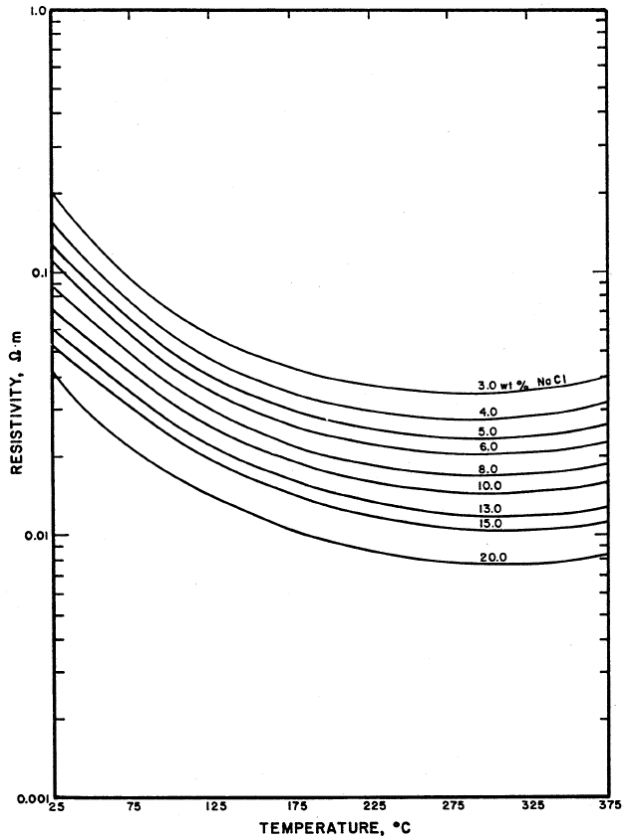

Figure 3.3: Resistivity of a NaCl solution as a function of temperature and concentration (Ucok et al., 1980).

Ucok et al. (1980) calculated that the dependence of resistivity is best represented by the formula:

$$\rho_w = b_0 + b_1 T^{-1} + b_2 T + b_3 T^2 + b_4 T^3 \tag{3.4}$$

where T is temperature and b are coefficients found empirically. The best fit for the concentration dependence was found to be:

$$\rho_w = 10/(\Lambda c) \tag{3.5}$$

Where:

$$\Lambda = B_0 - B_1 c^{1/2} + B_2 c \ln c + higher\ order\ terms \tag{3.6}$$

Coefficients B depend on the solution chemistry and c is the molar concentration.

In this project, the tracer concentration resulting from the flow simulation is changed into molar concentration and the following B coefficient matrix for the three-dimensional

regression analysis of the data studied by Ucok et al. (1980) is used to calculate the resistivity of the NaCl solution,

$$B = \begin{matrix} 3.470 & -6.650 & 2.633 \\ -59.23 & 198.1 & -64.80 \\ 0.4551 & -0.2058 & 0.005799 \\ -0.346E\text{-}5 & 7.368E\text{-}5 & 6.741E\text{-}5 \\ -1.766E\text{-}6 & 8.787E\text{-}7 & -2.136E\text{-}7 \end{matrix}$$

Then, the resistivity of water saturated rock, ρ, is calculated using Archie's law,

$$\rho = a\phi^{-b}\rho_w \tag{3.7}$$

where ϕ is the porosity of the rock and a and b are empirical constants, here a is set as 1 and b as 2. The resistivity value of each block therefore depends on the tracer concentration in that block and the value decreases as more tracer flows into the block. Before any tracer has been injected into the reservoir the pores and fractures are assumed to be filled with ground-water. Normal ground-waters are commonly near 0.1 molar NaCl solution (Ucok et al., 1980) which corresponds to 5.4206×10^{-3} initial tracer concentration.

3.6 DISCRETE FRACTURE NETWORKS

Discrete Fracture Network (DFN) models represent fracture-dominated flow paths in geothermal reservoirs more accurately since the fractures are treated discretely instead of being defined by high permeability values in course-scale grid blocks. By employing a DFN approach introduced by Karimi-Fard et al. (2003) we were able to generate a fracture network with fracture grid blocks of realistic dimensions. A MATLAB code written by Juliusson and Horne (2009) was used to generate a two-dimensional stochastic fracture network, run flow simulations on the network with TOUGH2, and plot the tracer flow results. EOS1 module in TOUGH2 was used to both solve the tracer flow as well as the electric flow. Figure 3.4 shows the fracture network generated, where the computational grid was formed using the triangular mesh generator Triangle, developed by Shewchuk (1996).

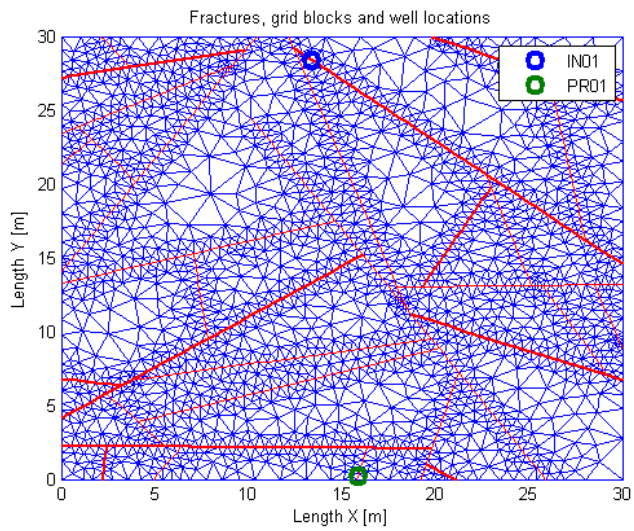

Figure 3.4: Two-dimensional discrete fracture network.

The dimensions of the two-dimensional grid were 30 × 30 m^2 and closed (no-flow) boundary conditions were used. The porosity of the fractures was set to 0.9 and the width, *w*, was assigned as a function of the fracture length *L*,

$$w = L \cdot 10^{-4} \tag{3.8}$$

The corresponding permeability was determined by:

$$k = \frac{w^2}{24} \tag{3.9}$$

The matrix blocks were given a porosity value of 0.1 and a very low permeability value so the conductive fluid only flows through the fractures.

By using the DFN approach every element (both triangles and fracture segments) was given a transmissibility value which is related to the flow between two adjoining elements as,

$$Q_{ij} = T_{ij}(p_j - p_i) \tag{3.10}$$

where *Q* is the flow rate between gridblocks *i* and *j*, *T* is the transmissibility and *p* is the pressure. More details on the approach can be found in the reference by Karimi-Fard et al. (2003).

In Figure 3.5 an injection well can be seen at the top of the figure and a production well at the bottom. Water was injected at the rate of 5.6 × 10^{-2} kg/s with enthalpy 3.14 × 10^5 kJ/kg and the tracer injected was 0.1% of the water injected. The production well was modeled to

deliver against a bottomhole pressure of 10^6 Pa with productivity index of 4×10^{-12} m^3 (as specified for TOUGH2). The initial pressure was set to 10^6 Pa and the temperature to 25°C and the initial tracer mass fraction was set to 5.4206×10^{-3}, which corresponds to groundwater.

Figure 3.5 shows how the tracer concentration in the producer (green) changed with time as more tracer was injected into the reservoir.

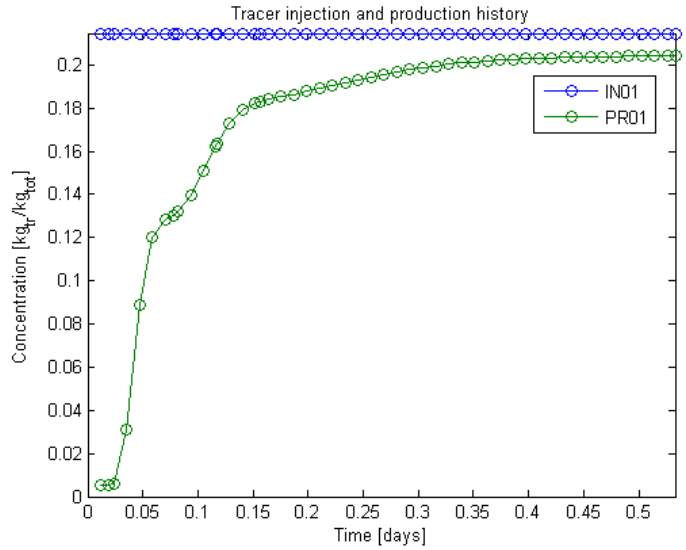

Figure 3.5: Tracer history at the injector (blue) and at the producer (green).

The electrical resistivity method was used to examine how the potential difference history, which corresponds to the changes in resistivity, relates to the fracture network. The current was set as 1 A at the injector and as -1 A at the producer and the potential field calculated using EOS1 module in TOUGH2, see Figure 3.6.

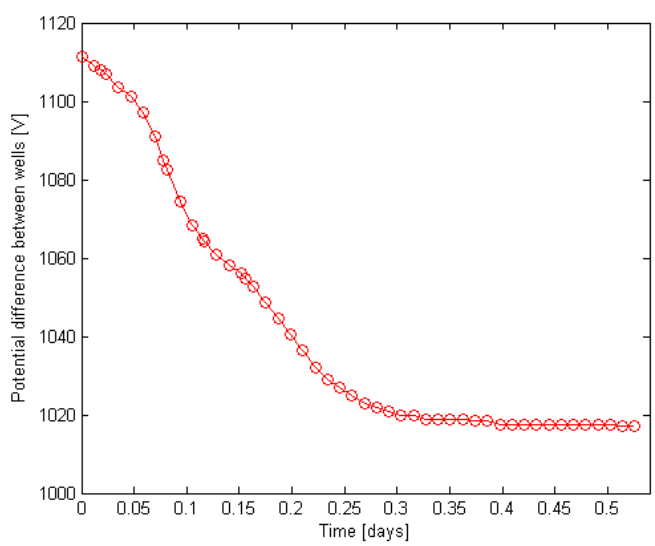

Figure 3.6: Potential difference between the injector and the producer.

The potential difference drops relatively fast until after about 0.25 days where it starts decreasing more slowly. The potential difference depends on the fracture network and can therefore give information about the character of the fractures, as discussed in preceding quarterly report (October-December). Noticing the correspondence between the fractures and the time history of the electric potential can be made easier by looking at the derivative of the potential difference, see Figure 3.7.

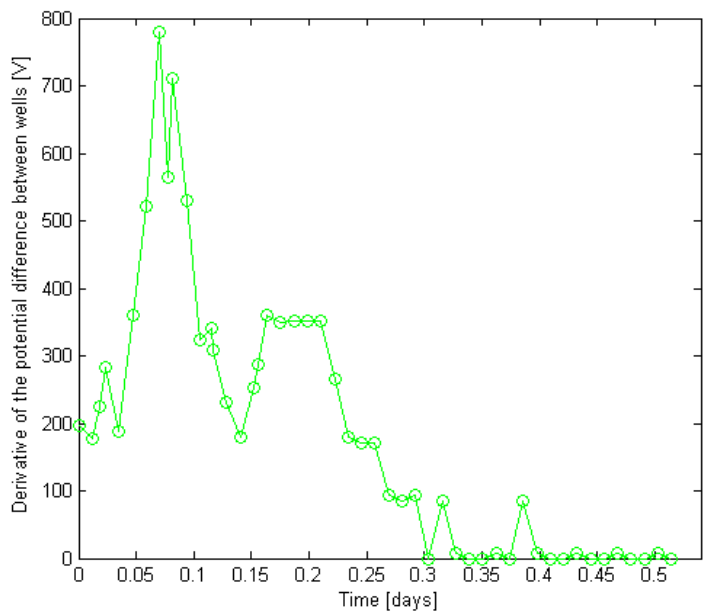

Figure 3.7: Derivative of the potential difference between the wells.

The first peak is after about 0.0351 days when the conductive tracer reaches the production well. The resistivity of the field after 0.023 days and 0.035 days can be seen in Figure 3.8.

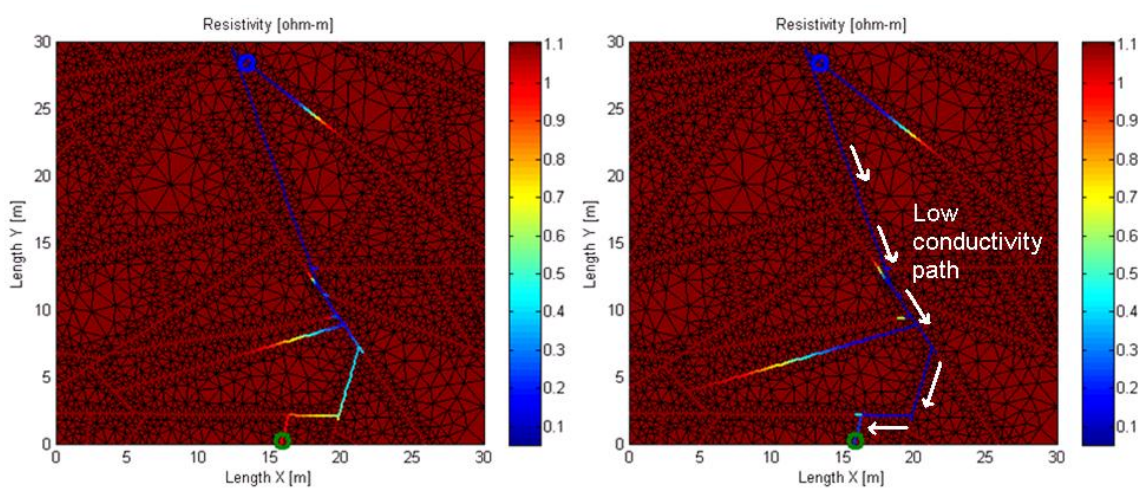

Figure 3.8: Resistivity of the field after 0.023 days (left) and 0.035 days (right).

The tracer concentration at the production well increases from 6.17×10^{-3} at 0.023 days to 3.13×10^{-2} at 0.035 days (see Figure 3.5) causing the resistivity to decrease and a low conductivity path to form between the injector and the producer. The electric current

therefore flows through the low conductivity path, causing the electric potential difference between the wells to drop. Other peaks can be seen in Figure 3.7, for example after about 0.078 days and after about 0.175 days. Figure 3.9 shows the resistivity distribution for these times.

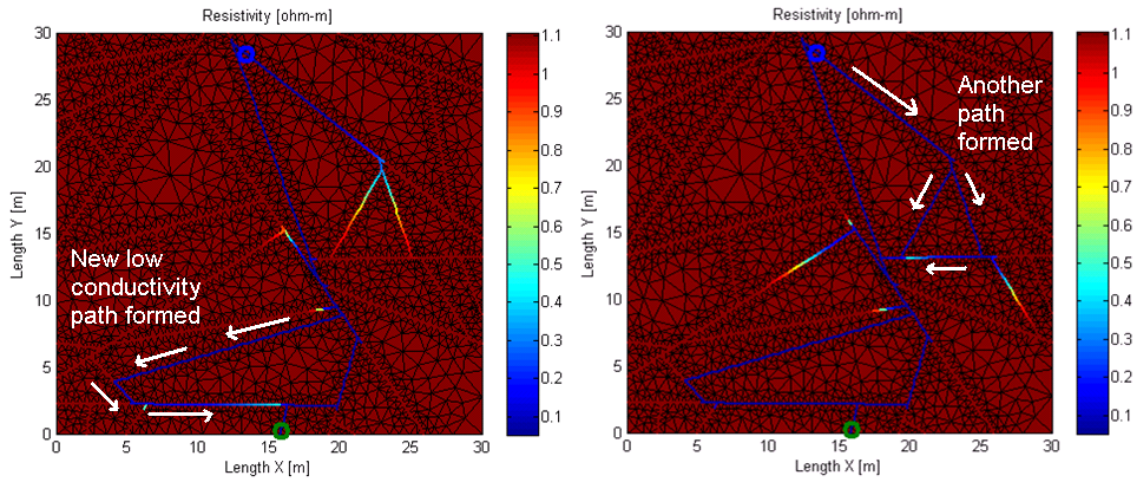

Figure 3.9: Resistivity of the field after 0.078 days (left) and 0.175 days (right).

The peak in Figure 3.7 after 0.078 days corresponds to a new low conductivity path formed to the left of the producer and another path has been formed to the right after 0.175 days. The peaks of the derivative of the potential difference therefore correspond to the fracture network and can be used to infer fracture properties.

3.7 FRACTURE NETWORK ANALYZED AS AN ELECTRIC CIRCUIT

The reservoir in Figure 3.4 acts in many ways like an electric circuit because the fractures form low-resistivity paths from the injector to the producer. The electric current travels mainly through these paths due to the high resistivity of the reservoir. Figure 3.11 demonstrates the electric circuit that corresponds to the fracture network in Figure 3.10 which is the same network previously studied (Figure 3.4) except the width of the fractures was set as 2×10^{-3} m. All the fractures are assumed to be filled with ground-water (with NaCl concentration equal to 5.4206×10^{-3}) and no conductive tracer has been injected into the reservoir.

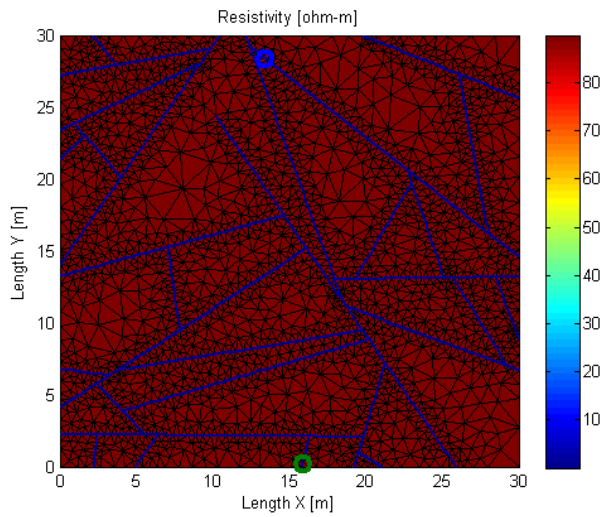

Figure 3.10: A fracture network with water-filled fractures

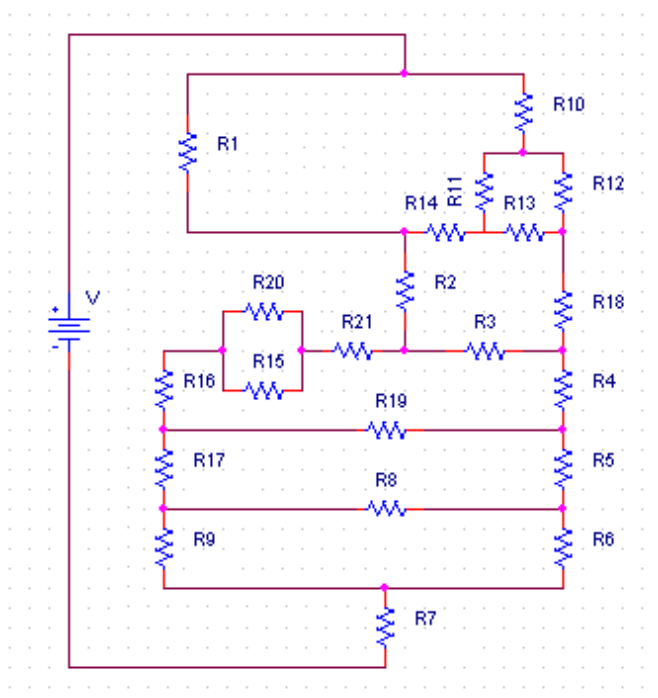

Figure 3.11: Electric circuit that corresponds to the fracture network in Figure 3.10.

The resistance, R [ohm], of the resistors in the electric circuit was calculated using the following relationship,

$$R = \frac{\rho L}{A} \tag{3.11}$$

where L [m] is the length and A [m^2] is the cross sectional area of the corresponding water-filled fracture. Table 3.2 shows the resistivity and dimensions of the fractures in Figure 3.10 as well as the calculated resistance of the resistors in Figure 3.11.

Table 3.2: Fracture properties and calculated resistance of the resistors.

Resistor	Resistance [ohm]	Resistivity [ohm-m]	Length [m]	Area [m^2]
R1	1.02×10^4	1.1086	18.3504	2×10^{-3}
R2	8.61×10^2	1.1086	1.5527	2×10^{-3}
R3	2.61×10^2	1.1086	0.4717	2×10^{-3}
R4	1.10×10^3	1.1086	1.9930	2×10^{-3}
R5	4.06×10^2	1.1086	0.7328	2×10^{-3}
R6	5.99×10^3	1.1086	10.8083	2×10^{-3}
R7	1.08×10^3	1.1086	1.9557	2×10^{-3}
R8	9.34×10^3	1.1086	16.8501	2×10^{-3}
R9	7.19×10^3	1.1086	12.9682	2×10^{-3}
R10	7.23×10^3	1.1086	13.0385	2×10^{-3}
R11	4.26×10^3	1.1086	7.6888	2×10^{-3}
R12	3.88×10^3	1.1086	6.9923	2×10^{-3}
R13	3.23×10^3	1.1086	5.8305	2×10^{-3}
R14	7.32×10^2	1.1086	1.3202	2×10^{-3}
R15	5.57×10^3	1.1086	10.0439	2×10^{-3}
R16	2.61×10^3	1.1086	4.7168	2×10^{-3}
R17	2.45×10^3	1.1086	4.4149	2×10^{-3}
R18	1.05×10^4	1.1086	18.9228	2×10^{-3}
R19	8.88×10^3	1.1086	16.0268	2×10^{-3}
R20	9.11×10^3	1.1086	16.4397	2×10^{-3}
R21	2.40×10^3	1.1086	4.3327	2×10^{-3}

The Y-Δ transformation theory published by Kennelly (1899) was used to simplify the resistors into a single equivalent resistor, $R = 1.2 \times 10^4$ ohm. The electric current at one end of the resistor was set as -1 A and as 1 A at the other end to simulate the current flow through the fractures between the injector and the producer. The voltage drop in the electric circuit was calculated using Ohm's law (Equation 3.1) and compared to the voltage drop for the fracture network computed using module EOS1, see Table 3.3.

Table 3.3: Voltage drop for a fracture network and corresponding electric circuit.

	Voltage drop [V]
Electric circuit	1.1964×10^4
Fracture network	1.1980×10^4

The voltage drop calculated for the electric circuit is equivalent to the voltage drop computed using TOUGH2, so the EOS1 module in TOUGH2 can successfully be used to calculate the electric potential with sufficient accuracy for the procedure in this project. The difference is likely due to the pressure dependency of the viscosity, density and

compressibility in EOS1, as previously analyzed, but should not affect the overall results of the fracture characterization.

3.8 INVERSE ANALYSES

One of the goals of this project is to use the tracer concentration simulations and electrical potential calculations from TOUGH2 with inverse modeling to characterize the dimensions and topology of a fracture network. In inverse modeling the results of actual observations are used to infer the values of the parameters characterizing the system under investigation. In this study, the output parameters would be the tracer return curves at the producer and the potential differences between wells as a function of time while the input parameters would include the dimensions and orientations of the fractures between the wells. The objective function measures the difference between the model calculation (the calculated voltage difference between the wells and tracer return) and the observed data (measured potential field between actual wells and actual tracer return), as illustrated in Figure 3.12, and a minimization algorithm proposes new parameter sets that improve the match iteratively.

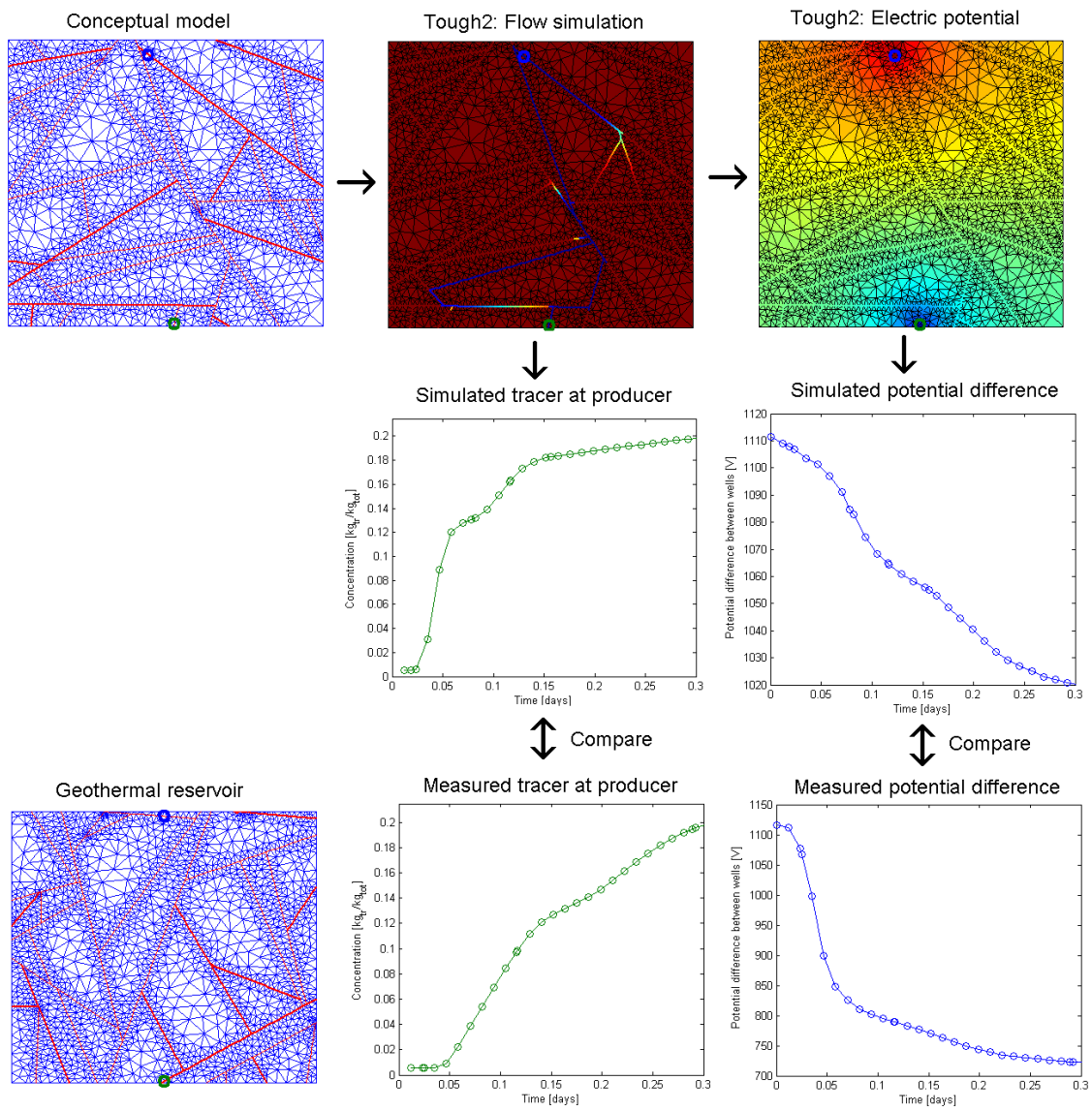

Figure 3.12: The inverse analysis.

Among optimization algorithms in inverse analysis, a Genetic Algorithm (GA) has the advantage that it can search the global minimum value and it can be modified to handle both discrete and continuous variables. The Genetic Algorithm was proposed by Holland (1975) as an optimization method that imitates natural evolution. A solution to the inverse problem is represented as a chromosome and the genetic algorithm creates a population of chromosomes that evolve through mutation and crossover in order to find the best one.

The possibility of using a Genetic Algorithm to characterize fracture patterns was explored by performing a very simple inverse analysis using a Genetic Algorithm to identify a given fracture network from four possible networks. The four networks have dimensions 30 × 30 m^2 and are shown in Figure 3.13.

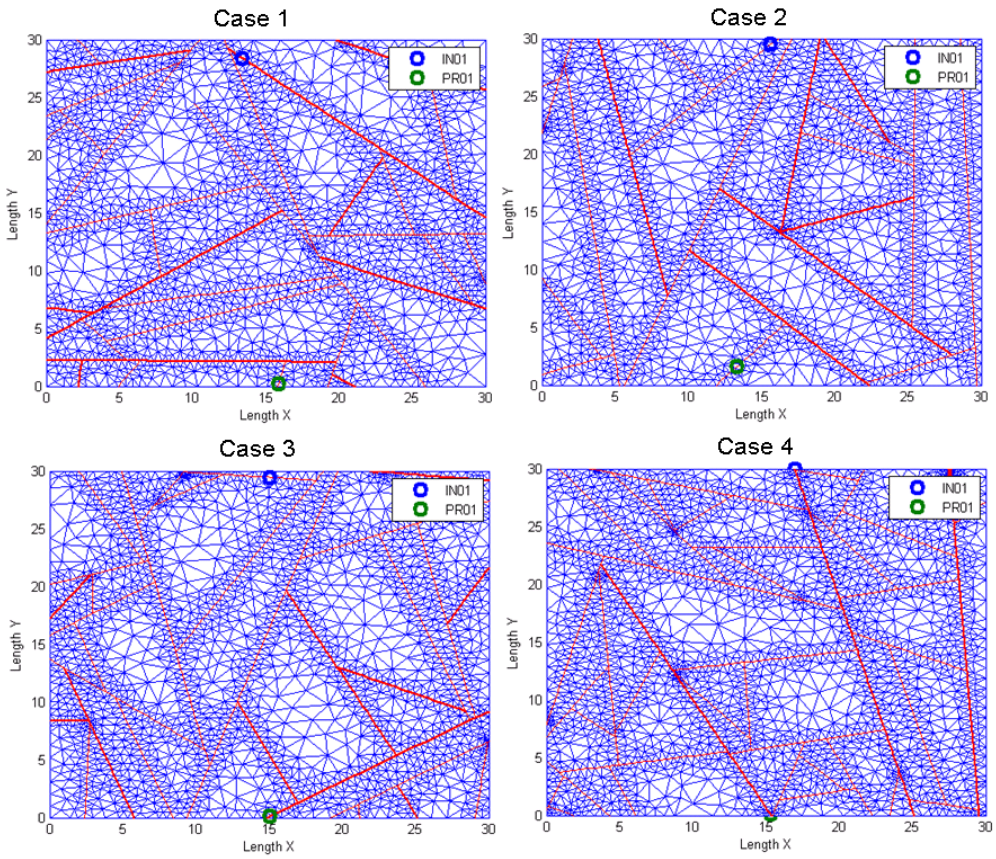

Figure 3.13: Discrete fracture networks.

The reservoir and injection/production properties were the same as for the fracture network decribed previously (3.6 Discrete Fracture Networks) except that the width of the fractures was defined as,

$$w = 3.33L \times 10^{-4} \tag{3.12}$$

First, a flow simulation of a NaCl tracer was carried out and the resistivity of the reservoir defined from the tracer distribution. Next, the electric field was calculated for different timesteps, from before any tracer had been injected into the reservoir and up to 3 days of injection. The tracer production histories and the electric potential differences for the four cases in Figure 3.13 are shown in Figure 3.14 and Figure 3.15.

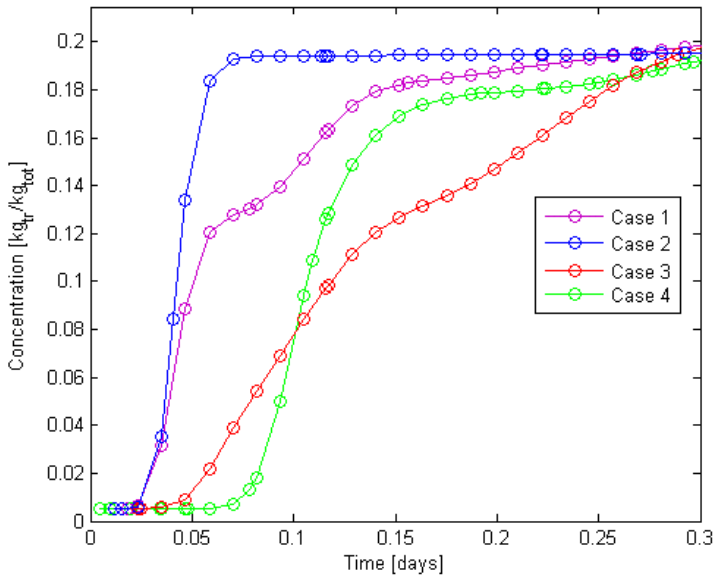

Figure 3.14: Tracer production history for Cases 1-4.

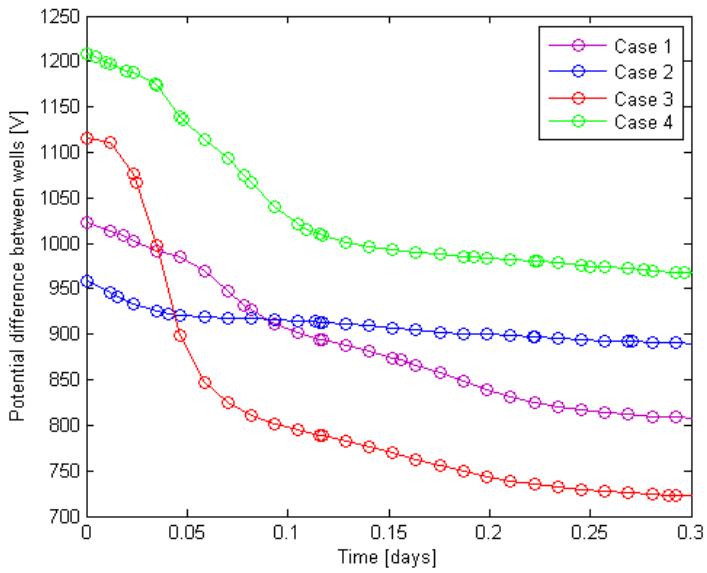

Figure 3.15: Potential difference between wells for Cases 1-4.

The conductive tracer reaches the production well fastest through the fracture network in Case 2 but the potential difference drops the most in Case 3. These differences in the histories of the tracer production and of the potential difference are due to the previous conclusion that the electric potential and tracer production depend on the fracture networks and can therefore give information about the fracture characteristics. The objective function of the inverse analysis was defined as the sum of the difference between the tracer production histories and the difference between the histories of the potential difference between the injector and the producer. The Genetic Algorithm was modified to force the chromosomes to be integers between 1 and 4, where the integer corresponds to Cases 1-4. One of the four cases was chosen and the inverse analysis used to identify the chosen fracture pattern. The Genetic Algorithm was able to identify the correct fracture patterns in all cases. However, because the variable being optimized is an integer corresponding to

different fracture networks, the Genetic Algorithm acts like a grid search algorithm where each fracture network needs to be tested unless a perfect match has been found. An increase in the variable, i.e. the case number, does not indicate a certain change in the fracture pattern because all the patterns were generated randomly. Therefore, it would be impossible to find the best fitted fracture network without checking all the possible networks. In reality, it would not be applicable to use grid search to try all networks because of the gigantic number of possible fracture patterns, so a relationship needs to exist between a certain change in the integer being optimized and the equivalent change in the corresponding fracture network. In practice, the intent is not to estimate the exact map of the fractures, but only to determine the character of the network in terms of connectivity and transmissivity.

3.9 FUTURE WORK

Future work includes investigating ways to use inverse analysis with tracer concentration simulations and electric potential calculations from TOUGH2 to characterize fracture networks. The possibility of defining the reservoirs using fractal dimensions and distributions will be explored and the potential of using gradual deformation for optimization. It is also of interest to implement self-potential calculations into the model since the change in self-potential affects the measured potential difference and could facilitate fracture characterization. Other future goals are to study the use of nanotracers and different chemical tracer as well as to explore the influence of injecting varying tracer concentration. Different well arrangements will also be studied to estimate the minimum number of measurement locations necessary to solve the inverse problem efficiently. The objective is to develop a method which can be used to find where fractures are located and the character of their distribution.

4. FRACTURE CHARACTERIZATION USING THERMAL AND TRACER DATA

This research project is being conducted by Research Assistant Carla Kathryn Co and Professor Roland Horne. The overall objective of this study is to develop a methodology to estimate fracture dimensions. Our current focus is on utilizing temperature, tracer, and borehole imaging data to determine relevant fracture parameters.

4.1 SUMMARY

This study aims to describe interwell connections through characterization of permeable zones in geothermal wells. Several model configurations were described and investigated. A single fracture model was used to represent the connectivity between injection and production well pairs. An analytical model derived by Gringarten and Sauty (1975) was used to estimate the fracture aperture from thermal breakthrough time and mean tracer arrival time. Estimated effective fracture aperture values were from 2.1 cm to 42.6 cm.

To understand the characterization of fractures further, a literature review was undertaken. Conventional and EGS fields included in this study were: Desert Peak, Nevada; Dixie Valley, Nevada; Soultz, France; The Geysers, California; and Wairakei, New Zealand. Fracture properties were determined from acoustic imaging techniques. Feed zone locations identified through Pressure, Temperature, and Spinner (PTS) data were then correlated to these properties. Results showed that feed zone locations correspond to depths with higher apertures. Fracture density, however, was not found to be relevant to fluid entry zones.

Comparison of cooling rate predictions from three interwell connection models was done using data from Palinpinon geothermal field (Maturgo et al., 2010). These three models were: single fracture model; porous model with heat loss; and isotropic porous medium model (Bodvarsson, 1972) using the software ICEBOX. Results for temperature drawdown versus time showed that all three models predict values within 50°C. This illustrated the viability of using a single effective aperture to characterize producer-injector well connections and predict the thermal effect of different injection scenarios.

An extensive literature review was undertaken last quarter to investigate the possibility of integrating scaling relationships with heat and mass transport to improve the single effective fracture model. The main goal was to model fracture networks that were more consistent with the observed patterns in the field. Scaling relationships between relevant fracture properties such as aperture, length, and density were envisioned to become useful in constraining the possible models derived from tracer analysis and temperature matching. Field studies revealed that scaling had been observed in numerous geothermal fields in various scales ranging from thin sections to aerial photographs.

Stratigraphy is found to be important mainly for shallow permeable zones only. Moreover, fractures most relevant to flow are optimally-oriented and critically-stressed. In addition, either high fracture aperture or high fracture density values can be used to identify

permeable zones depending on the degree of fracture overlap in the borehole image logs. Future work will focus on uncertainty analysis of scaling correlations and borehole imaging derived data to improve analytical models and reservoir simulations.

4.2 INTRODUCTION

Injection of spent brine and condensate is practiced widely in geothermal fields for pressure support and wastewater disposal (Horne, 1996). However, premature thermal breakthrough can occur if this is not managed properly. Therefore, determination of interwell connectivity is important for proper reservoir management. Connectivity between production and injection wells can be represented by different permeable zone configurations with their corresponding tracer and heat transport analytical models. Figure 4.1a describes a single fracture connection model (Co and Horne, 2011; Horne, 1996). The second model (Figure 4.1b) uses a well-developed major fault with an impermeable core and permeable damage zones (Massart et al., 2010; Paul et al., 2009, Paul et al., 2011; Johri et al., 2012). A third model, shown in Figure 4.1c, utilizes sheared fracture planes or porous channels (Bullivant and O'Sullivan, 1985; Lauwerier, 1955; Gringarten and Sauty, 1975) that can be attributed to secondary structures subparallel to major faults. In addition, horizontal sheared fracture planes can be used to model lithological boundaries. Lastly, the fourth model (Figure 4.1d) describes the intersection of cross-cutting sheared fracture planes as possible geothermal permeable zones. These could be represented by parallel plate models (Gringarten et al., 1975, Rivera et al., 1987). The focus of this quarter report will be on the first two models.

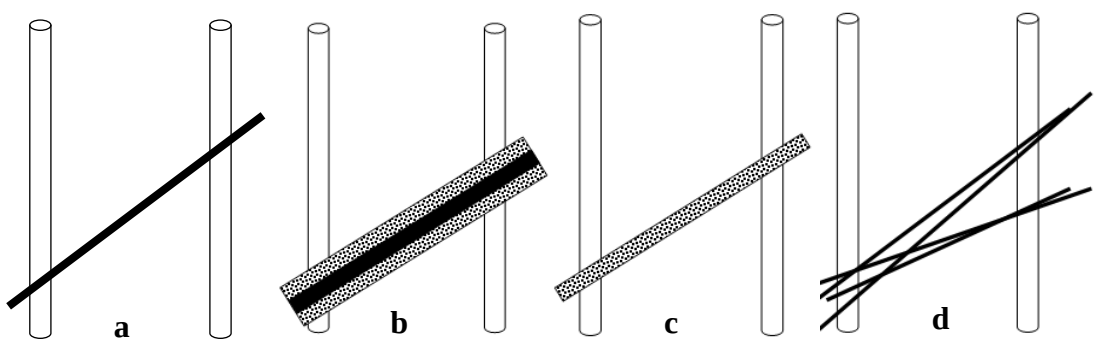

Figure 4.1 Interwell connectivity configurations: (A) single fracture connection; (B) well-developed fault with damage zone with a low permeability core; (C) secondary structures subparallel to faults or stratigraphy based connections; (D) cross-cutting sheared fracture planes.

Fracture aperture is an important parameter in geothermal reservoirs. Aperture influences transport and thermal behavior of the reservoir, both in EGS and in conventional hydrothermal systems. An important application is the determination of the degree of interwell connectivity. Of critical importance is the prevention of thermal breakthrough from injection wells to production wells.

During the 1980s, several unsuccessful attempts were made to estimate fracture aperture by matching tracer test data. This was because the parameter estimation problem had

multiple degrees of freedom, which made it difficult to separate fracture aperture from other unknown reservoir parameters. To constrain the degrees of freedom, thermal response data could be used. This was proposed in the 1980s; however at the time no data existed that provided both tracer and thermal responses. Now that several EGS and fractured reservoirs have been monitored to provide these data, the possibility exists to estimate fracture aperture in those fields. A single fracture model was used to describe the connectivity of an injection and production well pair. Tracer and thermal data were used to estimate the fracture width for this simplified model.

The objective of the initial work done was to determine whether it would be feasible to derive reasonable estimates for the fracture aperture using both temperature data and tracer test results. Another objective was to document existing analytical models and field data available in literature. Calculated fracture width values were compared to those derived from other datasets to check for consistency. Temperature drawdown predictions from the single fracture model were then compared to those from two versions of porous models. One was a porous model with heat loss and the other was calculated using ICEBOX software. This comparison was done for the Palinpinon geothermal field data (Maturgo et al., 2010).

Focus last quarter has been on understanding the significance of the fracture aperture in predicting possible fracture network models. A comprehensive literature review of the scaling of fracture properties in geothermal reservoirs was undertaken to define the relationships among fracture properties such as aperture, length, and density. Moreover, acoustic imaging data was used to correlate these fracture properties to feed zone locations. This quarter, two additional field datasets from Dixie Valley and Soultz geothermal fields were included. Furthermore, the influence of fracture orientation and lithology on feed zone locations was investigated. In addition, scaling correlations for damage zone fracture density was used to derive an effective permeability for faults.

4.3 COMBINED TRACER AND TEMPERATURE ANALYTICAL MODELS

4.3.1 Single Fracture Model:

Fracture Aperture

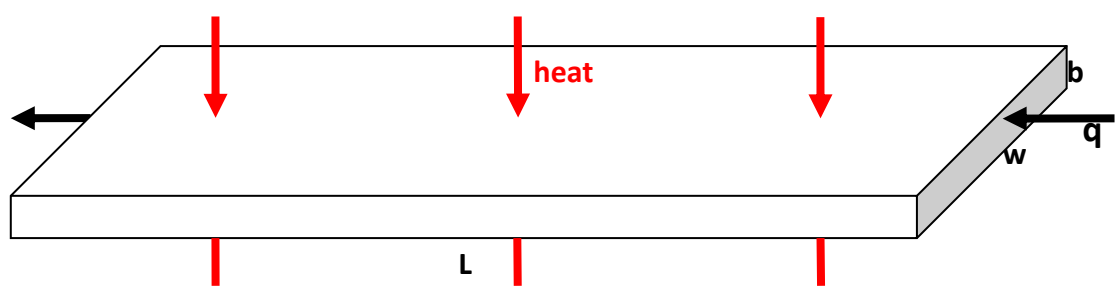

Figure 4.2 Model schematic for the Gringarten and Sauty (1975) derivation

Gringarten and Sauty (1975) derived a solution that can be used for unsteady-state one-dimensional heat transfer through a fracture as shown in Figure 4.2. The solution was similar to that for a porous medium, derived by Lauwerier (1955). The solution assumes a thin, uniform reservoir with an adiabatic boundary. Heat is transferred by conduction from the rock layers and the entering fluid. As no mixing is assumed, the result is a stream-like channel flow.

Horne (1996) derived the resulting analytical solution for this model as Equation 4.1 where t_c is the tracer front arrival time, t_{th} is the thermal breakthrough time, and b is the fracture aperture. On the left hand side of Equation 4.1 is the relative temperature ratio T_{ratio}. Here, T_o is the original reservoir temperature, T_w is the reservoir temperature at x, and T_{inj} is the injected fluid temperature. Thus, the fracture aperture can be determined using the thermal and tracer breakthrough data. Knowledge of the fracture aperture can then be used to predict temperature drawdown in producing wells.

$$T_{ratio} = \frac{T_o - T_w}{T_o - T_{inj}} = erfc\left\{\left[\frac{(\rho_w C_w)^2}{K_r \rho_r C_r}\left(\frac{b}{t_c}\right)^2 (t_{th} - t_c)\right]^{-\frac{1}{2}}\right\} \tag{4.1}$$

$$b = \left\{\left(erfc^{-1}\left[\frac{T_o - T_w}{T_o - T_{inj}}\right]\right)^{-2} \frac{t_c^2}{(t_{th} - t_c)} \frac{K_r \rho_r C_r}{(\rho_w C_w)^2}\right\}^{1/2} \tag{4.2}$$

These are the analytical expressions used to model a single fracture connection between an injector and producer well pair. Equation 4.2 calculates the effective fracture aperture from the thermal arrival time t_{th}; tracer front arrival time t_c; and relative temperature ratio T_{ratio}.

Cooling Rate Predictions

$$T_w = T_o - (T_o - T_{inj}) erfc\left\{\left[\frac{(\rho_w C_w)^2}{K_r \rho_r C_r}\left(\frac{qb}{A_{tracer} x}\right)^2 \left(t - \left(\frac{\rho_A C_A}{\rho_w C_w}\right)\frac{A_{tracer} x}{q}\right)\right]^{-\frac{1}{2}}\right\} \tag{4.3}$$

$$\rho_A C_A = \phi \rho_w C_w + (1 - \phi)\rho_r C_r \tag{4.4}$$

$$A_{tracer} = \phi A_{crosssection} \tag{4.5}$$

$$A_{\max} = \frac{q_{total}}{v_{mean}} \tag{4.6}$$

$$q = q_{total}\left(\frac{A_{tracer}}{A_{\max}}\right) \tag{4.7}$$

The general equation for temperature versus time as derived by Gringarten and Sauty (1975) is shown in Equation 4.3. Here, x is the distance between the injection well and producer well. Thus, once the aperture b is determined, this equation describes the cooling of producing feed zones due to injection with constant volumetric rate (q) and temperature (T_{inj}). Note that q specified here is not the total injection rate. It is the rate of effective injected volume that goes to a particular producer. This is approximated by getting the ratio of the area derived from tracer analysis to the maximum area based on the total injection rate and the observed mean velocity from tracer data. Equations 4.5 to 4.7 illustrate these in more detail.

4.3.2 Porous Channel with Heat Loss Model: Cooling Rate Predictions

Maturgo et al. (2010) use tracer analysis to determine the effective area (A_{tracer}) for two injector and producer well pairs. These are NJ3D-SG2RD and NJ2RD-NJ5D. Using parameters from the general equation and the effective cross sectional area, thermal velocity without heat loss (v_{th}) can be defined as shown in Equation 4.8. From this definition, Equation 4.3 can be rearranged to get Equation 4.9 which describes the cooling effect of injection for a porous connection model. As explained in the previous section, q is the effective volumetric injection rate.

$$v_{th} = \frac{q}{A_{tracer}} \frac{\rho_w C_w}{\rho_A C_A} = v_w \phi \tag{4.8}$$

$$T_w = T_o - \left(T_o - T_{inj}\right) erfc\left\{\left[\frac{\left(\rho_A C_A\right)^2}{K_r \rho_r C_r} \frac{v_{th}^2 b^2}{x^2}\left(t - \frac{x}{v_{th}}\right)\right]^{-\frac{1}{2}}\right\} \tag{4.9}$$

4.4 RESULTS FROM COMBINED TRACER AND TEMPERATURE ANALYSIS

4.4.1 Available Tracer and Temperature data

Results from tracer tests in EGS and conventional fractured geothermal reservoirs have been reported frequently in the literature. However, thermal breakthrough data are not as widely published. For EGS fields, thermal data are obtained usually from long-term circulation tests, as for example in Hijiori, Matsunaga et al. (2002) and Matsunaga et al. (2005). Historic silica geothermometer data are used from Palinpinon field which is a conventional liquid-dominated reservoir, Maturgo et al. (2010). Matsukawa is a conventional vapor-dominated field, Fukuda et al. (2006). Table 4.1 provides a summary of the field data used in this study. The thermal breakthrough time t_{th} here corresponds to the time it takes to reach a T_{ratio} of 0.5.

Table 4.1: Thermal and tracer breakthrough times from field data.

Field	Injector	Producer	t_c	t_{th}	Source
			Days	days	
Hijiori	HDR-1	HDR-2A	1	175	Matsunaga et al. (2002)
	HDR-1	HDR-3	4	266	Matsunaga et al. (2005)
Palinpinon	NJ2RD	NJ5D	15	730[1]	Maturgo et al. (2010)
	SG2RD	NJ3D	28	365	
Matsukawa	M-6	M-8	1.5	146	Fukuda et al. (2006)

4.4.2 Fracture Aperture

As described in the previous section, fracture aperture can be estimated directly from the thermal and tracer breakthrough times. Assumptions for the values of the other parameters are listed in Table 4.2. These are the values assigned to these properties in the estimation of fracture aperture. Actual temperature ratios for the injector-producer pairs derived from long term circulation test results are shown in Table 4.3. Estimated fracture aperture values are given in the same table.

To determine the relative temperature for M-6 and M-8 in Matsukawa, a 60°C injection temperature was assumed. Estimates of effective fracture aperture *b* varied from 2.1 cm to 42.6 cm. Though the HDR-1 and HDR-2A well pair in Hijiori exhibited the shortest mean tracer arrival time, it had the lowest calculated effective aperture value because of the long thermal breakthrough time. This observation demonstrated the value of using both tracer and thermal results to constrain the effective aperture. Using this analytical solution also provided an alternative method to characterize the flow path between wells.

Results from finite element heat and mass transfer modeling (FEHM) of the Hijiori field demonstrates fracture aperture values of about 2 mm (Tenma et al., 2005). This is significantly lower than the calculated aperture values. Further investigation of results from aperture estimates from numerical modeling will be undertaken. However, effective fracture aperture derived from acoustic imaging logs show a range of values consistent with those calculated. The next section will describe these studies in detail.

Table 4.2: Assumptions used in calculations.

Rock thermal conductivity	K_r	2	W/m-C
Rock density	ρ_r	2200	kg/m^3
Water density	ρ_w	900	kg/m^3
Rock heat capacity	C_r	0.712	kJ/kg-C
Water heat capacity	C_w	4.342	kJ/kg-C

[1] Assumed that injection in NJ2RD started in 1998 or 1 year before the start of drawdown in NJ5D based on the Palinpinon injection and production history discussed by Bayon and Ogena (2005).

Table 4.3: Relative temperature ratios and calculated fracture aperture from thermal and tracer breakthrough times.

Field	Injector	Producer	T_{ratio}	Calculated b cm
Hijiori	HDR-1	HDR-2A	0.46	2.1
	HDR-1	HDR-3	0.14	6.9
Palinpinon	NJ2RD	NJ5D	0.17	15.7
	SG2RD	NJ3D	0.07	42.6
Matsukawa	M-6	M-8	0.29[2]	3.5

4.4.3 Cooling Predictions

Comparison of cooling predictions was the most convenient way of relating the various producer-injector well connection models to each other. We wanted to investigate if the different models would give similar temperature drawdown profiles. Assumptions used for cooling rate calculations are shown in Table 4.4. Area values used to determine the effective injection rate going to the producer are in Table 4.5. These values were used by Maturgo et al. (2010) to predict the temperature drawdown due to injection at a constant rate (q_{total}) and temperature (T_{inj}). Palinpinon data was chosen because it had detailed cooling rate calculations available in literature. It also served as an additional verification of the validity of our models and the results of our calculations.

Table 4.4: Parameters used for cooling rate predictions

Field	Injector	Producer	q_{total} m^3/s	T_o °C	T_{inj} °C	L m
Palinpinon	NJ2RD	NJ5D	0.178	265	160	1500
	SG2RD	NJ3D	0.117	265	160	1500

Table 4.5: Effective injection rate calculation

Field	Injector	Producer	A_{max} m^2	A_{tracer} m^2	q m^3/s
Palinpinon	NJ2RD	NJ5D	217.5	50.7	0.041
	SG2RD	NJ3D	175.8	39.7	0.027

Cooling rate or temperature drawdown predictions from three models were compared. First was the single fracture model as described in Equation 4.3. Next was the porous

[2] Assumed an injection temperature of 60°C

model with heat loss using Equation 4.9. The third one was the isotropic porous medium model derived by Bodvarsson (1972) calculated using the ICEBOX software. As described in the previous section, calculation of temperature drawdown for the first two models was straightforward. On the other hand, values for the third model were just lifted from the same paper where data for aperture calculations were obtained (Maturgo et al., 2010).

Figure 4.3 shows the results for NJ2RD-NJ5D while Figure 4.4 illustrates the forecast for NJ3D-SG2RD. Time in the x axis is measured from the start of injection. For NJ2RD-NJ5D, the fracture model gives a prediction very similar to the one using ICEBOX. However, the porous model for this well pair presents a more pessimistic temperature forecast. On the other hand, both the porous model and fracture model agree on a lower stabilized temperature than the ICEBOX model prediction for NJ3D-SG2RD as seen in Figure 4.3. It is still unclear why the three models behaved differently for these two scenarios. Still, it is good that all three models agree within a range of 50°C. This proves that the effective single fracture aperture model is a viable one, as it can be used to predict injection effects. Further investigation using numerical modeling as well as data from other geothermal fields will have to be made.

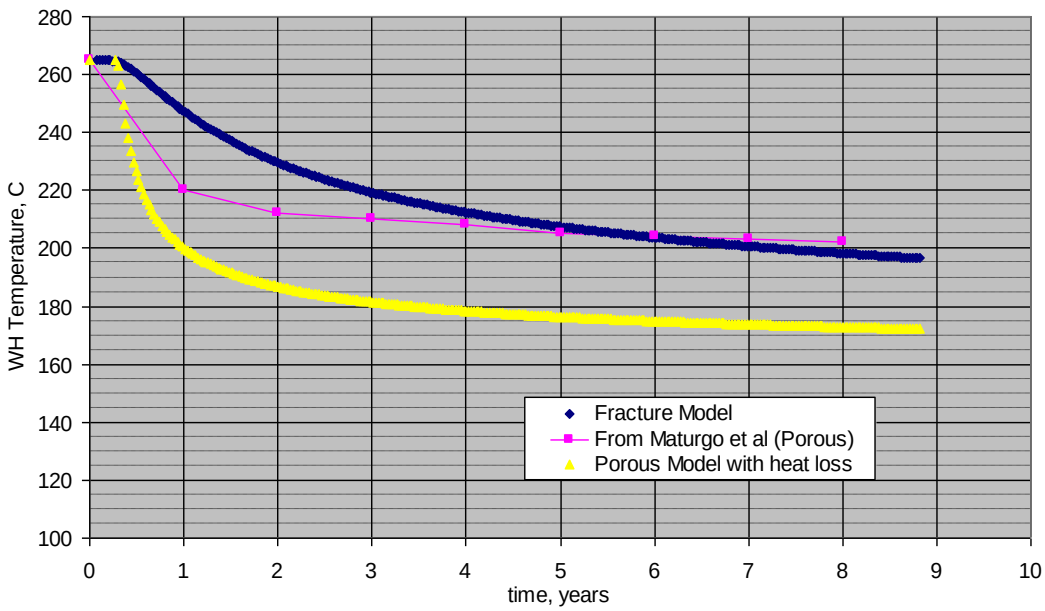

Figure 4.3 Comparison of cooling predictions for NJ2RD-NJ5D from different models: (1) fracture model; (2) porous model with heat loss; (3) ICEBOX (Maturgo et al., 2010).

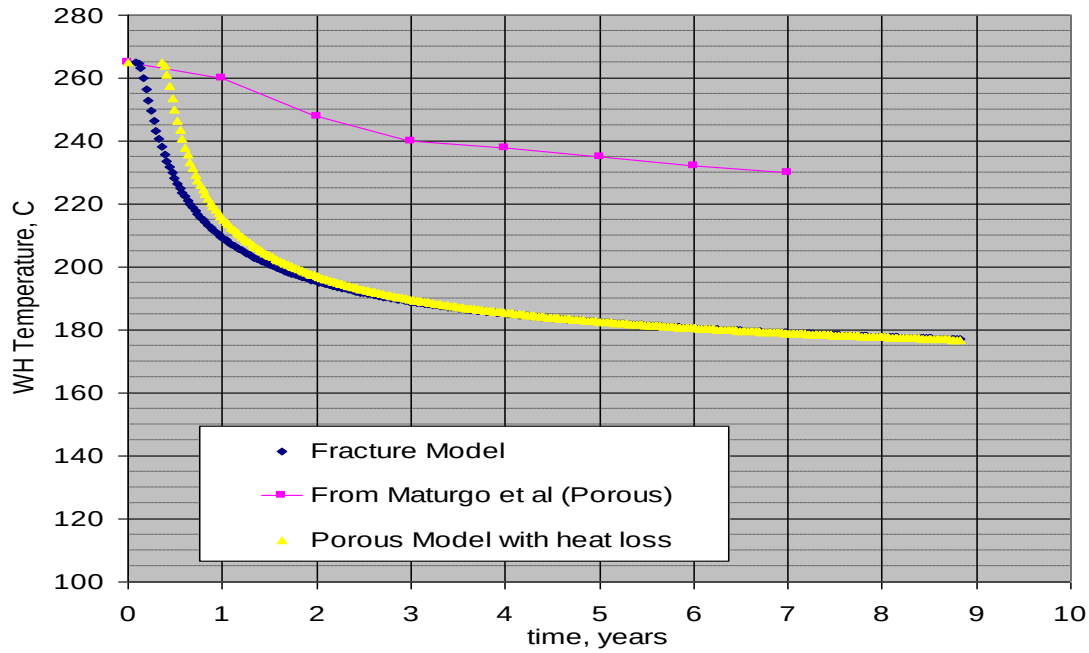

Figure 4.4 Comparison of cooling predictions for NJ3D-SG2RD from different models: (1) fracture model; (2) porous model with heat loss; (3) ICEBOX (Maturgo et al., 2010).

4.5 SCALING CORRELATIONS AND GEOMECHANICS CONCEPTS

4.5.1. Aperture Related Scaling Correlations

Olson (2003) describes the different mechanisms that lead to linear and sublinear scaling of aperture versus length for opening mode cracks. The two most relevant linear elastic fracture mechanics (LEFM) equations are the following:

$$\frac{b_{max}}{L} = \Delta\sigma \frac{2(1-v^2)}{E} = [p_f - \sigma_n] \frac{2(1-v^2)}{E} \tag{4.10}$$

$$\Delta\sigma = \frac{K_I}{\sqrt{\frac{\pi L}{2}}} \tag{4.11}$$

Equation 4.10 describes the relationship of the aperture (b_{max}) to the fracture length (L) for non-interacting opening mode fractures under plane strain conditions (Pollard and Segall, 1987). The other relevant parameters are: opening mode driving stress ($\Delta\sigma$), Poisson's ratio (v), and Young's modulus (E). Another definition for the driving stress is $(p_f - \sigma_n)$ where, p_f is the internal fluid pressure and σ_n is the remote normal compressive stress perpendicular to the crack. Furthermore, the driving stress ($\Delta\sigma$) for a uniformly loaded fracture can be expressed in terms of the stress intensity factor at the crack tip (K_I) and fracture length (L) as shown in Equation 4.11.

$$b_{max} = \Delta\sigma \frac{2(1-\gamma^2)}{E} L = CL \tag{4.12}$$

Linear scaling can be derived from Equation 4.10 assuming a constant driving stress condition (Equation 4.12). Additionally, C is a constant representing material properties and external stress conditions. The possibility of reaching an unstable dynamic crack growth condition increases as the crack propagates. This is because at constant driving stress, the stress intensity factor (K_I) is proportional to the fracture length (L) (Equation 4.11). Moreover, the minimum requirement for crack propagation is for K_I to be equal to the intrinsic fracture toughness of the material (K_{Ic}). Therefore, extensive crack tip branching behavior should be observed where linear scaling is applicable. Olson (2003) states that this is only possible when there is relaxed loading such as after propagation. In contrast, Scholz (2010) argues that this is the predominant mode of scaling based on the reanalysis of data. Calculated (C) values range from 0.1 to 0.001 (Scholz, 2010).

$$b_{max} = \frac{K_{Ic}(1-\gamma^2)}{E\sqrt{\pi/8}}\sqrt{L} \tag{4.13}$$

On the other hand, Olson (2003) claims that sublinear scaling is considered to be the most prevalent mechanism for most geologic conditions. Furthermore, Olson and Schultz (2011) insist that square root scaling provides the best fit for each data set. Sublinear or square root scaling can be derived from the assumption of constant stress intensity factor (K_I) equal to the intrinsic fracture toughness of the material (K_{Ic}) for critical crack propagation as presented in Equation 4.13 (Olson, 2003). Fracture arrest will occur once the internal fluid pressure goes down or the remote stresses are relieved due to propagation. In addition, sublinear scaling can also happen for subcritical crack growth where the rock has less resistance to failure due to corrosive fluids and long-term loading.

$$b_{max} = CL^e \tag{4.14}$$

$$b_{max} = \frac{4}{\pi} b_{measured} \tag{4.15}$$

Fracture data from various fields across multiple length scales (1 cm to 2 km) were fitted to a power law equation (Equation 4.14). The maximum aperture (b_{max}) can be derived from the measured aperture ($b_{measured}$) using Equation 4.15 for an elliptical opening distribution. Here, e was the scaling exponent and C was a constant. Values calculated by Olson (2003) for e ranged from 0.38 to 0.41. The deviation from the predicted exponent value of 0.5 could be due to several other interfering factors. One example of this was the mechanical interaction of multisegment features. Thus, overlapping multisegment fractures would behave like one long fracture. Another was the presence of strata boundaries such that the aperture scales with the fracture height (H) instead of length (L).

Renshaw and Park (1997) examined data from the Krafla fissure swarm in Iceland and observed a break in slope for the aperture (b) versus length (L) when L reaches the maximum value. They postulated that this threshold value was the length at which the smaller apertures were affected by stress perturbations of larger fractures. Superlinear scaling was observed for smaller fractures while linear scaling was observed for larger ones.

Ishibashi et al. (2012) evaluated the scale dependency of various parameters such as: tortuosity, permeability, fraction of area contacted by fluid, and the geometric mean of the aperture. This was done using confined pressure flow experiments and subsequent numerical modeling of sheared versus mated fracture planes in multiple scales (37.5 cm^2, 150 cm^2, and 600 cm^2). These fracture planes were created in a cube of Inada granite from Ibaraki, Japan using a wedge with a shear displacement of 5 mm in the radial direction for the sheared fracture. Their results showed that for the mated fracture, there was a scaling effect only for tortuosity and the mean aperture. On the other hand, sheared fractures planes exhibited sublinear scaling for all the parameters examined except for the fluid contacted area fraction. Moreover, channeling flow within the fracture plane was observed due to a log-normal distribution of aperture within it. Therefore, high aperture connections would be the dominant flow paths such that the contacted area fraction would not depend on the scale. Another important finding of this study was that sheared fractures had calculated permeability values that were three orders of magnitude higher than the equivalent mated one even though the shear displacement was just 5mm. This was consistent with the notion that sheared fracture planes models were more appropriate than opening mode ones for fractures obtained through borehole imaging.

4.5.2. Density Related Scaling Correlations

Density-Aperture Scaling

Statistical analysis of borehole imaging data from the Soultz geothermal field revealed an inverse linear scaling of fracture density and mean width across scales ranging from 1 to 1000 cm with a fractal dimension of 1.04 (Massart et al., 2010). Strong clustering was inferred from the low fractal dimension value. This result was consistent with Marrett et al. (1999), which analyzed data sets from natural faults and extension fractures and validated that the data follow power-law scaling in multiple-observational scales. Results from their study showed that the power-law scaling applied across six ranges of scale within reasonable uncertainty limits. Therefore, zones with higher fracture aperture values would have smaller fracture density values. Based on this, regions with fluid entry zones should have lower fracture densities.

Sammis et al. (1991) observed the same behavior at The Geysers geothermal field where it was found that fracture patterns in shear zones exhibited fractal geometry. Fracture networks on an outcrop from a freshly cut vertical wall (dm scale) were mapped and analyzed for the fractal dimension using the box counting method. The calculated fractal dimensions had values that ranged from 1.87 to 1.926 (Sammis et al., 1991). Two additional maps from larger scales were analyzed for self-similarity (Sammis et al., 1992). One was from a road-cut outcrop (m scale) and the other was from a regional map of the area (km scale). Density versus fracture length scaling was likewise observed in all length scales. It was observed from core analysis that most of the small fractures were sealed. One conclusion was that transport occurred through large shear fractures.

Damage Zone Fracture Density-Perpendicular Fault Distance Scaling

Fracture density scaling in damage zones of the San Andreas Fault and faults in the Suban gas field were investigated by Johri et al. (2012). Image and geophysical logs were used to ascertain properties of the damage zones at depth. It was found that the damage zone fracture density (F) versus perpendicular distance from the fault (r) followed an inverse power-law scaling behavior (Equation 4.16). F_o was the fault constant and n was the fractal dimension. Based on the data, n had values from 0.68 to 1 with an average value of 0.8. This fractal dimension was dependent on the lithology.

$$F = F_o r^{-n} \tag{4.16}$$

Paul et al. (2009) used dynamic-rupture propagation modeling to calculate the scope of damage zone along a fault for the CS field located between Australia and Indonesia. Secondary faults developed were oriented parallel to the major fault with higher dip angles. These faults, therefore, were at an optimal orientation for failure. This meant that they would be conduits for flow as described by Barton et al. (1995). Similar to Johri et al. (2010), this study found that damage intensity decreases with distance from the fault plane. Higher permeability values would be expected in the direction parallel to the strike of the major fault. In contrast, the direction perpendicular to the fault strike would have lower permeability if the fault were sealing due to a well-developed core. This would create field-scale permeability anisotropy that must be taken into account for reservoir simulation as modeled by Paul et al. (2011). Inclusion of fault damage zones in reservoir simulation led to a better history match and the uncertainty in simulation was investigated using multiple equally probable models (Paul et al., 2011).

Figure 4.5 shows a schematic for the parallel network configuration of porous channels to model this anisotropy. An equivalent inverse power-law scaling of the damage zone permeability with distance is shown in Equation 4.17. k_D is the damage zone permeability at a distance (y) away from the fault, k_o is the permeability right outside the core, and k_m is the low fault core permeability. To characterize the field-scale anisotropy, an approximate equivalent permeability for flow in the x ($\overline{k_x}$) and y ($\overline{k_y}$) directions can be derived (Equations 4.18 and 4.19) where, u is the velocity, μ is the fluid viscosity, and p is the pressure. Assuming that c is very small compared to the total width of the damage zone, equivalent parallel (x direction) and series (y direction) permeability values are defined by Equations 4.20 and 4.21, respectively. Expressing these two equations in integral form and substituting the inverse power-law scaling correlation, Equations 4.22 and 4.23 can be derived. For the x direction or flow parallel to the strike of the fault, the permeability increases with damage zone width (W_T) and decreases with core width (c). In addition, the matrix permeability has little effect on the overall permeability because flow in this direction can go through the other more permeable zones. However, flow in the y direction perpendicular to the fault plane (Equation 4.23) exhibits a possible sealing effect when the fault core permeability (k_m) is very small.

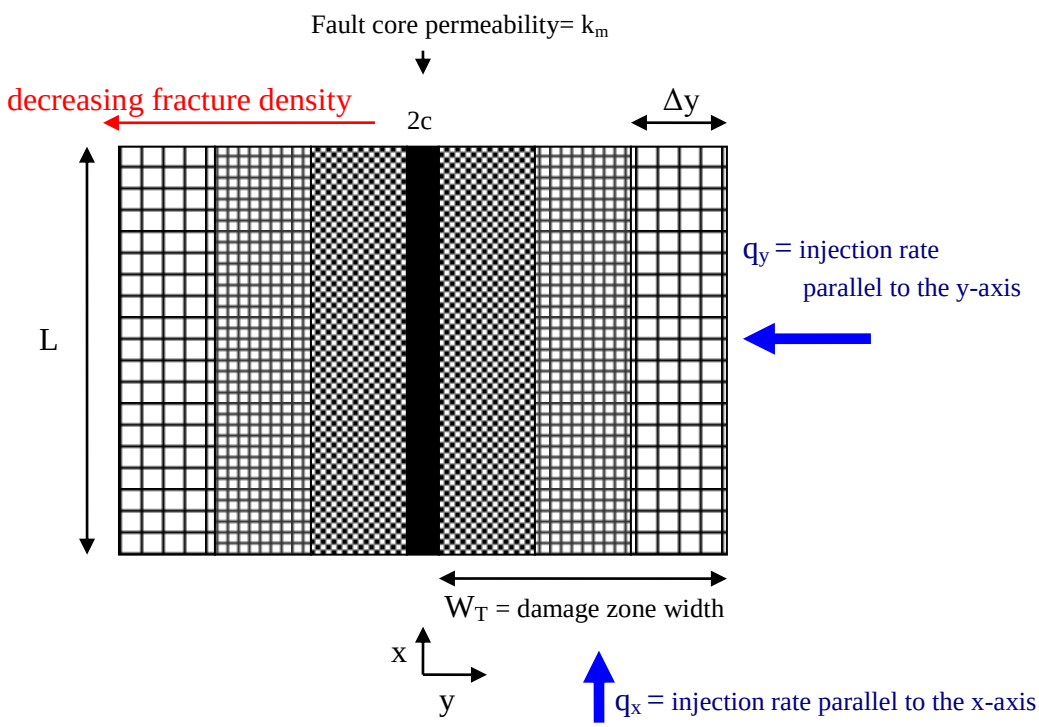

Figure 4.5 Schematic for a fault damage zone model.

$$k_D = k_o y^{-n} \tag{4.17}$$

$$u_x = -\frac{\overline{k_x}}{\mu}\frac{dp}{dx} \tag{4.18}$$

$$u_y = -\frac{\overline{k_y}}{\mu}\frac{dp}{dx} \tag{4.19}$$

$$\overline{k_x} = \frac{2\sum_i k_{f,i}\Delta y_i + 2k_m c}{2\sum_i \Delta y_i + 2c} \tag{4.20}$$

$$\overline{k_y} = \frac{2\sum_i \Delta y_i + 2c}{2\sum_i \frac{\Delta y_i}{k_{f,i}} + 2\frac{c}{k_m}} \tag{4.21}$$

$$\overline{k_x} = \frac{\int_c^{W_T} k_o y^{-n} dy + k_m c}{W_T + c} = \begin{cases} \dfrac{k_o\left(\dfrac{W_T^{1-n} - c^{1-n}}{1-n} + \dfrac{k_m}{k_o} c\right)}{W_T + c} & n \neq 1 \\ \dfrac{k_o\left(\ln\left[\dfrac{W_T}{c}\right] + \dfrac{k_m}{k_o} c\right)}{W_T + c} & n = 1 \end{cases} \tag{4.22}$$

$$\overline{k_y} = \frac{W_T + c}{\int_c^{W_T} \dfrac{dy}{k_o y^{-n}} + \dfrac{c}{k_m}} = \frac{k_o\left(W_T + c\right)}{\left(\dfrac{W_T^{1+n} - c^{1+n}}{1+n} + \dfrac{k_o}{k_m} c\right)} \tag{4.23}$$

4.5.3. Fractal Dimension Determination

Sammis et al. (1991) also observed that fracture patterns in shear zones were self-similar which meant that they could be characterized using fractal geometry. This rendered classical differential equations of transport for nonfractal media as inadequate. Hence, fracture networks on an outcrop from a freshly cut vertical wall (dm scale) were mapped and analyzed for the fractal dimension using the box counting method. Results confirmed self-similarity with the calculated fractal dimensions ranging from 1.87 to 1.926 (Sammis et al., 1991).

In a follow-up study (Sammis et al., 1992), similarity was investigated for other scales by analyzing two additional maps from larger scales. The first was from a road-cut outcrop (m scale) and the other was from a regional map of the area (km scale). Density versus fracture length scaling was observed in all length scales. Core observations were also performed. It was observed that most of the small fractures are sealed so a tentative conclusion was that transport occurs through large shear fractures. Using statistical analysis of the steam zone distributions, it was determined that the spacing of the relevant fractures was between 300 and 900 m (Sammis et al., 1992). Lastly, depths with high rate of penetration (ROP) over short distances in drilling logs were consistent with steam feed zone locations because they represent highly sheared rocks.

Different fractal analysis methods on various scales for two geothermal reservoirs, Germencik and Kizildere, in southwestern Turkey were used by Babadagli (2000). Analysis was done at four scales. Aerial photographs were used for the km scales and the calculated fractal dimensions were 1.575 and 1.583. Similarly, outcrop photos were used for the m scale and fractal dimensions ranged from 1.07 to 2. Then, rock samples were analyzed for the cm scale which resulted to a fractal dimension range of 1.161 to 1.257. Lastly, thin sections were examined for the micrometer scale and the fractal dimension ranged from 1.011 to 1.039. Overall, linear scaling was observed consistently across all scales.

Tateno et al. (1995) studied cores from the Kakkonda geothermal field and also concluded that the fractures can be described by fractals. Another conclusion was that fractal dimensions varied with the fracture type and location due to the difference in fracture formation processes. Calculated fractal dimensions ranged from 0.38 to 0.53.

4.5.4. Critically-Stressed Fault Identification

Equation 4.24 describes the critical shear stress magnitude for frictional sliding of faults using the Coulomb failure criterion (Zoback, 2007). Here, μ is the coefficient of friction along the plane and S is the cohesion. Normal and shear stresses on the plane are σ_N and τ, respectively. P_p is the pore pressure within the fault. Faults are optimally oriented when the stress ratio of shear and effective normal stresses $\left(\tau/\left(\sigma_N - P_p\right)\right)$ is at a maximum. Assuming that there is no cohesion and using a normal faulting regime (applicable to all the field cases in this study), sliding will occur at a critical minimum horizontal compressive stress value ($S_{h\min crit}$) shown in Equation 4.25. Here, μ is the coefficient of friction of preexisting faults. For conjugate normal faults, the critical stress orientation has a strike parallel to the maximum horizontal principal stress (S_{Hmax}) and a dip of 60 degrees for μ=0.6 (Zoback, 2007).

$$|\tau| = \tau_{crit} = \mu\left(\sigma_N - P_p\right) + S \tag{4.24}$$

$$S_{h\min crit} = \frac{\left(S_V - P_p\right)}{\left(\left(\mu^2 + 1\right)^{1/2} + \mu\right)^2 + P_p} \tag{4.25}$$

Pore pressure versus depth can be calculated from the water density versus depth logs. Typical values used for μ range from 0.6 to 1.0 (Zoback, 2007; Hickman et al., 1997). The magnitude of the minimum horizontal compressive stress (S_{hmin}) can be determined from the instantaneous shut-in pressure (ISIP) (Hickman et al., 1997; Zoback, 2007). ISIP is the pressure, after the well is shut-in during hydraulic fracture tests, at which the pressure drawdown curve deviates from the initial linear behavior. Contrary to this, the magnitude of S_{Hmax} is harder to obtain. S_{Hmax} values can be constrained using a stress polygon with the following information: presence or absence of wellbore breakouts and tensile fractures; rock strength; and faulting regime (Zoback, 2007). Overburden stress (S_v) can be derived from geophysical density logs and laboratory measurement of surface rock density (Hickman et al., 1997). In terms of orientation, drilling-induced tensile fractures along the borehole wall occur when the stress concentration around the wellbore becomes greater the tensile strength of the rock (Barton et al., 2009). These will propagate parallel to the direction of S_{Hmax} and perpendicular to S_{hmin} (Zoback, 2007; Barton et al., 2009; Hickman et al., 1997).

4.6 CORRELATION OF FRACTURE PROPERTIES AND LITHOLOGY TO PERMEABLE ZONE LOCATIONS

Characterization of fluid flow in fractures is an important area of study in geothermal reservoir engineering. Overall permeability in these reservoirs is fault-dominated (Massart

et al., 2010). Relevant fracture parameters to fluid flow are: orientation, aperture, extension, and density. These parameters influence transport and thermal behavior of the reservoir, both in enhanced geothermal systems (EGS) and in conventional hydrothermal systems. Recent advances in borehole imaging technology have made it possible to measure fracture properties with greater accuracy.

For the Wairakei geothermal field, McLean and McNamara (2011) used a high temperature acoustic formation imaging tool (AFIT) to collect fracture data. Confidence, azimuth, and amplitude filters were applied to the data prior to analysis. A borehole televiewer (BHTV) similar to AFIT was used in the Desert Peak EGS project. In addition, formation microscanner (FMS) image logs were utilized (Devatzes, 2009). Published fracture data from various geothermal fields were collected and analyzed. Data sets examined for this study were fracture aperture, density, and orientation. These were then compared to locations of feed zones to determine their correlation with fluid flow properties.

4.6.1 Fracture Aperture

Fracture data from the various geothermal fields showed consistent correspondence between fracture apertures and feed zone locations for most of the data points. In Wairakei, fracture apertures for the feed zones ranged from 10 to 60 cm in wells WK-404, WK-318, and WK-407 (McLean and McNamara, 2011) as shown in Figures 4.6 to 4.8. Moreover, it was found that the narrower azimuth filter yielded a better match of large fractures to permeable zones. There were some cases, however, where the depths of the permeable zones from completions testing did not align perfectly with the large aperture fractures. Minor depth discrepancies can be attributed to wireline stretching and slight depth measurement errors between logging runs.

A similar trend was observed from the Desert Peak data. Collected data included the following: permeable zone locations, PTS data, and fracture apertures from borehole imaging data. Because the injection rate used was small and the well diameter was large, spinner data could not be interpreted (Devatzes and Hickman, 2009). Thus, temperature gradient anomalies were used to identify permeable zones. Data for well 27-15 (Figure 4.9) had aperture values from 1 to 10 cm at fluid entry zones (Devatzes and Hickman, 2009).

There are two possible explanations for this observation. Using a parallel-plate model, fracture permeability is proportional to b^2, where b is the fracture aperture (Jourde et al., 2002). Fluid entry, associated to fractures in geothermal reservoirs, occurs at depths with high permeability. Therefore, permeable zone locations will be at depths with high apertures. Another rationale is the power-law scaling between joint length and width described by Scholz (2010). He argues that for opening mode in rocks, fracture toughness scales linearly with $\sqrt{L}$ and b scales linearly with L, where L is the length. Therefore, a larger fracture width will correspond to a longer fracture which implies a farther reach for the fluid source.

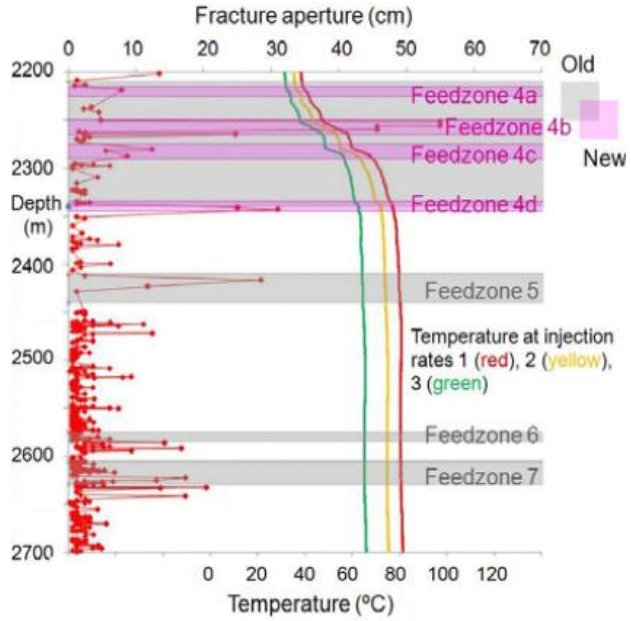

Figure 4.6 Fracture aperture (red) and temperature versus depth for well WK-404 in the Wairakei geothermal field (from McLean and McNamara, 2011)

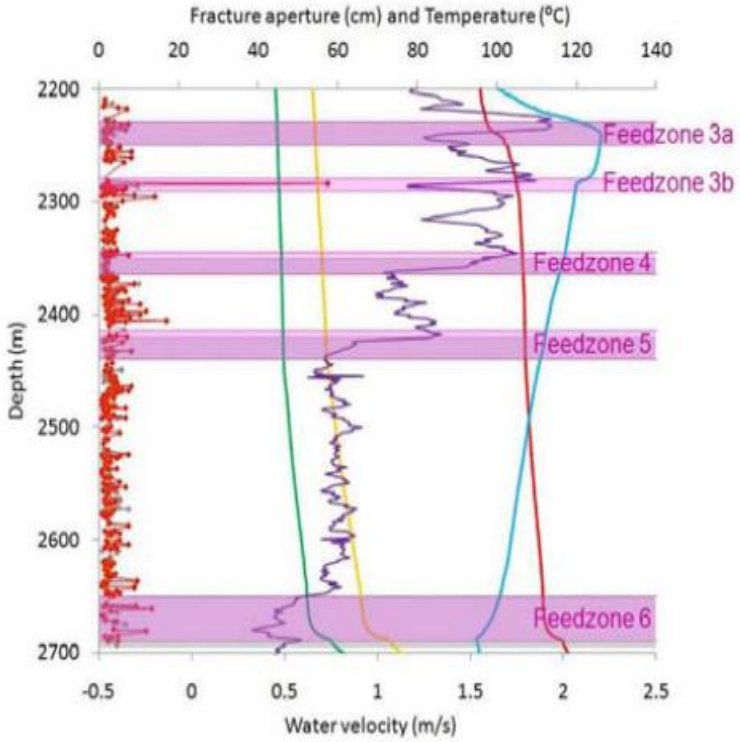

Figure 4.7 Fracture aperture (red), temperature, and spinner velocity (blue) versus depth log for well WK-317 in the Wairakei geothermal field (from McLean and McNamara, 2011)

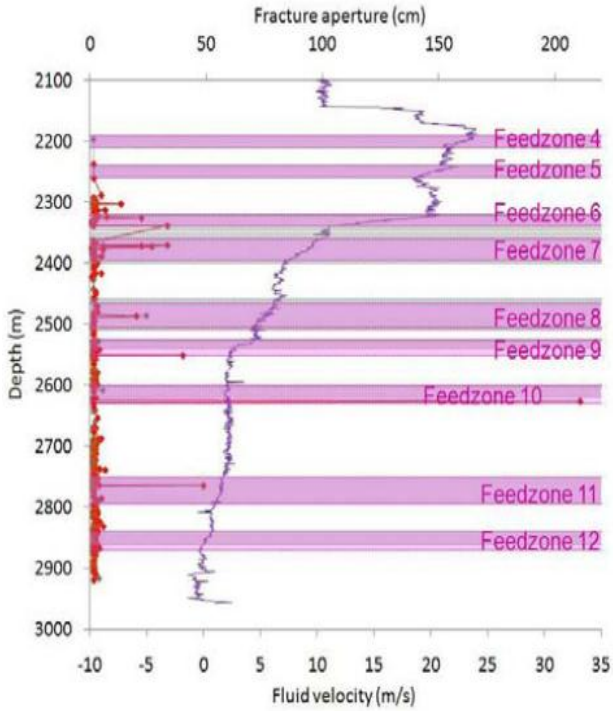

Figure 4.8 Aperture (red) and spinner velocity (blue) versus depth log for well WK-407 in the Wairakei geothermal field (from McLean and McNamara, 2011)

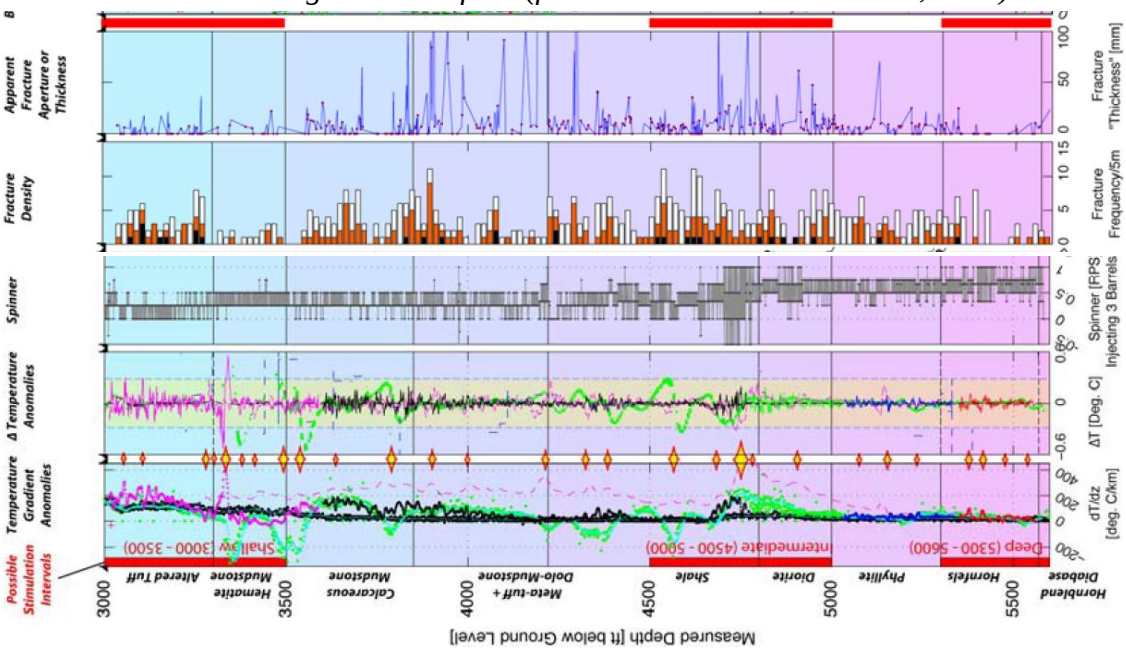

Figure 4.9 Well Log data for well 27-15 in the Desert Peak geothermal field, Nevada. Yellow diamonds indicate feed zones derived from temperature anomalies and spinner velocities (from Devatzes and Hickman, 2009)

4.6.2 Fracture Orientation

For the Wairakei geothermal field (McLean and McNamara, 2011), two additional azimuth filters were employed to include only fractures at optimal orientations. Here, structures were controlled by normal faulting so the optimal fault orientation was parallel or subparallel to S_{Hmax}. Based on the direction of drilling induced tensile fractures, the S_{Hmax} orientation ranged from 035 to 045 degrees strike. Azimuth filters utilized were 45 degrees and 30 degrees from this S_{Hmax} direction. This filtering narrowed the fault orientations to those that were critically-stressed in the current stress regime and would therefore be most likely slip. Permeable zones in this study followed the dominant S_{Hmax} direction within 30 degrees with steep average dips ranging from 66 to 84 degrees.

Hickman et al. (1997) investigated the relationship between permeable zones from temperature gradient anomalies and fracture properties from borehole imaging for the Dixie Valley geothermal field. The S_{Hmax} direction was N33°E which was subparallel to the Stillwater fault. It was ascertained that most of the hydraulically conductive faults were critically-stressed and optimally-oriented with respect to the current stress field striking northeast with varying dips ranging from 15 to 70 degrees. Furthermore, spinner logs showed that only six fractures dominated fluid flow in well 73B-7 and they occurred at a narrow depth range of 2.5 to 2.7 km. Isolated spinner flow meter and pressure logs at two depths (2.614 and 2.637 km) revealed high permeability values of 21 and 48 darcys, respectively. These were inferred to be part of the damage zone of the Stillwater fault. A follow-up study by Barton et al. (1998) used the same analysis for six wells to compare the orientations of fractures in productive and nonproductive geothermal wells. Hydraulically conductive fractures for good producers and segments of the Stillwater fault zone were critically-stressed. On the other hand, hydraulically conductive faults of poor producers were below the Coulomb failure line for μ=0.6 in the Mohr circle.

A similar analysis was done for well 27-15 from the Desert Peak geothermal field which was a candidate for hydraulic fracturing (Devatzes and Hickman, 2009; Hickman and Devatzes, 2010). The azimuth of S_{hmin} was 114 ± 17° which was consistent with the E-SE and W-NW striking orientation of the Rhyolite Ridge normal fault zone in the area with a stress magnitude of 1995 ± 60 psi. However, normal faulting regime in the well was not confirmed but was assumed based on the regional stress regimes. Hydraulic fracturing was planned for intervals that had a significant number of critically-stressed faults.

A previous study on the Cajon Pass scientific drillhole data demonstrated that optimally oriented faults control the overall permeability for reservoirs with low rock matrix permeability such as granite (Barton et al., 1995). Additionally, it was found that relatively few fracture planes dominated flow. Several reasons were given by various studies to explain this correlation for brittle rocks. First, the permeability increase in critically-stressed faults was due to brecciation and damage formation (Zoback, 2007). Second, dilatancy of sheared fracture planes from pore-volume expansion of microcracks would improve both porosity and permeability along the plane (Barton et al., 1995). Third, majority of geologic process such as precipitation, cementation, pressure solution

formation, and mineral alteration led to fracture closure. Hence, slip would be needed to keep fractures open (Zoback, 2007; Hickman et al., 1997).

4.6.3 Fracture Density

McLean and McNamara (2011), in their investigation of data from the Wairakei geothermal field, concluded that there was no correlation observed for fracture density and permeable zone depths. However, the number of interpreted fractures was highly dependent on the image quality. The same problem was encountered for the data of well 27-15 of the Desert Peak geothermal field as shown in Figure 4.9 (Devatzes and Hickman, 2009). No direct correspondence between fracture density and permeable zones locations was observed. Thus, this lack of correlation implied that fracture density was not an effective indicator of permeable zones because it was extremely difficult to obtain good quality image logs in highly fractured reservoirs. Another issue was the overlapping of fractures which led to two interpretations. First, a large fracture aperture reading could be made when overlapping fractures have consistent orientations. Second, the whole fracture set could be discarded in confidence filtering of the data because the aggregate set would not exhibit the typical sinusoidal shape that was expected. Thus, a high aperture fracture plane could also be interpreted as a high density cluster of fractures with smaller apertures. Therefore, both high density and high aperture values could be used to identify permeable zones. Other possible sources of errors were data binning inaccuracies and tool measurement uncertainties.

4.6.4 Lithology

Glynn-Morris et al. (2011) investigated the characteristics of feed zones of wells in the Wairakei and Tauhara geothermal fields in New Zealand. They sought to evaluate whether the permeability was derived from lithology or structures. Feedzone locations were identified from PTS logs and completions tests. The characteristic signature of primary permeability from lithology was a diffuse change in temperature with depth. In contrast, structurally based secondary permeability demonstrated sharp variations in PTS logs. Other measured properties from drilled cores included the following: lithology, rock-quality designation (RQD), core recovery factor, loss circulation zones, porosity, smectite presence, rock strength, and core photos. It was concluded that secondary permeability from structures becomes more important as the feed zone depth increases (Glynn-Morris et al., 2011; McLean and McNamara, 2011).

Permeable zones for well 27-15 in the Desert Peak geothermal field exhibited some correlation among temperature anomaly locations, stratigraphic boundaries, and mineral content (Devatzes and Hickman, 2009). One significant feed zone at 4720 ft MD was found just above the boundary between a shale and diorite region. Aside from this, increased illite-chlorite and quartz alteration were observed at this section. Data from the Soultz geothermal field study found that there was high potassium content due to granite alteration in high permeability regions (Sausse et al., 2008). This was claimed to be due to the dissolution of minerals as the fluid flows through the rock matrix thereby increasing the permeability and porosity even further. These altered granite zones represented high conductivity but channelized flow paths as seen in the depth where well GPK3 intersected

the fault zone. Lower degrees of alteration, however, resulted to a higher number of low conductivity paths which resulted to poor well performance such as in the case of GPK4.

Massart et al. (2010) describes the fault geometry encountered in Soultz. Figure 4.10 shows the lithofacies and equivalent porosity of the different zones within a major fault that intersects all three wells (GPK1, GPK2, and GPK3). Three main zones are present within this fault. First, there is a fault core in the middle containing quartz which has the lowest porosity. Second, there are cataclased and brecciated granite zones due to shearing of the fault. Third, hydrothermally altered granite zones have high porosity and serve as main conduits for flow equivalent to 75% of the total. The decreasing porosity with distance of the outermost altered zone is consistent with the inverse fracture density scaling with distance finding of Johri et al. (2012). Furthermore, owing to the symmetry and consistency of the rock properties within each zone, these could be represented by a parallel network of porous channels satisfying tracer and temperature analytical equations derived.

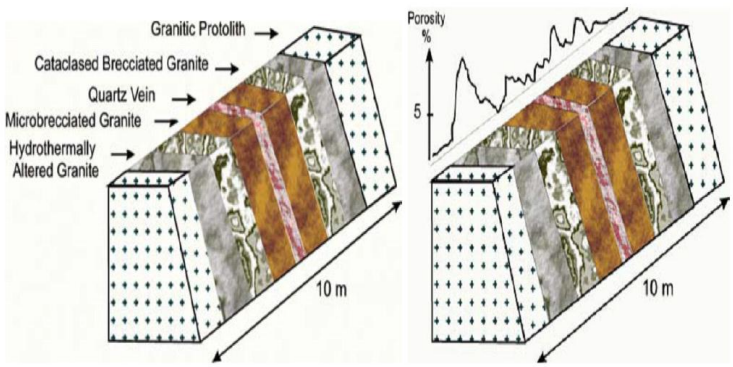

Figure 4.10. Zonation and porosity schematic of a hydrothermally altered fault zone at Soultz (from Massart et al., 2010).

On the other hand, steam production at The Geysers geothermal field was attributed to a network of fractures within a wide shear zone bounded by the right lateral Maacama and Collayomi Fault zones (Sammis et al., 1991). Steam feed zones were observed to occur in a few major fractures hosted in a relatively impermeable greywacke rock. Because steam feed zones were typically observed at shallow depths, this result contradicted the observations of the previous study discussed where shallow feed zones were attributed to lithology and not structures.

4.7 FUTURE WORK

The relationship between scaling properties and heat and mass transport will be investigated further. Analytical models for tracer and heat transport incorporating scaling correlations of aperture and length will be derived. Uncertainty analysis on scaling parameters and borehole imaging data for analytical models will be explored.

The long-term goal is to generate fracture networks using scaling properties and use these in reservoir simulation. To avoid instability problems during numerical simulations in TOUGH2, the finite element code Feflow will be used instead. This program does not have phase change modeling capability; however, it would suffice for this particular modeling application because fluid is injected deep and hence remains as a single phase. Moreover, Feflow is more stable especially in handling tracer modeling. Results from the analytical models of the idealized fracture connections will be compared to the simulated numerical models.

5. REFERENCES

Arnason, K.: Viðnámsmælingar í Jarðhitarannsóknum á Íslandi, Orkustofnun, Orkuþing (2001).

Babadagli, T.: "Evaluation of outcrop fracture patterns of geothermal reservoirs in southwestern Turkey," *Proceedings,* World Geothermal Congress. 2000.

Barker, J.: Modelling doublets and double porosity, *Quarterly Journal of Engineering Geology and Hydrogeology.* **43(3)**, p. 259-268, (2010).

Barton, C.A., Hickman, S., Morin, R., Zoback, M.D., Benoit, D.: "Reservoir-scale fracture permeability in the Dixie Valley, Nevada, geothermal field," *Proceedings*, 23th workshop on Geothermal Reservoir Engineering, Stanford University. 1998.

Barton, C.A., Moos, D., and Tezuka, K.: "Geomechanical wellbore imaging: implications for reservoir fracture permeability," *AAPG Bulletin*, v. 93, no. 11. 2009, 1551-1569.

Barton, C.A. and Zoback, M.D.: "Self-similar distribution and properties of macroscopic fractures at depth in crystalline rock in the Cajon Pass scientific drill hole," *Journal of Geophysical Research*, v.97, no. B4, 1992. 5181-5200.

Barton, C.A., Zoback, M.D., and Moos, D.: "Fluid flow along potentially active faults in crystalline rocks," *Geology*, v.23. 1995, 683-686.

Basel, E., Juliusson, E., and Horne, R. N.: A New Look at Well-to-Well Correlations using Nonparametric, Nonlinear Regression, *Thirty-Sixth Workshop on Geothermal Reservoir Engineering*, Stanford, (2011).

Bayon, F.E.B. and Ogena, M.S.: "Handling the problem of rapid reinjection returns in Palinpinon-I and Tongonan, Philippines," *Proceedings,* World Geothermal Congress. 2005.

Bodvarsson, G.: "Thermal problems in the siting of reinjection wells," *Geothermics,* v. 1, no. 1. 1972, 63-66.

Bradford, S.A., Yates, S.R., Bettahar, M., Simunek, J., 2002. Physical factors affecting the transport and fate of particles in saturated porous media. Water Resour. Res. 38, 1327 (12).

Bullivant, D.P. and O'Sullivan, M.J.: "Some simple models of tracer tests," *Proceedings*, 7th New Zealand Geothermal Workshop. 1985.

Cao, H.: Development of techniques for general purpose simulators, Ph.D. Thesis, Stanford University, Stanford, CA (2002).

Co, C.K.D. and Horne, R.N.: "Characterization of Geothermal Interwell Connectivity Using Thermal and Tracer Data," *GRC Transactions*. 2011, 1411-1416.

Devatzes, N.C. and Hickman, S.H.: "Fractures, stress, and fluid flow prior to stimulation of well 27-15, Desert Peak, Nevada, EGS project," *Proceedings,* 34th workshop on Geothermal Reservoir Engineering, Stanford University. 2009.

Devatzes, N.C. and Hickman, S.H.: "In-situ stress and fracture characterization for planning of an EGS stimulation in the Desert Peak geothermal field, Nevada," *Proceedings,* 35th workshop on Geothermal Reservoir Engineering, Stanford University. 2010.

Dinh, A. V.: Interwell Connectivity Tests in Waterflood Systems, *PhD thesis*, University of Oklahoma, (2009).

Fukuda, D., Akatsuka, T., and Sarudate, M: "Characterization of inter-well connectivity using alcohol tracer and steam geochemistry in the Matsukawa vapor-dominated geothermal field, Northeast Japan," *GRC Transactions*. 2006, 797-801.

Glynn-Morris, T., McLean, K., and Brockbank, K.: "Characterizing feed zones in geothermal fields: integrated learnings from completion testing, image logs and continuous core," *Proceedings,* New Zealand Geothermal Workshop. 2011.

Gringarten, A. C., and Sauty, J.: A Theoretical Study of Heat Extraction from Aquifers with Uniform Regional Flow, *Journal of Geophysical Research*, **80(35)**, (1975).

Gringarten, A.C. and Sauty, J. P.: "A theoretical study of heat extraction from aquifers with uniform regional flow," *Journal of Geophysical Research*. 1975, 4956-4952.

Gringarten, A.C., Witherspoon, P.A., and Ohnishi, Y.: "Theory of heat extraction from fractured hot dry rock," *Journal of Geophysical Research*. 1975, 1120-1124.

Hickman, S.H., Barton, C.A., Zoback, M.D., Morrin, R., Sass, J., and Benoit, R.: "In-situ stress and fracture permeability along the Stillwater fault zone, Dixie Valley, Nevada," *Int. J. Rock Mech. & Min. Sci.*, 34:3-4, Paper No. 126. 1997.

Holder, D.S.: Electrical Impedance Tomography: Methods, History and Applications, IOP, UK (2004).

Holland, J.H.: Adaptation in Natural and Artificial Systems, *Ann Arbor*, University of Michigan Press, **54**, (1975).

Horne, R.N.: "Reservoir Engineering of Reinjection," Course Notes. Stanford University, 1996.

Horne, R.N., and Szucs, P.: Inferring Well-to-Well Connectivity Using Nonparametric Regression on Well Histories, *Thirty-Second Workshop on Geothermal Reservoir Engineering*, Stanford, (2007).

Ishibashi, T., Watanabe, N., Hirano, N., Okamoto, A., and Tsuchiya, N.: "Experimental and numerical evaluation of channeling flow in fractured type of geothermal reservoir," *Proceedings*, 37th workshop on Geothermal Reservoir Engineering, Stanford University. 2012.

Johri, M., Zoback, M.D., and Hennings, P.: "Observationsof fault damage zones at reservoir depths," *Proceedings*, 45th US Rock Mechanics / Geomechanics Symposium, American Rock Mechanics Association. 2012.

Jourde, H., Flodin, E.A., Aydin, A., Durlofsky, L.J., Wen, X.H.: "Computing permeability of fault zones in eolian sandstone from outcrop measurements," *American Association of Petroleum Geologists Bulletin*. 2002.

Juliusson, E, and Horne, R.N.: Fracture Characterization using Production and Injection Data, *DOE Quarterly Report (2009 January to March), Contract DE-FG36-08GO18182*, (2009), 1-17.

Juliusson, E, and Horne, R.N.: Study and Simulation of Tracer and Thermal Transport in Fractured Reservoirs, *Proceedings*, 35th Workshop on Geothermal Reservoir Engineering, Stanford University, Stanford, CA (2010).

Juliusson E. and Horne, R.N.: Fracture characterization using production and injection data, DOE quarterly report (2011 April to June), Contract DE-FG36-08GO18192, Stanford Geothermal Program, Stanford University, California, (2011).

Juliusson E. and Horne, R.N.: Fracture characterization using production and injection data, DOE quarterly report (2011 October to December), Contract DE-FG36-08GO18192, Stanford Geothermal Program, Stanford University, California, (2011).

Karimi-Fard, M., Durlofsky, L.J. and Aziz, K.: An Efficient Discrete Fracture Model Applicable for General Purpose Reservoir Simulators, SPE 79699, SPE Reservoir Simulation Symposium, Houston, TX (2003).

Keller, A., M. Auset, and S. Sirivithayaparkorn (2011). "Pore-Scale Flow." COMSOL Multiphysics Model Library.

Kennelly, AE. The equivalence of triangles and three-pointed stars in conducting networks, *Electrical World and Engineer,* **34**, (1899), 413-414.

Kocabas, I.: Geothermal reservoir characterization via thermal injection backflow and interwell tracer testing. *Geothermics,* **34(1)**, p. 27-46 (2005).

Kreft, A., and Zuber, A.: "On the physical meaning of the dispersion equation and its solutions for different initial and boundary conditions," *Chemical Engineering Science*, v.33. 1978, 1471-1480.

Lauwerier, H.A.: "The Transport of Heat in an Oil Layer Caused by the Injection of Hot Fluid," *Applied. Scientific Research*, **5**(2-3). 1955, 145-150.

Lauwerier, H. A.: The transport of heat in an oil layer caused by the injection of hot fluid. *Applied Scientific Research*, **5(2)**, p. 145-150, (1955).

Lee, K., Ortega, A., Jafroodi, N., and Ershaghi, I.: A Multivariate Autoregressive Model for Characterizing Producer Producer Relationships in Waterfloods from Injection/Production Rate Fluctuations, *SPE Western Regional Meeting* (2010).

Maloszewski, P., and Zuber, A.: On the theory of tracer experiments in fissured rocks with a porous matrix, *Journal of Hydrology,* **79**, p. 333-358, (1985).

Marrett, R., Ortega, O.J., Kelsey, C.M.: "Extent of power-law scaling for natural fractures in rock," *Geology*. 1999. 799-802.

Massart, B., Paillet, M., Henrion, V., Sausse, J., Dezayes, C., Genter, A., Bisset, A.: "Fracture characterization and stochastic modeling of the granitic basement in the HDR Soultz Project (France)," *Proceedings,* World Geothermal Congress. 2010.

Matsunaga, I., Yanagisawa, N., Sugita, H., Tao, H.: "Reservoir monitoring by tracer testing during a long term circulation test at the Hijiori HDR site," *Proceedings,* Twenty-Seventh Workshop on Geothermal Reservoir Engineering, Stanford University. 2002.

Matsunaga, I., Yanagisawa, N., Sugita, H., Tao, H.: "Tracer tests for evaluation of flow in a multi-well and dual fracture system at the Hijiori HDR test site," *Proceedings,* World Geothermal Congress. 2005.

Maturgo, O.O., Sanchez, D. R., and Barroca, G.B.: "Tracer test using naphthalene disulfonates in Southern Negros Geothermal Production Field, Philippines," *Proceedings,* World Geothermal Congress. 2010.

McLean, K. and McNamara, D.: "Fractures interpreted from acoustic formation imaging technology: correlation to permeability," *Proceedings,* 36th workshop on Geothermal Reservoir Engineering, Stanford University. 2011.

Olson, J.E.: "Sublinear scaling of fracture aperture versus length: An exception or the rule?," *Journal of Geophysical Research.* 2003.

Olson, J.E. and Schultz, R.A.: "Comment on "A note on the scaling relations for opening mode fractures in rock" by C.H. Scholz," *Journal of Structural Geology*. 2011, 1523-1524.

Paul, P., Zoback, M.D., and Hennings, P.: "Fluid flow in a fracture reservoir using a geomechanically constrained fault-zone-damage model for reservoir simulation," *Proceedings,* 2007 SPE Annual Technical Conference and Exhibition.

Paul, P., Zoback, M.D., and Hennings, P.: "A method to implement permeability anisotropy associated with fault damage zones in reservoir simulation," *SPE Reservoir Evaluation and Engineering*. 2011.

Pollard, D.D. and Segall, P.: "Theoretical displacement and stresses near fractures in rock: with applications to faults, joints, veins, dikes, and solution surfaces. In B.K. Atkinson, ed.," *Fracture Mechanics of Rock,* Academic Press Inc. 1987, 277-349.

Pritchett, J.W.: Finding Hidden Geothermal Resources in the Basin and Range Using Electrical Survey Techniques. A Computational Feasibility Study (2004).

Pruess, K. and Bodvarsson, G. S.: "Thermal effects of reinjection in geothermal reservoirs with major vertical fractures," *Journal of Petroleum Technology*. 1984, 1567-1578.

Reimus, P., Watson, T., Vermeul, V., Newell, D., and Williams, M.: Laboratory Testing and Modeling to Evaluate Perfluorocarbon Compounds as Tracers in Geothermal Systems, *Thirty-Sixth Workshop on Geothermal Reservoir Engineering,* Stanford, (2011).

Renshaw, C.E. and Park, J.C.: "Effect of mechanical interactions on the scaling of fracture length and aperture," *Nature*. 1997, 482-484.

Rivera, J.R., Ramirez, J.S., and Rodriguez, F.G.: "Parallel fractures model for tracer flow through geothermal reservoirs – preliminary results," *Proceedings*, 12th workshop on Geothermal Reservoir Engineering, Stanford University. 1987.

Sammis, C.G., An, L.J., Ershaghi, I.: "Fracture patterns in greywacke outcrops at the Geysers geothermal field," *Proceedings,* 16th workshop on Geothermal Reservoir Engineering, Stanford University. 1991.

Sammis, C.G., An, L.J., Ershaghi, I.: "Determining the 3-D fracture structure in the Geysers geothermal reservoir*," Proceedings*, 16th workshop on Geothermal Reservoir Engineering, Stanford University. 1992.

Sausse, J., Dezayes, C., Genter, A., and Bisset, A.: "Characterization of fracture connectivity and fluid flow pathways derived from geological interpretation and 3D modeling of the deep seated EGS reservoir of Soultz (France)," *Proceedings*, 33rd workshop on Geothermal Reservoir Engineering, Stanford University. 2008.

Scholz, C.H.: "A note on the scaling relations for opening mode fractures in rock," *Journal of Structural Geology*. 2010, 1485-1487.

Shaw, J.C., Churcher, P.L. and Hawkins, B.F., "The effects of firing on Berea sandstone." Published in Proceedings from the SPE International Symposium on Oilfield Chemistry, Houston, Texas. SPE Paper No. 18463, p. 63-74 (1989).

Shewchuk J.R.: Triangle: Engineering a 2D Quality ;Mesh Generator and Delaunay Triangulator, *Applied Computational Geometry: Towards Geometric Engineering*, **1148**, (1996), 203-222.

Singha, K. and Gorelick, S.M. Saline Tracer Visualized with Three-dimensional Electrical Resistivity Tomography: Field-scale Spatial Moment Analysis. *Water Resources Research*, **41,** (2005), W05023.

Slater, L., Binley, A.M., Daily, W. and Johnson, R. Cross-hole Electrical Imaging of a Controlled Saline Tracer Injection. *Journal of Applied Geophysics*, **44**, (2000), 85-102.

Stacey, R.W., Li, K. and Horne, R.N.: Electrical Impedance Tomography (EIT) Method for Saturation Determination, *Proceedings*, 31st Workshop on Geothermal Reservoir Engineering, Stanford University, Stanford, CA (2006).

Sullera, M. M., and Horne, R. N.: Inferring injection returns from chloride monitoring data, *Geothermics*, **30(6)**, 591–616, Elsevier, (2001).

Syndansk, R.D., "Discussion of the effect of temperature and confining pressure on single-phase flow in consolidated rocks." JPT, August, p. 1329-1330 (1980).

Tateno, M., Watanabe, K., Nakatsuka, K., and Takahashi, H.: "Fractal Characterization of the Fracture Distribution and the Permeability in Geothermal Reservoirs," *Proceedings*, World Geothermal Congress. 1995.

Tenma, N., Yamaguchi, T., and Zyvoloski, G.: Variation of the characteristics of the shallow reservoir at the Hijiori test site between 90-days circulation test and long-term circulation test using FEHM code." *Proceedings*, World Geothermal Congress. 2005.

Ucok, H., Ershaghi, I. and Olhoeft, G.R.: Electrical Resistivity of Geothermal Brines, *Journal of Petroleum Technology*, **32**, (1980), 717-727.

Urbino, E. G., and Horne, R. N.: Optimizing reinjection strategy at Palinpinon, Philippines, based on chloride data. *Sixteenth Workshop on Geothermal Reservoir Engineering*. Stanford, (1991).

Voskov, D.: Description of the Thermal GPRS, Technical Report, Department of Energy Resources Engineering, Stanford University, Stanford, CA (2006).

Wang, P. and Horne, R.N.: Integrating Resistivity Data with Production Data for Improved Reservoir Modeling, SPE 59425, SPE Asia Pacific Conference, Yokohama, Japan (2000).

Zoback, M.D.: "*Reservoir Geomechanics*," Cambridge: Cambridge University Press, 2007.